Université d'Aix-Marseille

École doctorale de sciences de la vie et de la santé

UMR 7283

Laboratoire de Chimie Bactérienne

Thèse présentée pour obtenir le grade universitaire de docteur

Discipline : Biologie
Spécialité : Microbiologie

Lionel UHL

Modélisations mathématiques de la dynamique des formes réactives de l'oxygène chez *Escherichia coli*

Soutenue le 24/04/2017 devant le jury :

Rachel MÉALLET-RENAULT	Université Paris Sud	Rapporteur
Hans GEISELMANN	Université Grenoble Alpes	Rapporteur
Michel SLIWA	Université Lille 1	Examinateur
Florence HUBERT	Aix-Marseille Université	Examinateur
Frédéric BARRAS	Aix-Marseille Université	Examinateur
Sam DUKAN	Click4Tag	Directeur de thèse

AIX-MARSEILLE UNIVERSITY

DOCTORAL THESIS

Mathematical models for reactive oxygen species dynamic in *Escherichia coli*

Author:
Lionel UHL

Supervisor:
Dr. Sam DUKAN

A thesis submitted in fulfilment of the requirements

for the degree of Doctor of Philosophy

in the

Laboratoire de Chimie Bactérienne

École doctorale de sciences de la vie et de la santé

March 21, 2017

Declaration of Authorship

I, Lionel UHL, declare that this thesis titled, "Mathematical models for reactive oxygen species dynamic in *Escherichia coli*" and the work presented in it are my own. I confirm that:

- This work was done wholly or mainly while in candidature for a research degree at this University.
- Where any part of this thesis has previously been submitted for a degree or any other qualification at this University or any other institution, this has been clearly stated.
- Where I have consulted the published work of others, this is always clearly attributed.
- Where I have quoted from the work of others, the source is always given. With the exception of such quotations, this thesis is entirely my own work.
- I have acknowledged all main sources of help.
- Where the thesis is based on work done by myself jointly with others, I have made clear exactly what was done by others and what I have contributed myself.

Signed:

Date:

“Remember that all models are wrong; the practical question is how wrong do they have to be to not be useful. ”

Box and Draper, Empirical Model-Building.

AIX-MARSEILLE UNIVERSITY

Abstract

Laboratoire de Chimie Bactérienne

École doctorale de sciences de la vie et de la santé

Doctor of Philosophy

Mathematical models for reactive oxygen species dynamic in *Escherichia coli*

by Lionel UHL

The Reactive Oxygen Species (ROS) are molecules (superoxide $O_2^{\bullet-}$, hydrogen peroxide H_2O_2 and hydroxyl radical $HO^{\bullet}$) that are continuously generated in living cells as a consequence of aerobic life. They are partially eliminated by scavenging systems. Nevertheless, ROS can unfortunately react with cellular proteins, lipids or DNA leading to cell damage. The mechanisms of such lesions is still being studied: we are talking about « oxidative stress ». Using *Escherichia coli* as a model organism this thesis is concerned with the numerical simulation of ROS dynamics. In the first part of this work, simulations were performed in a deterministic way to predict the behaviour of a set of cells. By studying killing of *E. coli* by exposure to H_2O_2, we show that intracellular available iron and cell density, two factors potentially involved in ROS dynamics, play a major role in the prediction of experimental results in particular in bimodal cell killing. We then evaluate the relative roles of major defences against H_2O_2. Although the key actors in cell defence are enzymes and membrane, a detailed analysis shows that their involvement depends on the H_2O_2 concentration level. In the second part and thanks to the first deterministic approach, we study more closely the fate of the single cell with a stochastic point of view in physiological conditions. We show that elementary chemical stochasticity allows bacteria to segregate specialized cells in prevision of possible stress challenge. Actually, whereas ROS distribution does not activate defence regulation without exogenous stress, we demonstrate that this distribution may activate DNA repair mechanisms because DNA nicks are the result of a succession of rare events which involve a small number of molecules.

Acknowledgements

I would first like to express my gratitude to my supervisor Dr. Sam Dukan for entrusting me with such an interesting project from which I have gained a tremendous amount of knowledge and experience. I consider it a privilege to have had the opportunity to work with him.

I would also like to thank Benjamin Ezraty for the trust he placed in my thesis and for his continued words of encouragement and motivation throughout the period of research.

Most importantly, I would like to thank the members of my thesis committee Hans Geiselmann, Rachel Méallet-Renault, Michel sliwa and Florence Hubert for their insightful comments and encouragement, but also for the challenging questions which incited me to widen my research from various perspectives.

My sincere thanks also go to Prof. Frédéric Barras, who provided me with the opportunity to join his team in the Laboratoire de Chimie Bactérienne. I thank all the members of the team who have contributed to my thesis work in one way or another. My thanks go to Audrey Dumont, Maïalène Chabalier, Audrey Gerstel, Elodie Fugier, Pascal Caillet and Karyn Wilson-Costa for carefully proof-reading parts of my manuscript. I sincerely thank them for setting aside time to assist me in this endeavour.

Finally, I would like to thank Audrey Rault and our daughters Louison and Rose for their unfailing support.

Contents

Declaration of Authorship iii

Abstract vii

Acknowledgements ix

1 Introduction 1

1.1 Reactive oxygen species and oxidative stress 1

1.1.1 From molecular oxygen to reactive oxygen species 2

1.1.2 Defences against ROS 4

1.2 Introduction to kinetic laws 4

1.2.1 Chemical kinetic definitions 4

1.2.2 Enzyme reactions, the Michaelis-Menten mechanism 7

1.3 Analytical resolution 9

1.4 Numerical resolutions 10

1.5 Stochastic approach 11

1.5.1 Presentation 12

Chemical reactions and probabilities 12

Diffusion and probability 13

1.5.2 Algorithm 15

Description 15

1.5.3 The connectivity matrix 16

1.5.4 An application 17

1.6 Mesoscopic reaction-diffusion models 18

1.7 Organization and aim of the Thesis 22

1.7.1 Hydrogen peroxide mode of action 22
1.7.2 The major defences relative roles against hydrogen peroxide . . . 23
1.7.3 ROS in single cell 23

2 Hydrogen peroxide induced cell death: One or two modes of action? 29

2.1 Introduction 31
2.2 Materials and methods 32
2.3 Results and discussion 32
2.3.1 The key role of free iron, its decrease during oxidative stress . . . 32
A simple in vitro system 33
2.3.2 Mathematical analysis of the in vivo Fenton system 34
Mathematical model 37
Choice of kinetic constants 42
Position and width of mode one killing 48
2.3.3 Cell density involvement. 50
2.4 Conclusions 52

3 The major defences relative roles and consequences in *E. coli* 63

3.1 Introduction 65
3.2 Materials and Methods 67
3.2.1 Superoxide kinetics 68
3.2.2 Internal hydrogen peroxide kinetics 69
3.2.3 External hydrogen peroxide 70
3.2.4 Cell density 70
3.2.5 Kinetic constants 71
3.2.6 Numerical simulations 72
3.3 Results and discussion 72
3.3.1 Superoxide evolution 72
In the wild-type strain 72
In a SOD(-) mutant 74

In a *SOD*(-) *GSH*(-) mutant 75
Superoxide summary 76
3.3.2 Internal hydrogen peroxide 77
Without exogenous stress 77
With exogenous stress 81
3.3.3 Consequence of defence switch in the primary scavenger 93
Cumulative internal H_2O_2 concentration, rather than maximum internal H_2O_2 concentration, is involved in the H_2O_2-mediated death of bacterial cells 94
3.4 Conclusions 98
3.4.1 In the absence of exogenous stress 98
3.4.2 With exogenous H_2O_2 stress 98

4 ROS stochasticity can explain single cell biological specialization 105
4.1 Introduction 105
4.2 Material and methods 106
4.2.1 Superoxide kinetics 107
4.2.2 Internal hydrogen peroxide kinetics 107
4.2.3 External hydrogen peroxide 108
4.2.4 Kinetic constants 109
4.2.5 Hydroxyl radical 109
4.2.6 Transcription factors that defend *E. coli* 110
4.2.7 Simulation 111
4.3 Results and discussion 112
4.3.1 Deterministic previsions 112
Superoxide 112
Hydrogen peroxide 113
Hydroxyl radical production 114
The OxyR transcription factor 115
4.3.2 Stochastic results 120

Superoxide distribution 120
Hydrogen peroxide distribution 124
OxyR distribution 124
DNA distribution 128

5 Conclusions and perspectives **139**

A Numerical methods for ODE **145**
A.1 Runge-Kutta 145
A.1.1 ODE discretization 145
A.1.2 Runge-Kutta methods (*RK*) 145
Presentation 145
Method Construction 146
A.2 Adaptative RK methods 149
A.3 Multistep methods 152
A.3.1 Adams-Bashforth methods 153
Presentation 153
Examples 153
A.3.2 Adams-Moulton methods 154
Presentation 154
Examples 154
A.3.3 Nyström methods 155
Presentation 155
Examples 155
A.3.4 Milne-Simpson methods 156
Presentation 156
Examples 156
A.3.5 Backward Differentiation Formulas 157

B A passive physical model for DnaK chaperoning and disaggregation **161**
B.1 Introduction 161

B.2 Materials and methods . . . 163
B.2.1 Presentation of the model . . . 163
B.2.2 The aggregation phenomenon . . . 164
B.2.3 Algorithm . . . 165
B.2.4 Constants used for simulation and validity . . . 168
B.3 Results and discussion . . . 170

List of Figures

1.1 The redox states of molecular oxygen. 3

1.2 Scheme of an elementary process $AB + C \rightarrow A + BC$. 5

1.3 Scheme of Michaelis-Menten mechanism. 7

1.4 Evolution of enzymolysis with the substrate concentration. 9

1.5 Scheme of diffusion jump in a one-dimensional system. 14

1.6 Example of subvolume index organization in a 3D system. 17

1.7 Evolutions of the reactant fraction for a first order reaction solved with the Gillespie algorithm and the deterministic one. The rate constant is $k = 1\ \mathrm{s}^{-1}$. 18

1.8 Reactant distribution in a first order reaction solved with the Gillespie algorithm 19

1.9 Configuration of a hypothetical model of compartmentalization 20

1.10 Decrease in substrate by reaction with H_2O_2 according to 3 models of compartmentalization. 21

2.1 Simulation for H_2O_2-mediated mode 1 killing in a Fenton system 34

2.2 *in vivo* NADH levels after H_2O_2challenge of *E. coli*. 39

2.3 Scheme of ROS interaction in the mathematical model. 41

2.4 Average DNA oxidation (during 15 minutes) dependence upon H_2O_2 external concentration and maximal Fe^{2+} recycling rate $v_{\max}$. C_0 is set to 1 mM. Initially, cell density was set to 10^7 cell/mL. The kinetic parameters used for the simulation are gathered in table 2.2. 49

2.5 Average DNA oxidation (during 15 minutes) dependence upon H_2O_2 external concentration and parameter C_0. $v_{\max}$ is set to 50 $\mu\mathrm{M\ s}^{-1}$. 51

2.6 DNA oxidation (average during 15 minutes) dependence upon H_2O_2 external concentration and free available iron concentration. Parameter C_0 is set to 0.5 mM and $v_{\max}$ is set to 50 μM s^{-1}. 52

2.7 Extracellular H_2O_2 concentration, determined after 15 minutes of incubation with various amounts of exogenous H_2O_2, in a wild-type strain incubated in LB and exogenous H_2O_2 concentration simulated under the same experimental conditions. 53

2.8 Simulation of the average H_2O_2 external concentration dependence with cell density and initial H_2O_2 exogenous concentration. 54

2.9 Simulation of the average oxidized DNA proportion dependence with cell density and initial H_2O_2 exogenous concentration. Inset shows the maximal oxidized DNA proportion dependence with cell density. 55

3.1 Change in $O_2^{\bullet -}$ concentration in the *E. coli* wild-type strain. 73

3.2 Changes in $O_2^{\bullet -}$ concentration in a $SOD(-)$ mutant 75

3.3 Change in $O_2^{\bullet -}$ concentration i2001n $SOD(-)\,GSH(-)$ mutants. 76

3.4 Changes in internal H_2O_2 concentration in the wild-type strain with 10^7 cells ml^{-1}. 79

3.5 Changes in internal H_2O_2 concentration in the wild-type strain with 10^6 cells ml^{-1} 81

3.6 Changes in H_2O_2 concentration in the wild-type strain with 10^9 cells ml^{-1}. 82

3.7 Kinetics of exogenous H_2O_2 decomposition for 1.5×10^8 *E. coli* cells ml^{-1}. for Cat(-) and Ahp (-) mutants mutant. 83

3.8 Higher magnification for Fig. 3.7). 84

3.9 $In\ silico$, breakdown of exogenous H_2O_2 by whole cells (Ahp(-) mutant) or cell extract. Simulation runs with 4×10^6 cells ml^{-1}. 85

3.10 Extract of Seaver and Imlay (Hydrogen Peroxide Fluxes and Compartmentalization inside Growing *Escherichia coli*). 86

3.11 Changes in internal H_2O_2 concentration in the wild type after the addition of 1.5 μM exogenous H_2O_2 with 1.45×10^7 cells ml^{-1}. 88

3.12 Changes in external H_2O_2 concentration in the wild type after the addition of 1.5 μM exogenous H_2O_2 with 1.45×10^7 cells ml^{-1}. 89

3.13 Changes in external H_2O_2 concentration in the wild type after the addition of 1.5 μM exogenous H_2O_2 with 2×10^8 cells ml^{-1}. 90

3.14 Changes in internal H_2O_2 concentration in the wild type after the addition of 1 mM exogenous H_2O_2 with 1.45×10^7 cells ml^{-1}. 92

3.15 Changes in the ration between external initial H_2O_2 concentration and internal maximal H_2O_2 concentration in *E. coli* wild type. 94

3.16 Changes in external H_2O_2 half-life with different initial external H_2O_2 concentrations and 3 different cell densities in *E. coli* wild type. 95

3.17 Changes in external H_2O_2 half-life with cell densities and with 7 different initial external H_2O_2 concentrations in *E. coli* wild type. 96

3.18 Simulation of Ma and Eaton experiment following external hydrogen peroxide concentration. 97

3.19 Simulation of Ma and Eaton experiment following internal hydrogen peroxide concentration. 98

4.1 Numerical simulation of OxyR activation and deactivation when *E. coli* was treated with 200 μM of H_2O_2 117

4.2 Extract from Aslund *et al.*. OxyR activation and deactivation when *E. coli* was treated with 200 μM of H_2O_2 at $OD_{600} = 0.4$ 117

4.3 Simulation of OxyR (reduced form) *in vivo* activation following exposure to increasing concentrations of H_2O_2 119

4.4 Extract from Aslund *et al.* and Tao. OxyR activation and deactivation when *E. coli* was treated with increasing concentrations of external H_2O_2 119

4.5 Superoxide number in each cell represented in a square lattice of 32 by 32 cells (left panel) and Superoxide distribution histogram (right panel). 121

4.6 Superoxide average number in each cell represented in a square lattice of 32 by 32 cells (left panel) and the corresponding standard deviation. . 121

4.7 Superoxide maximal number in each cell represented in a square lattice of 32 by 32 cells (left panel) and Superoxide maximal number distribution histogram (right panel). 122
4.8 Superoxide average number in cell versus time for a system of 1032 cells. 122
4.9 Superoxide total number produced in each cell represented in a square lattice of 32 by 32 cells (left panel) and Superoxide total number produced distribution histogram (right panel). 123
4.10 Superoxide number evolution in one cell during a narrow time interval. 123
4.11 Hydrogen peroxide number in each cell represented in a square lattice of 32 by 32 cells (left panel) and Hydrogen peroxide distribution histogram (right panel). 124
4.12 Hydrogen peroxide average number in each cell represented in a square lattice of 32 by 32 cells (left panel) and the corresponding standard deviation. 125
4.13 Hydrogen peroxide number in each cell represented in a square lattice of 32 by 32 cells (left panel) and Hydrogen peroxide distribution histogram (right panel). 125
4.14 Hydrogen peroxide average number in cell versus time calculated for a system of 1032 cells. 126
4.15 Hydrogen peroxide total number produced in each cell represented in a square lattice of 32 by 32 cells (left panel) and Hydrogen peroxide total number produced distribution histogram (right panel). 126
4.16 OxyR number in each cell represented in a square lattice of 32 by 32 cells (left panel) and OxyR distribution histogram (right panel). 127
4.17 OxyR average number in each cell represented in a square lattice of 32 by 32 cells (left panel) and the corresponding standard deviation. 127
4.18 OxyR maximal number in each cell represented in a square lattice of 32 by 32 cells (left panel) and maximal OxyR distribution histogram (right panel). 128

4.19 OxyR average number in cell versus time for a system of 1032 cells. 128

4.20 Scatter plot of $OxyR_{ox}$ maximal number in cell versus H_2O_2 maximal number for a system of 1032 cells. 129

4.21 DNA types of damage number in each cell represented in a square lattice of 32 by 32 cells (left panel) and DNA damage distribution histogram. . 131

B.1 Green fluorescent DnaK protein microscopy. 162

B.2 DnaK evolution in *E. coli* with NSM simulation, after an alcoholic stress produced during the first 6 minutes. 171

B.3 Abnormal proteins evolution in *E. coli* with NSM simulation, after an alcoholic stress produced during the first 6 minutes. 172

B.4 Free DnaK, DnaK-protein complexes and free abnormal proteins evolution after an alcoholic stress in a homogeneous system. 172

B.5 Evolution of the number of abnormal protein obtained by different simulations with the next sub-volume method. 173

B.6 Evolution of the number of free DnaK obtained by different simulations with the next sub-volume method. 173

List of Tables

1.1 Standard reduction potentials for dioxygen and ROS 3

2.1 Ordered kinetic rate constants and concentration of the major metabolites in *E.coli*. 44

2.2 Summary of the different constants used for *in silico* simulations. 50

3.1 Kinetic constants used to describe H_2O_2 evolution. 71

3.2 Kinetic constants used to describe $O_2^{\bullet -}$ evolution. 72

3.3 Superoxide steady-state concentration. 77

3.4 H_2O_2 steady-state concentration. 80

4.1 Kinetic constants used to describe $O_2^{\bullet -}$ evolution. 109

4.2 Kinetic constants used to describe H_2O_2 evolution. 109

A.1 Butcher table for RK methods 146

A.2 Butcher table for Euler method 147

A.3 Butcher table for modified Euler method 147

A.4 Butcher table for Heun method 147

A.5 Butcher table for the $RK4$ method 148

A.6 Butcher table for Newton method 148

A.7 Butcher table for Cash-Karp method 149

A.8 Butcher table for Runge-Kutta-Fehlberg method 150

List of Abbreviations

Ahp	**A**lkyl **H**ydroperoxide **R**eductase
BDF	**B**ackward **D**ifferentiation **F**ormulas
Cat	Catalase
GSH	Glutathion
MO	**M**olecular **O**rbital
MS	**M**ulti **S**tep (method)
NADH	**N**icotinamide **A**denine **D**inucleotide
NSM	**N**ext **S**ub-volume **M**ethod
ODE	**O**rdinary **D**ifferential **E**quation
PDE	**P**artial **D**ifferential **E**quations
RK	**R**unge **K**utta (method)
ROS	**R**eactive **O**xygen **S**pecies
SOD	**S**uper **O**xide **D**ismutase

To my daughters Louison and Rose

Chapter 1

Introduction

This chapter stands out from much of the rest of this thesis in that it mostly deals with academic knowledge in isolation from any results. On the one hand, it evokes basic knowledge Reactive Oxygen Species (ROS) and chemical kinetics; it is important to bring this to the attention of the mathematics community. On the other hand, it is useful to introduce the mathematical models needed to understand the resolution of kinetic equations.

Finally this thesis only considers *Escherichia coli* as an example of bacteria and as a system for studying. Indeed this bacterium has been intensively investigated for over 60 years and literature covers a large set of data. Whereas *E. coli* can switch to fermentation (anaerobic respiration) in the absence of oxygen, our experiments only deal with aerobic respiration when oxygen is present.

1.1 Reactive oxygen species and oxidative stress

Life emerged nearly 4 billion years ago in an anaerobic world, therefore primitive biological mechanisms and enzymes had to change and adapt as molecular oxygen slowly accumulated on Earth. In order to thrive in an oxygenated medium, The ancestors of *E. coli* had to evolve, yet the current oxygen level can still injure bacteria or cells. The mechanism of such injuries is still being studied, we are talking about « oxidative stress ». ROS are a family of molecules that are continuously generated, transformed and consumed in all living cells or organisms as a consequence of aerobic life. In order to control ROS levels, cells balance their generation with their elimination by scavenging systems. Nevertheless, ROS can unfortunately react with cellular proteins, lipids or DNA leading to cell damage or involving lesions in cells that contribute for example to carcinogenesis, Parkinson's disease or Alzheimer's disease [1].

1.1.1 From molecular oxygen to reactive oxygen species

Free radicals are molecules or molecular fragments that contain one or more unpaired electrons in molecular orbitals (MO). The valence bond theory describes molecular oxygen (dioxygen) as a double bond compound with only paired electrons ($\underline{\overline{O}} = \underline{\overline{O}}$) but this description cannot explain oxygen chemical or paramagnetic properties. Nevertheless, MO theory (which is more complete) predicts that oxygen is a di-radical molecule with two unpaired electrons ($^\bullet\underline{\overline{O}} - \underline{\overline{O}}\,^\bullet$) which then account for oxygen properties. This electronic configuration explains the kinetic stability of dioxygen. Actually the two electrons of the highest occupied molecular orbital (HOMO) have parallel spins whereas most (bio)chemical compounds contain anti-parallel electrons on their HOMO, therefore quantum mechanic criteria for chemical reactivity suggest that the oxidizing ability for molecular oxygen is reduced. A second reason for the weak oxidative ability of molecular oxygen is its low affinity for the first electron : -0.33 V ($O_2 + e^- \rightarrow O_2^{\bullet -}$) compared to the two electron reduction : +0.94 V ($O_2 + 2e^- + 2H^+ \rightarrow H_2O_2$). Abstraction of a single electron from a donor creates superoxide ($O_2^{\bullet -}$) and then abstraction of a second electron forms hydrogen peroxide (H_2O_2). The production of those two reactive oxygen species (ROS) occurs mostly within a cell during the "electron transport chain mechanism" responsible for cellular respiration and energy production. During this mechanism , electrons pass from different donors to different acceptors, but even under normal conditions, some electrons escape the electron transport chain to produce $O_2^{\bullet -}$ and then H_2O_2.

The iron catalysed breakdown of H_2O_2 generates the third ROS $HO^\bullet$ called hydroxyl radical according to the Fenton reaction [2, 3]:

$$Fe^{2+} + H_2O_2 \longrightarrow Fe^{3+} + HO^\bullet + HO^-$$

TABLE 1.1: Standard reduction potentials for dioxygen and ROS. The values of $E°$ are given for aqueous solutions with O_2 partial pressure at 1 atm, molecular concentrations at 1 M and $pH = 7$.

	$E°$ (V)
One electron reduction	
$O_2 + e^- \rightleftharpoons O_2^{\bullet -}$	-0.33
$O_2^{\bullet -} + H^+ + e^- \rightleftharpoons H_2O_2$	+0.94
$H_2O_2 + H^+ + e^- \rightleftharpoons HO^{\bullet} + H_2O$	+0.38
$HO^{\bullet} + H^+ + e^- \rightleftharpoons H_2O$	+2.33
Two electron reduction	
$O_2 + 2H^+ + 2e^- \rightleftharpoons H_2O_2$	+0.33
$H_2O_2 + +2H^+ + 2e^- \rightleftharpoons H_2O$	+1.35
Four electron reduction	
$O_2 + 4H^+ + 4e^- \rightleftharpoons 2H_2O$	+0.82

$HO^{\bullet}$ is a highly reactive radical with a half-life lower than 1 ns, therefore it reacts close to its site of formation. For example, it can cause addition to DNA bases involving generation of a variety of oxidative products [4] or it can attack membrane lipid leading to severe damage [5].

The redox states of molecular oxygen include $O_2^{\bullet -}$, H_2O_2, $HO^{\bullet}$ and water with the reduction potentials shown in figure 1.1 and table 1.1. The standard state sets concentration to 1 M and pH to 7.

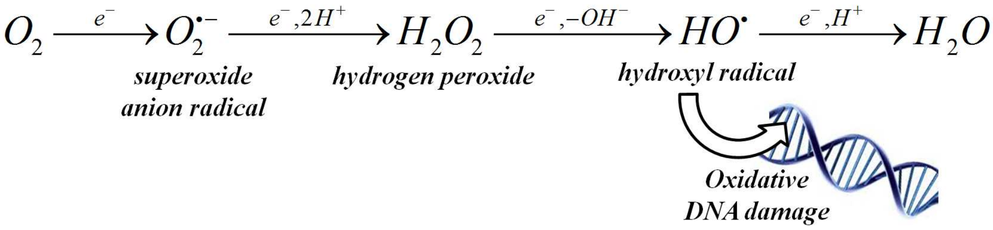
$O_2 \xrightarrow{e^-} O_2^{\bullet -} \xrightarrow{e^-,2H^+} H_2O_2 \xrightarrow{e^-,-OH^-} HO^{\bullet} \xrightarrow{e^-,H^+} H_2O$
superoxide anion radical
hydrogen peroxide
hydroxyl radical
Oxidative DNA damage

FIGURE 1.1: The redox states of molecular oxygen.

1.1.2 Defences against ROS

Oxidative stress results from an imbalance between exposure to ROS and defences against ROS that can potentially cause damage to all macromolecules [6]. Cells exposed to molecular oxygen and the resulting ROS develop important antioxidant defences. Superoxide dismutases (SOD) are a class of enzymes which catalyse the dismutation of $O_2^{\bullet -}$ into dioxygen and H_2O_2, it is the major way used to eliminate $O_2^{\bullet -}$. The corresponding reaction is :

$$O_2^{\bullet -} + H^+ \xrightarrow[SOD]{k_2} \frac{1}{2}H_2O_2 + \frac{1}{2}O_2$$

SOD then work in conjunction with H_2O_2 scavenging enzymes such as catalase (Cat) or Alkylhydroperoxidase (Ahp):

$$H_2O_2 \xrightarrow[Ahp]{Cat} H_2O + \frac{1}{2}O_2$$

E. coli mutants that lack either SOD or catalases show a variety of growth defects [7]. Nevertheless $HO^\bullet$ is a powerful radical oxidant which can react with all organic biomolecules at nearly diffusion-limited rates. Therefore it reacts very close to the site of its production. An organism does not a develop mechanism in order to scavenge this highly reactive radical. Solutions found by cells try to minimize the frequency of its production or try to repair its damage.

1.2 Introduction to kinetic laws

1.2.1 Chemical kinetic definitions

Chemical kinetic simply deals with the rates of chemical processes. Any chemical processes may be split into a sequence of one or more single-step processes known as elementary processes. Elementary processes usually involve either a single reactive collision between two molecules, or dissociation of a single reactant molecule. A major point to recognize is that many reactions that are written as a single reaction equation in fact consist of a series of elementary processes. For instance, the chemical reaction catalysed by SOD is simply written $O_2^{\bullet -} + H^+ \longrightarrow \frac{1}{2}H_2O_2 + \frac{1}{2}O_2$ but it hides a multitude of complex stages. In kinetics, a « complex reaction » simply means a reaction whose mechanism comprises more than one elementary step.

As a general rule, elementary processes involve a transition state between two atomic or molecular states separated by a potential barrier which constitutes the activation energy (E_A) of the reaction. This energy determines the rate constant of the reaction according to the Arrhenius equation [8]:

$$k = A \exp\left(-\frac{E_A}{RT}\right)$$

Figure 1.2 illustrates the way used by reactants (for instance $AB + C$ to be transformed into products $A + BC$.

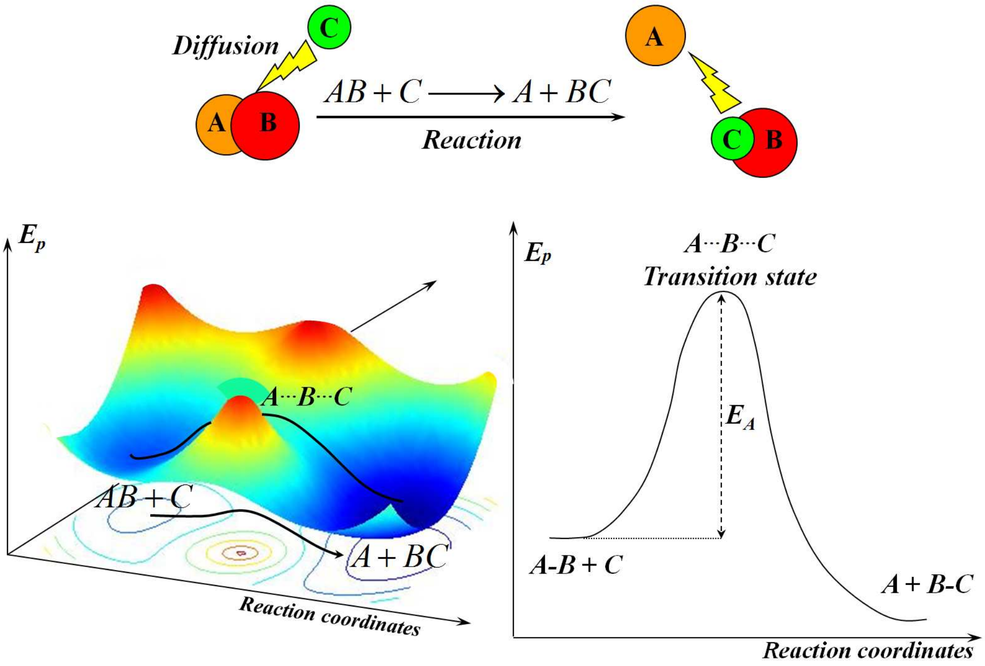
Diffusion
C
A
B
AB + C ⟶ A + BC
Reaction
A
C
B
Ep
A···B···C
AB + C
A + BC
Reaction coordinates
Ep
A···B···C
Transition state
EA
A-B + C
A + B-C
Reaction coordinates

FIGURE 1.2: Scheme of an elementary process $AB + C \rightarrow A + BC$. Potential energy versus the reaction coordinate.

When the barrier is low ($i.e.$ $E_A \ll RT$), the thermal and kinetic energy of the reactants will generally be high enough to surmount the barrier and move over to products, and the reaction will be fast ($i.e.$ $k \gg 1$). However, when the activation energy is high, only a few reactants will have sufficient energy, and the reaction will be much slower. The Arrhenius equation indicates the temperature dependence of reaction rates. A differential notation gives :

$$\frac{\mathrm{d}k}{k} = \frac{E_A \mathrm{d}T}{RT^2}$$

Activation energy is typically spaced between 10 and 200 kJ.mol^{-1}. Chemical tables generally give the rate constant at 25 $^\circ C$ (298 K) whereas biological reactions generally occur at 37 $^\circ C$ (310 K). This relative temperature difference involves a relative difference on rate constant spaced between 0.2 and 3.2 meaning that we do not change the order of magnitude of the rate constant.

The rate law is an expression relating the rate of a reaction to the concentrations of the chemical species present. It includes reactants and catalysts. Complex reactions often give complex expression but, the Law of Mass Action in chemical kinetics states that the rate at which an elementary step is produced is proportional to the product of the reactant concentration, therefore the reaction $AB + C \rightarrow A + BC$ leads to the kinetic rate $v = k[AB][C]$. We can notice that the kinetic rate is all the greater as the reactants are concentrated, indeed the probability of a collision is higher at high concentrations. We can also notice that the kinetic rate depends on the rate constant which increases when the temperature increases.

The half life, $t_{1/2}$ of a chemical species is defined as the time it takes for its concentration to fall to half of its initial value. Considering a first order reaction $A \rightarrow products$ with rate constant k, we can write:

$$v = -\frac{\mathrm{d}[A]}{\mathrm{d}t} = k[A]$$

After integration we have:

$$\ln[A] = \ln[A]_0 - kt$$

Then we can show that the half life is given by:

$$t_{1/2} = \frac{\ln 2}{k}$$

In this case, the half life does not depend on the initial concentration.

For example, considering the elementary reaction of recombination of hydroxyl radical $HO^\bullet + HO^\bullet \rightarrow H_2O_2$, the reaction rate is:

$$v = -\frac{\mathrm{d}\left[HO^\bullet\right]}{\mathrm{d}t} = k\left[HO^\bullet\right]^2$$

where k is the rate constant. The kinetic order of this elementary reaction is 2 which corresponds to the power and to the molecularity of the reactant. An integration leads to:

$$\frac{1}{\left[HO^\bullet\right]} = \frac{1}{\left[HO^\bullet\right]_0} + kt$$

but here the half life is:

$$t_{1/2} = \frac{1}{k\left[HO^\bullet\right]_0}$$

and depends on the initial concentration.

1.2.2 Enzyme reactions, the Michaelis-Menten mechanism

An enzyme accelerates a chemical reaction by lowering the activation energy. Enzymes generally operate by having an active site that is carefully designed to bind a particular reactant molecule called substrate. In an enzyme-catalysed reaction, a substrate S is converted to products P in a reaction which is catalysed by an enzyme E. Michaelis and Menten proposed the following mechanism (Figure 1.3) involving formation of a bound enzyme-substrate complex ES ([9]) :

$$E + S \underset{k_{-1}}{\overset{k_1}{\rightleftharpoons}} ES \xrightarrow{k_{cat}} P + E$$

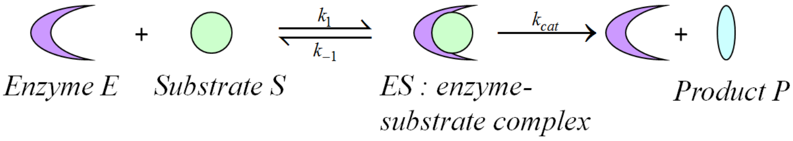

FIGURE 1.3: Scheme of Michaelis-Menten mechanism.

Applying the steady state approximation to ES we have, thanks to the Law of Mass Action:

$$\frac{\mathrm{d}\left[ES\right]}{\mathrm{d}t} = 0 = k_1\left[ES\right]\left[S\right] - k_{-1}\left[ES\right] - k_{cat}\left[ES\right]$$

and writing the total enzyme conservation,

$$\left[E\right]_0 = \left[E\right] + \left[ES\right]$$

$\left[E\right]_0$ is the total enzyme concentration and $\left[E\right]$ is the amount of free enzyme. Substituting $\left[E\right]$ it comes,

$$\left[ES\right] = \frac{k_1\left[E\right]_0\left[S\right]}{k_{-1} + k_{cat} + k_1\left[S\right]}$$

The overall rate of reaction is then found from the rate of formation of product P.

$$v = \frac{\mathrm{d}\left[P\right]}{\mathrm{d}t} = k_{cat}\left[ES\right] = \frac{k_{cat}k_1\left[E\right]_0\left[S\right]}{k_{-1} + k_{cat} + k_1\left[S\right]}$$

This expression is often written :

$$v = \frac{v_{max}\left[S\right]}{K_M + \left[S\right]}$$

where $K_M = \frac{k_{cat}+k_{-1}}{k_1}$ is called the Michaelis constant and $v_{max} = k_{cat}\left[E\right]_0$ is the maximum rate reached when the substrate is present in large excess when $\left[S\right] \gg K_M$, under these conditions the enzyme is saturated with substrate. k_{cat} is known as the turnover number, it represents the maximum number of molecules that an enzyme can convert into products per second. When $\left[S\right] \ll K_M$, the reaction rate becomes $v = \frac{k_{cat}}{K_M}[E]_0[S]$, and the rate is first order in both the initial concentration of enzyme $\left[E\right]_0$ and the substrate concentration $\left[S\right]$. The rate constant $\frac{k_{cat}}{K_M}$ traduces the enzyme efficiency.

Therefore the rate of enzyme-catalysed reaction (enzymolysis) depends on the substrate concentration according to figure 1.4. We can also notice that K_M represents the concentration needed to reached half of the maximal rate.

Many enzyme-catalysed reactions are found experimentally to follow the Michaelis-Menten equation. For instance the enzymes Ahp and catalase have been reported to

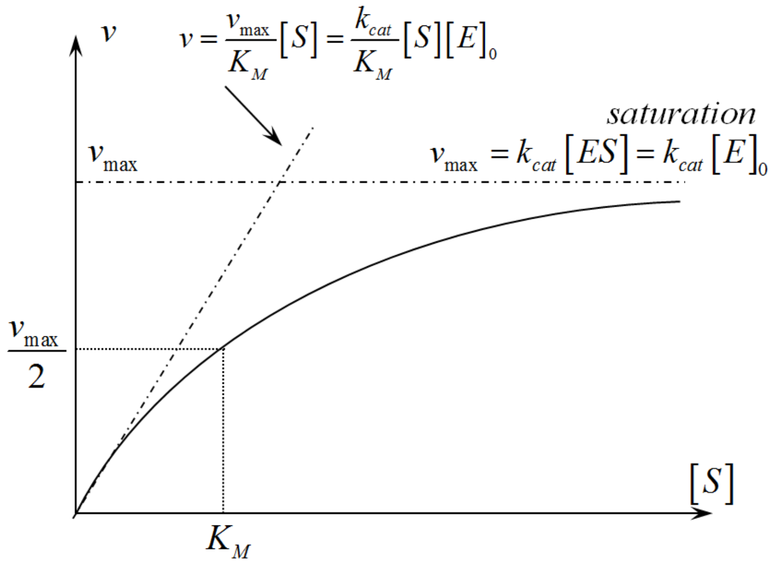

FIGURE 1.4: Evolution of enzymolysis with the substrate concentration (Michaelis-Menten hyperbole).

obey such a kinetic [10, 11].

1.3 Analytical resolution

A rate law leads to a differential equation that describes the rate of change of reactant concentrations with time. The integration of the rate law gives an expression for the concentrations as function of time. In simple cases, the rate law may be integrated analytically. Otherwise, numerical (computer based) techniques may be used.

For instance, $O_2^{\bullet -}$ *in vivo* production is a zeroth order reaction $\emptyset \xrightarrow{k_1} O_2^{\bullet -}$ of rate constant k_1 and its dismutation catalysed by superoxide dismutase SOD is a first order reaction $O_2^{\bullet -} \xrightarrow[SOD]{k_2} H_2O_2$. These equations lead to the differential equation :

$$\frac{\mathrm{d}\left[O_2^{\bullet -}\right]}{\mathrm{d}t} = k_1 - k_2[SOD]\left[O_2^{\bullet -}\right]$$

Its resolution easily gives:

$$\left[O_2^{\bullet -}\right](t) = \frac{k_1}{k_2[SOD]}\left(1 - \exp(-k_2[SOD]t)\right)$$

This analytical expression of the concentration helps us to understand its evolution. Here $O_2^{\bullet -}$ concentration rapidly (exponentially) increases near a steady state concentration $\frac{k_1}{k_2[SOD]}$. The characteristic time of the $O_2^{\bullet -}$ evolution is $\frac{1}{k_2[SOD]}$.

In order to simplify the rate law, we can sometimes apply the isolation method when one reactant is in large excess. Let us consider a hypothetical elementary process $A + B \rightarrow products$, in which B is present at a concentration 100 times greater than A. When all of compound A has been used up, the concentration of B has only decreased by $1/100$, and so 99 % of the original B is still present in solution. We therefore consider a good approximation to treat its concentration as constant throughout the reaction. The rate law can be simplified :

$$v = k[A][B] \approx k[A][B]_0 = k_{app}[A] \quad \text{with} \quad k_{app} = k[B]_0$$

Unfortunately, complex reactions generally lead to non linear systems of differential equations which can not be solved analytically even with some approximations, which is why we need to introduce numerical and computational methods.

1.4 Numerical resolutions

There are many numerical procedures for solving ordinary differential equations (ODE) with a given initial value. The different methods find numerical approximations to the ODE. Their use is also known as « numerical integration ». Let us consider the first-order differential equation:

$$\frac{\mathrm{d}y}{\mathrm{d}t} = y'(t) = f(t, y)$$

with the initial value $y(t_0) = y_0$ where $t \in [t_0, T]$. It is a Cauchy problem [12]. The most basic explicit method for numerical integration of ordinary differential equations is the Euler method. It chooses a step size h and constructs the sequence $t_i = i \cdot h$ for $i \in [\![0, N]\!]$ where $N = \lfloor (T - t_0)/h \rfloor$. N represents the number of points where the numerical method will propose its approximation. The Euler method replaces the derivative y' by the finite difference approximation :

$$y'(t_n) = \lim_{h \to 0} \frac{y(t_n + h) - y(t_n)}{h} \approx \frac{y(t_n + h) - y(t_n)}{h}$$

This equation leads to the numerical scheme :

$$y_{n+1} = y_n + hf(t_n, y_n)$$

where y_n is the numerical approximation of $y(t_n)$ This is an explicit method because the new value y_{n+1} is determined in terms of previous y_n already calculated.

The huge variety of chemical species, types of reaction, and the corresponding constants rate involved means that the time scale over which chemical reactions occur covers many orders of magnitude, from very slow reactions, such as diffusion through the membrane, to extremely fast reactions, such as the electron transfer processes involved in many biological systems ($e.g.$ catalase action). This large time scale leads to stiff equations and by consequence the Euler method is often not accurate enough and often suffers from problems of instability. Stiffness is often caused by the presence of different time scales in the underlying problem. By evaluating more points in the interval $[t_n, t_{n+1}]$, the numerical scheme becomes more accurate and this can lead to the family of the Rung-Kutta methods. One other idea is to evaluate y_{n+1} not only with y_n but with p previously computed value y_k with $k \in [\![n - p, n]\!]$. This yields multistep methods. These methods have been used in this thesis and are therefore developed in appendix A.

1.5 Stochastic approach

Intrinsic noise results form the probabilistic character of the (bio)chemical reactions. It is all the more important as the number of reacting molecules is low. Noise is inherent to the dynamics of (bio)chemical systems. Extrinsic noise is due to the random fluctuations in environmental parameters (temperature, pH,...). Both intrinsic and extrinsic noise lead to fluctuations in a single cell and results in cell-to-cell variability. This work uses the Gillespie algorithm ([13] and [14]). At each time interval, the reaction that occurs is chosen randomly according to the probabilities for the reaction to take place. The probabilities depend on both the number of molecules and the rate constants. The following paragraphs present this algorithm whereas a practical and original example is developed in appendix B.

1.5.1 Presentation

Chemical reactions and probabilities

Global point of view

The chemical reaction $A \rightarrow products$ (for instance degradation, isomerization, or radioactive disintegration) can be regarded as a random event; indeed since we can't predict the next event, there is no memory effect. Nevertheless, the reaction probability per unit of time is a constant k called the rate constant of the reaction. Let us consider $N_A(t)$ the number of molecules A at the time t. During the interval of time $\mathrm{d}t$ the number of reacting molecules equals the reaction probability $\mathrm{d}P = k\mathrm{d}t$ multiplied by the number of reacting molecules A, $k\mathrm{d}t \times N_A$. It involves a decrease of $-\mathrm{d}N_A$ in the number of molecules A. Then it gives the following ODE:

$$\frac{\mathrm{d}N_A}{\mathrm{d}t} = -kN_A$$

$$\text{or } \frac{\mathrm{d}\,[A]}{\mathrm{d}t} = -k\,[A]$$

$$\text{where concentration } [A] = \tfrac{N_A}{V_{sol}}\ ;$$

V_{sol} corresponds to the volume of the solution.

It is a first order kinetic.

Local point of view

Now the system is subdivided into a large number of subvolumes V_i. The decrease in the number of molecules A: $-\mathrm{d}n_{A,i}$ (the index i is associated with the subvolume where the transformation takes place) caused by a first order reaction $A \rightarrow produits$

taking place in the subvolume $n^\circ i$ during the interval of time dt is $r \cdot \mathrm{d}t \cdot V_i/\mathcal{N_A}$ where r corresponds to the macroscopic rate of the chemical reaction ($\mathcal{N_A}$ is the Avogadro number).

The kinetic rate law is $r = k\,[A]$ where $[A] = n_{A,i}/\left(\mathcal{N_A} V_i\right)$ ($n_{A,i}$ is the number of molecules A in the subvolume i). The decrease traduces the reaction propensity in the subvolume V_i, it is $k \cdot n_{A,i} \cdot \mathrm{d}t$. This reaction propensity is all the greater as the number of molecules is important or as the rate constant is high. The microscopic kinetic rate is defined by $v_{r,i} = -\frac{\mathrm{d}n_{A,i}}{\mathrm{d}t} = k \cdot n_{A,i}$. If a reaction occurs in the subvolume i, $n_{A,i}$ decreases by one and the number of product increases by one. A chemical reaction only affects the subvolume i and the neighbours remain unchanged.

In a second order elementary process: $A + B \to produits$, the kinetic rate law is $r = k \cdot [A] \cdot [B] = \frac{k}{\mathcal{N_A}^2 V_i^2} \cdot n_{A,i} \cdot n_{B,i}$ in subvolume i. The reaction propensity is then $v_{r,i} = -\frac{\mathrm{d}n_{A,i}}{\mathrm{d}t} = \frac{k}{\mathcal{N_A} V_i} \cdot n_{A,i} \cdot n_{B,i}$.

Diffusion and probability

With a local point of view, the diffusion of a molecule A is regarded as a first order reaction. Indeed, it is a random phenomenon without effect of memory. Let us consider a hypothetical two-dimensional reaction $A_i \to A_{i\pm1}$ where A_i represents the molecule A_i in the subvolume i and $A_{i\pm1}$ the molecule in a adjoining subvolume, on the right (+1) or on the left (-1) in a one-dimensional approach (using axis x). For instance, the probability of A diffusing from the subvolume i to the adjoining subvolume $i+1$ during the interval of time dt is $\mathrm{d}p_{d,i\to i+1} = k_d \cdot \mathrm{d}t$, This transformation decreases the number of A in the subvolume i during dt by $k_d \cdot n_{A,i} \cdot \mathrm{d}t$.

Remarks: In a homogeneous reaction medium k_d is constant and is therefore independent on the subvolume, but in an inhomogeneous medium k_d depends on the subvolume. Consequently, we have to add an index for the rate constant $k_{d,i}$ in the subvolume i.

The global variation of A takes into account its diffusion from the subvolumes i to the subvolume $i \pm 1$ but it also considers the diffusion from the subvolumes $i \pm 1$ to i.

We have (illustrated in figure 1.5):

$$\mathrm{d}n_{A,i} = \underbrace{\mathrm{d}p \cdot n_{A,i+1}}_{coming\,from\ i+1} - \underbrace{2\mathrm{d}p \cdot n_{A,i}}_{going\,to\ i\pm1} + \underbrace{\mathrm{d}p \cdot n_{A,i-1}}_{coming\,from\ i-1}$$

$\mathrm{d}p_{d,i\to i+1} = \mathrm{d}p$ is independent of the subvolume

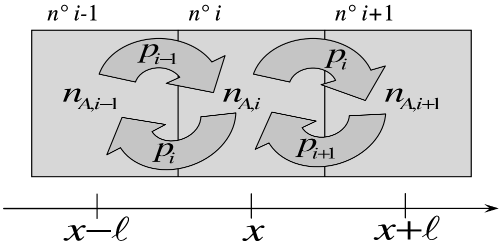

FIGURE 1.5: Scheme of diffusion jump in a one-dimensional system.

We can also write:

$$\mathrm{d}n_{A,i} = k_d \left(n_{A,i+1} - 2n_{A,i} + n_{A,i-1}\right) \mathrm{d}t$$

If ℓ represents the subvolume width:

$$\mathrm{d}n_{A(x,t)} = k_d \ell^2 \left(\frac{n_A\left(x+\ell,t\right) - 2n_A\left(x,t\right) + n_A\left(x-\ell,t\right)}{\ell^2} \right) \mathrm{d}t$$

furthermore $\lim\limits_{\ell\to 0} \frac{n_A(x+\ell,t)-2n_A(x,t)+n_A(x-\ell,t)}{\ell^2} = \frac{\partial^2 n_A(x,t)}{\partial x^2}$

Then we find the diffusion equation:

$$\frac{\partial n_A}{\partial t} = D_A \frac{\partial^2 n_A}{\partial x^2} \text{ where } k_d = \frac{D}{\ell^2}$$

In conclusion, diffusion is treated in a similar way to a first order reaction with a rate constant $k_d = D/\ell^2$. If a species A diffuses, we have to reduce by one the number of molecules in the subvolume i and to increase by one an adjoining subvolume $i+1$ or $i-1$ randomly shot.

1.5.2 Algorithm

The idea consists in determining the subvolume where the next event will occur: a reaction or a diffusion. The system is subdivided into N_T subvolumes. For instance, a bi-dimensional description will provide $n \times p$ subvolumes for $i \in 1...np$.

Description

Initialization

- Generate a connectivity matrix (figure 1.6) that describes the geometry of the system. It indicates the neighbouring subvolumes.

- Distribute the initial numbers of molecules in the N_T subvolumes. The distribution is stored in a configuration list of N_T elements.

- Calculate the sum $v_{R,i}$ of reaction rates over all subvolumes: $v_{R,i} = \sum_k^{reactions} V_i \mathcal{N_A} \cdot r_{k,i}$.

- Calculate the sum $v_{D,i}$ of diffusion rates over all molecules A_k for each subvolume $v_{D,i} = N_D \cdot \sum_k^{molcules} k_{d,k} n_{k,i}$ (n_k represents the number of molecules A_k). N_D is the number of directions in which molecules can diffuse (for instance 4 directions in a bi-dimensional system or 6 in a 3D system). $k_{d,k} = \frac{D_k}{\ell^2}$ and D_k is the diffusion coefficient of a molecule A_k.

- Each subvolume is associated with the characteristic time of the next event calculated according to the Gillespie formula ([13])

  $$\tau_i = -\frac{\ln rand_i}{v_{R,i} + v_{D,i}}$$

  where *rand*$_i$ is a random number uniformly distributed between 0 and 1 and associated with the the subvolume i

Iterations during the time experiment

- The next event occurs in the subvolume i_0 which has the lowest characteristic time τ_{i_0}. The time t_{new} of this new event is eaquivalent to $t_{new} = \tau_{i_0}$.

- We have to choose between a reaction or diffusion jump out.

- A random number (*rand*) between 0 and 1 (uniformly distributed) is chosen, if $rand < \frac{v_{R,i_0}}{v_{D,i_0}+v_{R,i_0}}$ a reaction occurs, otherwise there is a molecule diffusion.

  - *Assuming a reaction*

    Which reaction occurs ? In a similar way, a random draw chooses the k^{th} reaction if:

    $$\frac{\sum_{j=1}^{k-1} r_{j,i_0}}{\sum_{j=1}^{reactions} r_{j,i_0}} < rand \leq \frac{\sum_{j=1}^{k} r_{j,i_0}}{\sum_{j=1}^{reactions} r_{j,i_0}} \text{ considering } \sum_{j=1}^{k-1} r_{j,i} = 0 \text{ for } k = 1$$

  - *Assuming a diffusion*

    Which chemical species jumps ? By comparison with the diffusion rates, a random draw gives the diffusion jump out of the k^{th} species if:

    $$\frac{\sum_{j=1}^{k-1} k_{d,j} n_{j,i_0}}{\sum_{j=1}^{molecules} k_{d,j} n_{j,i_0}} < rand \leq \frac{\sum_{j=1}^{k} k_{d,j} n_{j,i_0}}{\sum_{j=1}^{molecules} k_{d,j} n_{j,i_0}}$$

    where $\sum_{j=1}^{k-1} k_{d,j} n_{j,i_0} = 0$ for $k = 1$.
    Then a neighbouring subvolume i_V is randomly chosen among the $2N$ neighbouring subvolumes (according to the N-dimension of the problem).

- Considering the event which occurs in the subvolume i_0, we have to modify the number of molecules in the subvolume i_0 but also in the neighbouring subvolume i_V if there was diffusion jump out.

- Finally we recalculate the new values τ_{i_0} et τ_{i_V} according to Gillespie:

$$\tau_{i_0}^{next} = \tau_{i_0} - \frac{\ln rand}{v_{R,i_0} + v_{D,i_0}} \quad \text{and} \quad \tau_{i_V}^{next} = \tau_{i_0} - \frac{\ln rand'}{v_{R,i_V} + v_{D,i_V}}$$

1.5.3 The connectivity matrix

For a rectangular bi-dimensional system with $n \times p$ subvolume, each of them has 4 neighbours, north, south, east, west (except on boundaries). The connectivity matrix helps us to identify the 4 neighbouring subvolumes' indices. The matrix dimension is therefore (4, $n \times p$). The i^{th} column stores the indices of the four neighbouring subvolumes of the i^{th} subvolume. Subvolume boundaries do not have 4 neighbours, therefore the subvolume index is duplicated.

The number of the i^{th} molecules is stored in a list of $n \times p$ elements. There are equal numbers of lists and species.

Considering a 3D-system, we have m pages, n columns and p rows which describe subvolumes indexes. In figure (1.6) $n = 3$, $p = 2$ and $m = 4$. For instance, the subvolume with index 8 is surrounded by subvolumes with indices 7, 9, 11, 14 and 2.

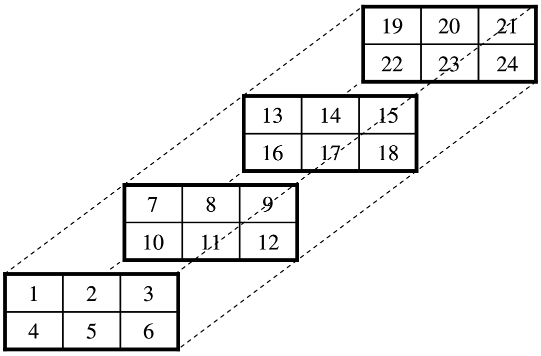

FIGURE 1.6: Example of subvolume index organization in a 3D system.

1.5.4 An application

The simplest system considers a first order reaction of decomposition of a set of molecules A in a 2D-medium without diffusion. The kinetic law gives : $\frac{\mathrm{d}N_A}{\mathrm{d}t} = -kN_A$ then $N_A = N_0 e^{-kt}$ where N_0 is the initial number of A and k (here we chose $k = 1\ \mathrm{s}^{-1}$) the rate constant. The figure 1.7 compares the analytical and stochastic results which are very close and confirm the efficiency of the algorithm. Figure 1.8 shows a graphical distribution of the molecules. In the initial configuration all molecules are black, after its decomposition the molecule disappears and becomes white.

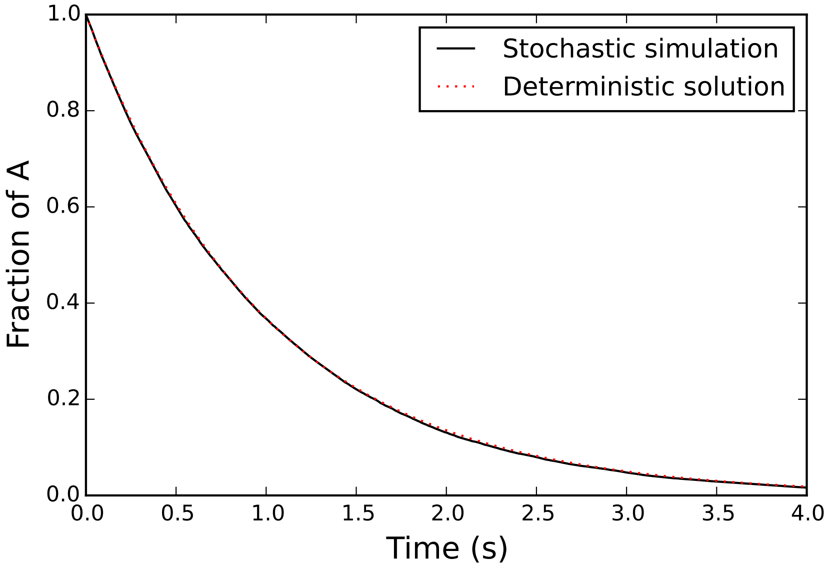

FIGURE 1.7: Evolutions of the reactant fraction for a first order reaction solved with the Gillespie algorithm and the deterministic one. The rate constant is $k = 1\ \mathrm{s}^{-1}$.

1.6 Mesoscopic reaction-diffusion models

The standard assumption for biochemical models is that the spatial distribution of reactants is homogeneous. Actually with this hypothesis, the system can be described with easy to compute ODE. Nevertheless, this assumption suffers some exceptions ([15, 16] or B). The homogeneity of the chemical component concentration depends on the diffusion rate in the cell. Instead of using ODE or PDE (partial differential equations) with finite differences, one way to handle the vast state space is to use a Monte Carlo method [17] introduced by Gillespie in 1976 ([13]).

In previous chapters we used the assumption that ROS distribution is homogeneous. Let us consider the example of H_2O_2. In order to study the influence of compartmentalization during the action of a molecule of H_2O_2 coming from outside the cell (through the membrane) and diffusing in the whole cell with a view to reacting with a substrate A, we build a hypothetical model. This model considers 40 molecules of H_2O_2 (it corresponds to 22 nM slightly above the steady state of 20 nM of H_2O_2 in *E. coli* according to Seaver and Imlay [18]) continuously coming through the membrane

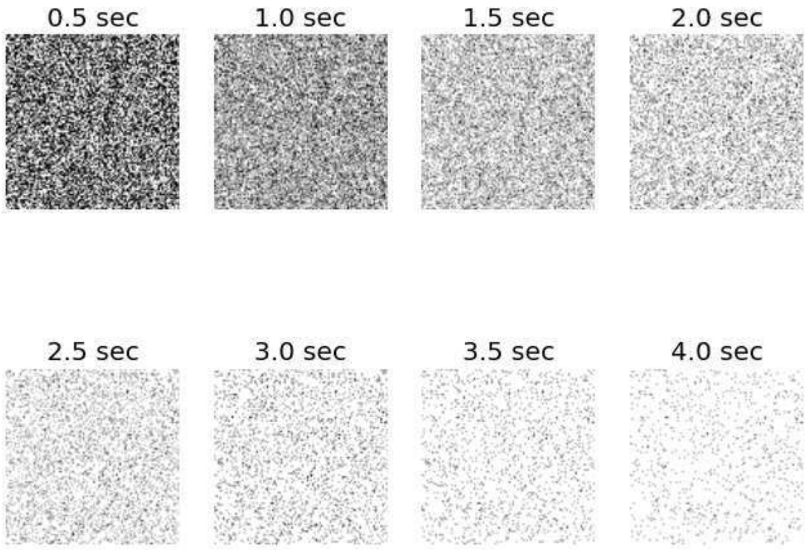

Simulation was run with a rate constant of 1 s^{-1} in a bi-dimensional square system of 100 by 100 subvolumes. The initial configuration assumes a uniform random distribution of the reactant molecule.

FIGURE 1.8: Reactant distribution in a first order reaction solved with the Gillespie algorithm.

mostly near the pole (in order to accentuate the diffusion distance) and able to diffuse in the cell. We test the reaction between H_2O_2 (cross marker in figure 1.9) and two sets of 500 molecules of substrate unable to diffuse (because compartmentalized in a fixed area of the cell), a first set of molecule A fixed near the membrane and a second set of molecule A' fixed on the centre of the cell. After a reaction between H_2O_2 and A or A', all molecules disappear but H_2O_2 is immediately reproduced coming from the membrane so that its concentration remains constant. In order to compare the effect of compartmentalization of A and A' we set the same rate constant for both reactions between H_2O_2 and A or A'.

We compare the kinetics of this hypothetical compartmentalization model with the homogeneous dynamical system referring the set of ordinary differential equations written below :

$$\begin{cases} H_2O_2 = cte \\ H_2O_2 + A \rightarrow \phi \\ H_2O_2 + A' \rightarrow \phi \end{cases} \Leftrightarrow \begin{cases} \frac{d[H_2O_2]}{dt} = 0 \\ \frac{d[A]}{dt} = -k\,[H_2O_2]\,[A] \\ \frac{d[A']}{dt} = -k\,[H_2O_2]\,[A'] \end{cases}$$

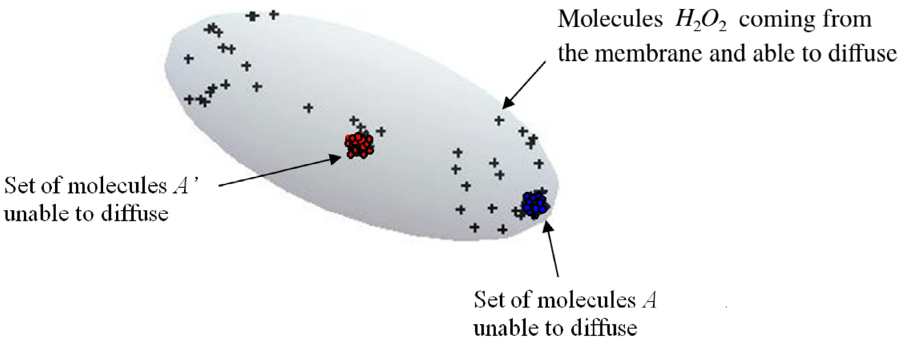
Molecules H_2O_2 coming from the membrane and able to diffuse
Set of molecules A' unable to diffuse
Set of molecules A unable to diffuse

FIGURE 1.9: Configuration of a hypothetical model of compartmentalization. 40 molecules of H_2O_2 coming through the membrane near the pole and diffusing in cell in order to react with two sets of 500 molecules of A on centre or A' near one pole.

The algorithm used for the study is the Next Sub-volume Method (NSM) the Gillespie-like method presented in the previous subsection. It approaches the spatial effects of diffusive phenomena and chemical reaction.

An example of simulation is shown in figure 1.10. This simulation shows that even if the rate constant is high (10^5 M^{-1}.s^{-1}), the diffusion is fast enough to make the compartmentalization negligible. Moreover, H_2O_2 generally reacts with rate constant lower than 10^2 M^{-1}.s^{-1} ([19].

According to the Next Sub-volume Method, the side length ℓ of the square sub-volumes has to satisfy the two inequalities

$$R \ll \ell \text{ and } \frac{\ell^2}{6D} \ll \tau_{\min}$$

where R is the larger protein radius and D the smallest diffusion constant

The first inequality indicates that dissociation events can be properly defined within sub-volumes. The second criterion specifies that the time for any molecule to leave a sub-volume is much smaller than the shortest reaction time τ_{min} among the molecular species, so that all molecules are homogeneously distributed within the sub-volumes.

The 3D simulations were performed with $\ell = 0{,}1$ μm and the depth $h = \ell$ of the sub-volumes, which is many times larger than the average protein radius.

As H_2O_2 molecules number is a constant, the reaction follows a first order kinetic with rate constant $k' = k\,[H_2O_2]$. $[H_2O_2] = \frac{N}{\mathcal{N_A}V}$ (the Avogadro constant $\mathcal{N_A} \approx 6.10^{23}$

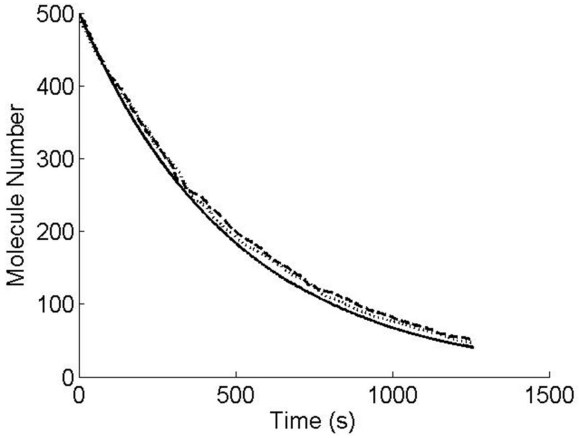

FIGURE 1.10: Decrease in molecules A by reaction with H_2O_2 according to 3 models : solid line corresponds to homogeneous repartition of A and H_2O_2 (solved with a deterministic ODE description), dotted line corresponds to the compartmentalization model with the fixed set of A on the centre of the cell and dash line corresponds to the compartmentalization model with the fixed set of A' near the pole. The rate constant is 10^5 $\text{M}^{-1}.\text{s}^{-1}$ and initially there are 40 molecules of H_2O_2 (which remain constant) and 500 molecules of A.

mol^{-1}). Considering $N = 40$ molecules of H_2O_2 in the sub-volume $V = \ell^3 = 10^{-18}$ L, the concentration is then $c \approx 70\,\mu$mol.L^{-1} and the characteristic time is therefore $\tau = 1/k' \approx 700$ s.

With usual diffusion constant D larger than 10^{-15} m^2.s^{-1}, the second inequality is respected. For instance, water diffusion constant is 10×10^{-9} m^2.s^{-1}

In conclusion, while studying reactive oxygen species we will assume for biochemical reactions that the spatial distribution of reactants is homogeneous. Nevertheless this assumption cannot explain compartmentalization effects such as DnaK action. Indeed, DnaK initially localized on foci, quickly diffuses during alcoholic stress in order to interact with abnormal protein. DnaK is then located on the abnormal protein aggregate and finally goes back to foci. We developed a model using stochastic methods to understand DnaK action in appendix B. This study is parenthetical to our work, used to complete experimental data realised by our team (Audrey Dumont unpublished data).

1.7 Organization and aim of the Thesis

The aim of the thesis is to improve understanding and knowledge of the ROS dynamic and oxidative stress consequences on cell fate. We first examine behaviour of global cells towards endogenous (the 3 ROS) or exogenous (principally H_2O_2) oxidative stress with a deterministic approach and then, thanks to this first approach we focus on the fate of the single cell from a stochastic angle which is more appropriate to small systems. Moreover our knowledge of thee behaviour of cell colonies will help us to examine the single cell more closely.

1.7.1 Hydrogen peroxide mode of action

Imlay and Linn [20] show that exposure of logarithmically growing *Escherichia coli* to hydrogen peroxide (H_2O_2) leads to two kinetically distinguishable modes of cell killing. Mode one killing is pronounced near 1 mM concentration of H_2O_2 and is caused by DNA damage, whereas mode two killing requires higher concentration ($>$ 10 mM). The second mode seems to be essentially due to damage to all macromolecules. This phenomenon has also been observed in Fenton *in vitro* systems with DNA nicking caused by hydroxyl radical ($HO^\bullet$) [21].

To our knowledge, there is currently no mathematical model for predicting mode one killing *in vitro* or *in vivo* after H_2O_2 exposure. Moreover, mode-one death has not previously been explained. Imlay and Linn [20] suggested that perhaps the amount of the toxic species was reduced at high concentrations of H_2O_2 because hydroxyl (or other) radicals might be quenched directly by hydrogen peroxide with the concomitant formation of superoxide anion (a less toxic species). We will first re-examine this assertion both *in vitro* and *in vitro*.

We have then proposed a simple model, using *Escherichia coli* as a model organism and a set of ordinary differential equations. Using this model, and testing multiple parameters we particularly focused on available iron and cell density, two factors potentially involved in ROS dynamics.

1.7.2 The major defences relative roles against hydrogen peroxide

We then investigated the relative contributions of the various reactions to the dynamic system and searched for approximate analytical solutions for the explicit expression of changes in H_2O_2 internal or external concentrations. Although the key actors in cell defence are enzymes and membrane, we asked what was their involvement with increasing H_2O_2 concentration level. We examined the ratio between maximal external H_2O_2 and internal H_2O_2 concentration. Based on these analyses and in order to introduce a concept of dose response relationship for H_2O_2-induced cell death, we developed the concepts of "maximal internal H_2O_2 concentration" and "cumulative internal H_2O_2 concentration" (e.g. the total amount of H_2O_2).

1.7.3 ROS in single cell

In the previous studies, we considered a large set of cells, so the system was described with a large number of molecules and chemical reactions could proceed in a deterministic manner. However, in a single cell, only a few types of molecules exist, therefore stochastic effects can become predominant. Many questions remain about the origin and generation of noise particularly in gene expression. Stochastic switches in bacteria can offer a explanation, as bacteria respond to environmental stress by inducing the expression of adaptive genes. Using *E. coli* as a model organism, and considering only elementary chemical stochasticity we study ROS distribution for cells in physiological conditions.

Bibliography

[1] M. Jimenez-Del-Rio and C. Velez-Pardo, "The bad, the good, and the ugly about oxidative stress", Oxidative medicine and cellular longevity, vol. 2012, 2012.

[2] C. C. Winterbourn, "Proceedings of the international congress of toxicology - vii toxicity of iron and hydrogen peroxide: The fenton reaction", Toxicology Letters, vol. 82, pp. 969–974, 1995.

[3] R. V. Lloyd, P. M. Hanna, and R. P. Mason, "The origin of the hydroxyl radical oxygen in the fenton reaction", Free Radical Biology and Medicine, vol. 22, no. 5, pp. 885–888, 1997.

[4] P. Jaruga, H. Rodriguez, and M. Dizdaroglu, "Measurement of 8-hydroxy-2-deoxyadenosine in DNA by liquid chromatography /mass spectrometry", Free Radical Biology and Medicine, vol. 31, no. 3, pp. 336–344, 2001.

[5] G. Minotti and S. D. Aust, "The role of iron in oxygen radical mediated lipid peroxidation", Chemico-Biological Interactions, vol. 71, no. 1, pp. 1–19, 1989.

[6] J. A. Imlay, "The molecular mechanisms and physiological consequences of oxidative stress: Lessons from a model bacterium", Nature Reviews Microbiology, vol. 11, no. 7, pp. 443–454, 2013.

[7] U. Jakob, W. Muse, M. Eser, and J. C. Bardwell, "Chaperone activity with a redox switch", Cell, vol. 96, no. 3, pp. 341–352, 1999.

[8] S. Arrhenius, Uber die Dissociations arme und den Einfluss der Temperatur. Wilhelm Engelmann, 1889.

[9] L. Michaelis and M. M. Menten, "The kinetics of invertin action. 1913", FEBS Lett., vol. 587, no. 17, pp. 2712–2720, Sep. 2013.

[10] L. C. Seaver and J. A. Imlay, "Hydrogen peroxide fluxes and compartmentalization inside growing Escherichia coli", J. Bacteriol., vol. 183, no. 24, pp. 7182–7189, Dec. 2001.

[11] A. Hillar, B. Peters, R. Pauls, A. Loboda, H. Zhang, A. G. Mauk, and P. C. Loewen, "Modulation of the activities of catalase-peroxidase HPI of Escherichia coli by site-directed mutagenesis", Biochemistry, vol. 39, no. 19, pp. 5868–5875, May 2000.

[12] J. Hadamard, Lectures on Cauchy's Problem in Linear Partial Differential Equations. New Haven: Yale University Press, 1923.

[13] D. T. Gillespie, "A general method for numerically simulating the stochastic time evolution of coupled chemical reactions", J. Comp. Phys., vol. 22, no. 4, pp. 403–434, Dec. 1976.

[14] ——, "Exact stochastic simulation of coupled chemical reactions", J. Phys. Chem., vol. 81, no. 25, pp. 2340–2361, Dec. 1977.

[15] M. Howard and A. D. Rutenberg, "Pattern formation inside bacteria: fluctuations due to the low copy number of proteins", Phys. Rev. Lett., vol. 90, no. 12, p. 128 102, Mar. 2003.

[16] M. B. Elowitz, M. G. Surette, P. E. Wolf, J. B. Stock, and S. Leibler, "Protein mobility in the cytoplasm of Escherichia coli", J. Bacteriol., vol. 181, no. 1, pp. 197–203, Jan. 1999.

[17] N. Metropolis and S. M. Ulam, "The monte carlo method", Journal of the American Statistical Association, vol. 44, no. 247, pp. 335–341, Sep. 1949.

[18] L. C. Seaver and J. A. Imlay, "Hydrogen peroxide fluxes and compartmentalization inside growing Escherichia coli", J. Bacteriol., vol. 183, no. 24, pp. 7182–7189, Dec. 2001.

[19] S. L. H. H., “Kinetic measurements of the reactivity of hydrogen peroxide and ozone towards small atmospherically relevant aldehydes, ketones and organic acids in aqueous solutions”, Atmos. Chem. Phys., vol. 14, pp. 4503–4514, 2014.

[20] J. A. Imlay and S. Linn, “Bimodal pattern of killing of dna-repair-defective or anoxically grown escherichia coli by hydrogen peroxide.”, Journal of bacteriology, vol. 166, no. 2, pp. 519–527, 1986.

[21] J. A. Imlay, S. M. Chin, and S. Linn, “Toxic dna damage by hydrogen peroxide through the fenton reaction in vivo and in vitro”, Science, vol. 240, no. 4852, p. 640, 1988.

Chapter 2

Hydrogen peroxide induced cell death: One or two modes of action?

Heliyon

ELSEVIER

Received:
2 November 2015
Accepted:
10 November 2015

Heliyon (2015) e00049

Hydrogen peroxide induced cell death: One or two modes of action?

Lionel Uhl, Audrey Gerstel, Maialène Chabalier, Sam Dukan *

Institut de Microbiologie de la Méditerranée – Université Aix-Marseille, Laboratoire de Chimie Bactérienne, CNRS UMR7283, 31 Chemin Joseph Aiguier, 13009 Marseille, France

* Corresponding author at: Aix-Marseille Université, Laboratoire de Chimie Bactérienne (UMR7283), Institut de Microbiologie de la Méditerranée (IMM), CNRS, 31 Chemin Joseph Aiguier, 13402 Marseille, France. Fax: +33 4 91 71 89 14; tel.: +33 4 91 16 46 01.
E-mail address: sdukan@imm.cnrs.fr (S. Dukan).

Abstract

Imlay and Linn show that exposure of logarithmically growing *Escherichia coli* to hydrogen peroxide (H_2O_2) leads to two kinetically distinguishable modes of cell killing. Mode one killing is pronounced near 1 mM concentration of H_2O_2 and is caused by DNA damage, whereas mode-two killing requires higher concentration (> 10 mM). The second mode seems to be essentially due to damage to all macromolecules. This phenomenon has also been observed in Fenton *in vitro* systems with DNA nicking caused by hydroxyl radical ($HO^\bullet$).

To our knowledge, there is currently no mathematical model for predicting mode one killing *in vitro* or *in vivo* after H_2O_2 exposure.

We propose a simple model, using *Escherichia coli* as a model organism and a set of ordinary differential equations. Using this model, we show that available iron and cell density, two factors potentially involved in ROS dynamics, play a major role in the prediction of the experimental results obtained by our team and in previous studies. Indeed the presence of the mode one killing is strongly related to those two parameters.

To our knowledge, mode-one death has not previously been explained. Imlay and Linn (Imlay and Linn, 1986) suggested that perhaps the amount of the toxic species was reduced at high concentrations of H_2O_2 because hydroxyl (or other) radicals might be quenched directly by hydrogen peroxide with the concomitant formation

http://dx.doi.org/10.1016/j.heliyon.2015.e00049
2405-8440/© 2015 The Authors. Published by Elsevier Ltd. This is an open access article under the CC BY-NC-ND license (http://creativecommons.org/licenses/by-nc-nd/4.0/).

2.1 Introduction

The principal reactive oxygen species (ROS) — superoxide $O_2^{\bullet -}$, hydrogen peroxide H_2O_2, and the hydroxyl radical $HO^{\bullet}$ — are generated by sequential reductions of molecular oxygen and are continually produced in cells. Oxidative stress results from an imbalance between exposure to ROS and defences against ROS, potentially causing damage to all macromolecules [1]. There is increasing evidence to suggest that the cumulative damage caused by ROS contributes to many diseases, including age-related disorders, such as Parkinson's disease and Alzheimer's disease, and cancer [2].

The ability of bacteria to cope with these ROS species has been studied in detail [3–10]. Briefly, in *Escherichia coli*, cytoplasmic superoxide dismutases (Mn-SOD and Fe-SOD) constitute the principal system responsible for keeping $O_2^{\bullet -}$ concentration below 2 x 10^{-10} M [11]. Alkyl hydroperoxide reductase (Ahp) and catalases (KatG and KatE) keep H_2O_2 concentration below 20 nM [12]. These concentrations of these two ROS species need to be kept very low as they are linked to the formation of $HO^{\bullet}$ via the Fenton reaction ($H_2O_2 + Fe^{2+} \rightarrow HO^{\bullet} + HO^{-} + Fe^{3+}$), against which cells have no known defense [13]. Indeed, $O_2^{\bullet -}$ rapidly destroys the [4Fe-4S] clusters of dehydratases, leading to the release of reactive iron (Fe^{2+}), which may then react with H_2O_2 to generate $HO^{\bullet}$ (Fenton reaction).

Imlay and Linn [13, 14] show that exposure of logarithmically growing *E. coli* to H_2O_2 involves two kinetically modes of cell killing. Mode one killing pronounced near 1 mM concentration of H_2O_2 is caused by DNA damage, whereas mode-two killing appears with higher concentration ($>$ 10 mM) and seems to be essentially due to damage to all macromolecules.

In this study, we aimed to use *E. coli* as a model organism, to investigate *ROS* dynamics and to understand the presence or not of the first killing mode. We used data from a large number of articles dealing with enzyme or molecule concentrations, kinetic properties and chemical reaction rate constants to generate a mathematical model based on a set of ordinary differential equations relating to fundamental principles of mass balance and reaction kinetics. To our knowledge, no such mathematical model allowing the prediction of ROS concentration and explanation of mode one killing, after H_2O_2 exposure, has ever been developed before.

2.2 Materials and methods

All numerical simulations were carried out using the MATLAB ODE solver ode15s for stiff differential equations. The multistep solver ode15s is a variable order solver based on the numerical differentiation formulas.

2.3 Results and discussion

2.3.1 The key role of free iron, its decrease during oxidative stress

The first aim of this study was to determine whether *in vivo* Fe^{2+} should be taken into account as variable when trying to predict the mode one killing. Our interest in Fe^{2+} stems from its involvement in the Fenton reaction, which leads to the formation of $HO^{\bullet}$. It is therefore important to determine whether Fe^{2+} concentration can be assumed to be constant, as a first approximation, or whether it must be treated as variable, when estimating $HO^{\bullet}$ concentration. Indeed, literature shows studies considering free iron as a constant [15] and other presenting iron evolution [16].

Our study will not mention copper. Indeed although either copper or iron can reduce H_2O_2 *in vitro*, iron is the responsible species *in vivo*. Indeed, the amount of available copper may be too small. Imlay indicates that mutants that lose the ability to control copper levels exhibit normal resistance to H_2O_2 [17]. Thus, copper is liganded by the large pool of intracellular thiols (including glutathione which is in millimolar concentration) that blocks the participation of copper in $HO^{\bullet}$ formation *in vivo*. Moreover, H_2O_2 -oxidizable copper is located in the periplasm; therefore, most of the copper-mediated hydroxyl radical formation occurs in a compartment far away from DNA.

A simple in vitro system

The simplest *in vitro* system was proposed by Luo *et al.* [18] only considering 80 nM of Fe^{2+} and 17 μM DNA. They show that DNA nicking is maximal at 0.05 mM H_2O_2 concentration after a 7.5 minutes experiment.

The chemical reactions which describe this system are :

$$\begin{array}{ll} Fe^{2+} + H_2O_2 \xrightarrow{k_F} Fe^{3+} + HO^- + HO^\bullet & \text{(Fenton reaction)} \\ HO^\bullet + H_2O_2 \xrightarrow{k_Q} O_2^{\bullet -} + H_2O + H^+ & \text{(Quenching reaction by } H_2O_2\text{)} \\ HO^\bullet + DNA \xrightarrow{k_{DNA}} products & \text{(DNA nicking)} \end{array}$$

The resulting dynamical system of ordinary differential equation is :

$$\begin{aligned} \frac{\mathrm{d}\,[HO^\bullet]}{\mathrm{d}t} &= k_F\left[Fe^{2+}\right][H_2O_2] - k_Q\,[HO^\bullet]\,[H_2O_2] - k_{DNA}\,[DNA]\,[HO^\bullet] \\ \frac{\mathrm{d}\left[Fe^{2+}\right]}{\mathrm{d}t} &= -k_F\left[Fe^{2+}\right][H_2O_2] \\ \frac{\mathrm{d}\,[H_2O_2]}{\mathrm{d}t} &= -k_F\left[Fe^{2+}\right][H_2O_2] - k_Q\,[HO^\bullet]\,[H_2O_2] \\ \frac{\mathrm{d}\,[DNA]}{\mathrm{d}t} &= -k_{DNA}\,[DNA]\,[HO^\bullet] \end{aligned}$$

Taking the reaction rate constants found in literature, $k_F = 4.4 \times 10^4$ M s^{-1} [5], $k_Q = 2.7 \times 10^7$ M s^{-1} [19] and $k_{DNA} = 4.7 \times 10^9$ M s^{-1} [20], the simulation shows exactly the same maximum (figure 2.1) when reporting average DNA nicking (during time experiment) versus H_2O_2 concentration.

In this system, it is obvious that free iron decreases because there is no way of recycling; nevertheless we present a hypothetic simulation considering free iron as a constant. This hypothetic simulation realized with $\mathrm{d}\left[Fe^{2+}\right]/\mathrm{d}t = 0$ makes clear the need to take into account free iron as a variable even in a simple system in order to see mode one killing; and it also shows that iron decrease is responsible of the first killing mode. Imlay first discussion [14] concerning the quenching of $HO^\bullet$ with H_2O_2 in order to interpret mode one killing have to be forgotten. The quenching only slows down the DNA oxidation (caused by $HO^\bullet$) but it cannot be responsible for the mode one killing.

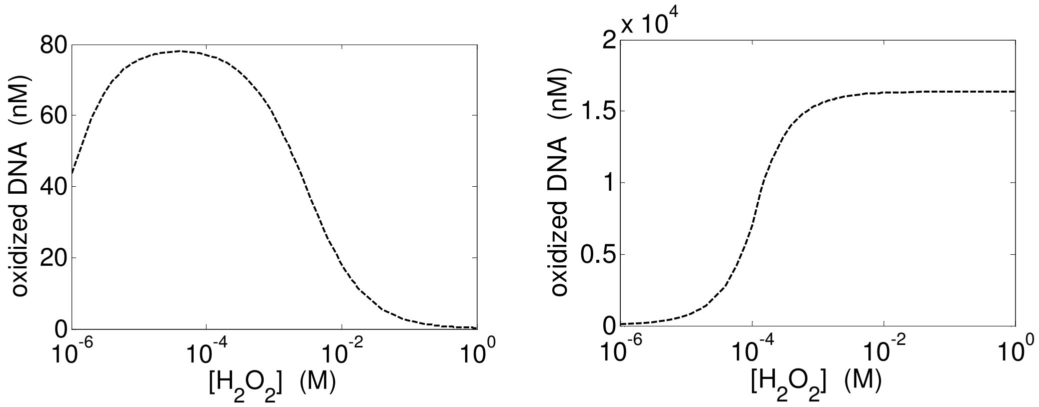

FIGURE 2.1: Simulation for H_2O_2-mediated mode 1 killing (left panel) in a Fenton system obtained with 80 nM of Fe^{2+} and 17 μM DNA. Mode one killing disappear (right panel) when free iron is artificially taken constant (the dynamical system has been modified by taken $\mathrm{d}\left[Fe^{2+}\right]/\mathrm{d}t = 0$).

2.3.2 Mathematical analysis of the in vivo Fenton system

DNA nicking involves a reaction between DNA and $HO^\bullet$, therefore, in order to see mode one killing, $HO^\bullet$ concentration must reach a maximum as a function of exogenous H_2O_2 concentration. Considering *in vivo* Fenton system we have to take into account H_2O_2 scavenging enzyme (Alkyl hydroperoxide reductase and catalases). Let us examine whether this system is consistent with a maximum level of $HO^\bullet$ concentration when challenging H_2O_2. Our model does not take into account molecules compartmentalization.

$HO^\bullet$ depends on time t and $[H_2O_2]_{out}$ (exogenous H_2O_2 concentration). If $HO^\bullet$ reaches a maximum value, that implies that a mathematical derivative of $HO^\bullet$ versus $[H_2O_2]_{out}$ reached zero. Before evaluating $\frac{\mathrm{d}[HO^\bullet]}{\mathrm{d}[H_2O_2]_{out}}$, we need to know how $HO^\bullet$ levels change.

The most important cellular sinks for hydroxyl radical are reactions with major cellular components like proteins, metabolomes,... The quenching reaction (with H_2O_2) may be relevant under *in vitro* conditions when H_2O_2 concentration is very high (and DNA concentration very low), but under a physiological setting or even when cells are exposed to external H_2O_2, H_2O_2 will not be a major sink for hydroxyl radical. Indeed, reaction rate constant of $HO^\bullet$ between organic cellular compounds (like proteins, metabolomes,...) are closed to diffusion limit rate constant $k_{diff} \approx 10^{10}$ M^{-1} s^{-1} and organic cellular compounds concentration $[Organic]$ is higher than 10 mM, therefore under the mode one killing where H_2O_2 concentration is under 4 mM, we can write the inequality :

$$\frac{v_{organic\ sinks}}{v_{quenching}} = \frac{k_{diff}\,[Organic]\,[HO^\bullet]}{k_Q\,[H_2O_2]\,[HO^\bullet]} = \frac{k_{diff}\,[Organic]}{k_Q\,[H_2O_2]} \approx 10^3 \gg 1$$

This inequality means that the quenching reaction can be neglected in the study of mode one killing.

Moreover, concerning $HO^\bullet$ production, we do not consider Haber-Weiss reaction, a reaction whose relevance *in vivo* is questionable [21, 22]. In fact, when adding this reaction, we saw no significant change in ROS or DNA kinetic. Therefore, within cells, for a given exogenous H_2O_2 concentration, $HO^\bullet$ levels obey the following reactions:

$$\begin{array}{ll} Fe^{2+} + H_2O_2 \xrightarrow{k_F} Fe^{3+} + HO^- + HO^\bullet & \text{formation (Fenton reaction)} \\ HO^\bullet + X_i \xrightarrow{k_i} products & \text{consumption by a molecule} X_i \end{array}$$

In vivo, because $HO^\bullet$ reacts with various molecules we generalise the system and demonstrate that we need to consider available iron as a variable.

Proof by contradiction (*reductio ad absurbum*): Suppose that free iron is constant.

Considering N reactions (of rate constant k_i between an organic X_i compound and $HO^\bullet$) and assuming X_i concentration is constant because X_i is in large excess (for example DNA, proteins, metabolomes,...). Therefore $HO^\bullet$ levels obey the following kinetic differential equation:

$$\frac{\mathrm{d}\,[HO^\bullet]}{\mathrm{d}t} = k_F\left[Fe^{2+}\right][H_2O_2] - \sum_{i=1}^{N} k_i\,[HO^\bullet]\,[X_i]$$

The resolution of this equation gives:

$$[HO^\bullet] = \left(\int_0^t k_F\left[Fe^{2+}\right][H_2O_2]\exp\left(\sum_{i=1}^{N} k_i\,[X_i]t'\right)\mathrm{d}t'\right)\exp\left(-\sum_{i=1}^{N} k_i\,[X_i]t\right) \qquad (*)$$

Internal H_2O_2 concentration is also dependent on t and $[H_2O_2]_{out}$, as follows:

$$[H_2O_2] = f\left(t, [H_2O_2]_{out}\right)$$

In addition, the more exogenous H_2O_2 added, the more H_2O_2 penetrates the cell, so f is a monotonic increasing function of $[H_2O_2]_{out}$ and $\frac{\partial f\left([H_2O_2]_{out}, t\right)}{\partial [H_2O_2]_{out}} > 0$. The mathematical derivative of $HO^{\bullet}$ versus $[H_2O_2]_{out}$ gives:

$$\frac{\mathrm{d}\,[HO^{\bullet}]}{\mathrm{d}[H_2O_2]_{out}} = \left(\int_0^t k_F \left[Fe^{2+}\right] \frac{\partial f\left([H_2O_2]_{out}, t'\right)}{\partial [H_2O_2]_{out}} \exp\left(\sum_{i=1}^{N} k_i\,[X_i]t'\right) \mathrm{d}t'\right) \exp\left(-\sum_{i=1}^{N} k_i\,[X_i]t\right)$$

This expression obviously indicates that $\frac{\mathrm{d}[HO^{\bullet}]}{\mathrm{d}[H_2O_2]_{out}} > 0$ because all terms are positive.

For this reason, in this model, there should be no peak when changes in $HO^{\bullet}$ levels are plotted against exogenous H_2O_2 levels. This conclusion is in contradiction with mode one killing observation, therefore we must consider Fe^{2+} concentration to decrease with increasing H_2O_2 concentration.

We can notice that a direct proof, without supposing free iron constant, gives by derivation of (*) :

$$\frac{\mathrm{d}\,[HO^{\bullet}]}{\mathrm{d}\,[H_2O_2]_{out}} = \left(\int_0^t k_F F_{(Fe^{2+}, H_2O_2)} \exp\left(\sum_{i=1}^{N} k_i\,[X_i]\,t'\right) \mathrm{d}t'\right) \times \exp\left(-\sum_{i=1}^{N} k_i\,[X_i]t\right)$$

where $F_{(Fe^{2+}, [H_2O_2])} = \left[\left[Fe^{2+}\right] \frac{\partial f\left([H_2O_2]_{out}, t'\right)}{\partial [H_2O_2]_{out}} + [H_2O_2] \frac{\partial \left[Fe^{2+}\right]}{\partial [H_2O_2]_{out}}\right]$
This expression can reach zero only if:

$$\underbrace{\left[Fe^{2+}\right]}_{>0} \underbrace{\frac{\partial f\left([H_2O_2]_{out}, t'\right)}{\partial [H_2O_2]_{out}}}_{>0} + \underbrace{[H_2O_2]}_{>0} \frac{\partial \left[Fe^{2+}\right]}{\partial [H_2O_2]_{out}} = 0$$

It demonstrates that necessarily $\frac{\partial \left[Fe^{2+}\right]}{\partial [H_2O_2]_{out}} < 0$, meaning that $\left[Fe^{2+}\right]$ is a monotonic decreasing function of $[H_2O_2]_{out}$.

So, to explain the experimental curve for DNA nicking *in vitro*, we must consider Fe^{2+} concentration to decrease with increasing H_2O_2 concentration.

Mathematical model

The first difference between *in vivo* and *in vitro* experiments is the value of H_2O_2 exogenous concentration needed to reach maximum in the mode one killing [13]. This difference is for a number of reasons. First cell membrane and cell scavenger (Ahp and catalase) reduce H_2O_2 concentration within the cell; therefore mode one killing appears with higher concentration of H_2O_2 concentration *in vivo*. Then there are many sinks for hydroxyl radical and free iron evolution has to take its recycling into account. The model has to be completed with the following equations, of course we only present the major reaction involved in the description of the mode one killing; for instance we do not add reaction between organic compounds and H_2O_2 which is negligible when compared to enzymatic dismutation. This model is deliberately simple in order to examine the predominant effects.

Internal hydrogen peroxide kinetics

$$\begin{aligned}
\frac{\mathrm{d}\,[H_2O_2]}{\mathrm{d}t} = \; & k_{prod}^{H_2O_2} && : \text{Endogenous production} \\
& -\frac{k_{cat}^{Ahp}\,[Ahp]\,[H_2O_2]}{[H_2O_2] + K_M^{Ahp}} && : \text{Dismutation by Ahp } H_2O_2 \overset{Ahp}{\longrightarrow} H_2O + {}^1\!/\!_2 O_2 \\
& -\frac{k_{cat}^{Kat}\,[Kat]\,[H_2O_2]}{[H_2O_2] + K_M^{Kat}} && : \text{Dismutation by Kat } H_2O_2 \overset{Kat}{\longrightarrow} H_2O + {}^1\!/\!_2 O_2 \\
& -k_{diff}\left([H_2O_2] - [H_2O_2]_{ex}\right) && : \text{Diffusion across cell membrane} \\
& -k_F\,[H_2O_2]\left[Fe^{2+}\right] && : \text{Fenton reaction}
\end{aligned}$$

External hydrogen peroxide concentration ($[H_2O_2]_{out}$) strongly depends on cell number (noted n), indeed, the higher cell density, the faster the media is detoxified. The cell density involvement will be discussed in section 3.

External hydrogen peroxide kinetics

$$\frac{\mathrm{d}[H_2O_2]_{out}}{\mathrm{d}t} = k_{diff}\frac{n \cdot V_{internal}}{V_{external}}\left([H_2O_2] - [H_2O_2]_{out}\right)$$

$V_{internal}$ represents intracellular solvent-accessible volume.

Cell numbers n double every 20 minutes according to an exponential law.

Hydroxyl radical kinetics

We consider N reactions of rate constant k_i between an organic X_i compound (proteins, metabolites,...) and $HO^\bullet$. Nevertheless, DNA was treated separately (out of the sum) in order to examine its damage during oxidative stress, so it comes to the following equations:

$$\frac{\mathrm{d}\left[HO^\bullet\right]}{\mathrm{d}t} = k_F\left[Fe^{2+}\right]\left[H_2O_2\right] - \sum_{i=1}^{N} k_i\left[X_i\right]\left[HO^\bullet\right] - k_{DNA}\left[DNA\right]\left[HO^\bullet\right]$$

$$\frac{\mathrm{d}\left[DNA\right]}{\mathrm{d}t} = -k_{DNA}\left[DNA\right]\left[HO^\bullet\right]$$

Recycling of free iron

Free available Fe^{2+} is oxidized during Fenton reaction but Fe^{3+} is then reduced by cellular reductants. However, the identity of the biological reductants *in vivo* remains unclear [23], Fe^{3+} might also be reduced at varying reaction rates by a range of cellular reductants, such as glutathione, L-cysteine, NAD(P)H and FADH$_2$ [24]. The kinetic of iron recycling has to take into account the fact that reductant concentrations also decrease with increasing value of exogenous concentration of H_2O_2 because of reductant reactions with various ROS. For instance Brumaghim *et al.* [25] report that *in vivo* NADH concentration reduce by half when challenging about 0.2 mM of H_2O_2 (Fig. 2.2). Therefore we corrected recycling rate with a Hill factor (noted f) of coefficient 1 (because decrease is hyperbolic) often used to describe reaction of inhibition [26]. We consider here that H_2O_2 inhibits the efficiency of the reductants to recycle Fe^{3+} into Fe^{2+} .

For instance, reduction by NADH gives the kinetic rate:

$$v_{red}^{NADH} = k_{NADH}\left[Fe^{3+}\right][NADH]$$

where $[NADH] = f_{NADH}[NADH]_0$ and $f_{NADH} = \frac{C_{1/2}^{NADH}}{[H_2O_2]+C_{1/2}^{NADH}}$ where $C_{1/2}^{NADH}$ is the H_2O_2 concentration needed to reduce by half the initial concentration of NADH. $[NADH]_0$ represents NADH concentration without oxidative stress.

Hill correction factor fits Brumaghim [25] experimental results by taking $C_{1/2}^{NADH}$ =0.2 mM (this value was found using a least square approximation).

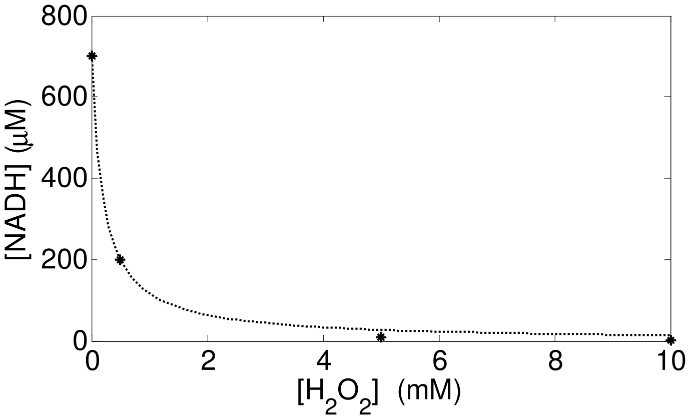

FIGURE 2.2: *in vivo* NADH levels after H_2O_2challenge of *E. coli* (* marker for Brumaghim measurements and dots for our mathematical model).

We can then write Fe^{3+} reduction kinetic rate by NADH :

$$v_{red}^{NADH} = k_{NADH}\left[Fe^{3+}\right][NADH]_0\frac{C_{1/2}^{NADH}}{[H_2O_2]+C_{1/2}^{NADH}}$$

or

$$v_{red}^{NADH} = k_{NADH}[NADH]_0\,[Fe]\,\frac{[Fe]-\left[Fe^{2+}\right]}{[Fe]}\,\frac{C_{1/2}^{NADH}}{[H_2O_2]+C_{1/2}^{NADH}}$$

because $\left[Fe^{3+}\right] = [Fe] - \left[Fe^{2+}\right]$ where $[Fe]$ represents the total free available iron concentration in cell.

We can also write

$$v_{red}^{NADH} = v_{\max}^{NADH} \frac{[Fe] - \left[Fe^{2+}\right]}{[Fe]} \frac{C_{1/2}^{NADH}}{[H_2O_2] + C_{1/2}^{NADH}}$$

where $v_{\max}^{NADH} = k_{NADH}[NADH]_0\,[Fe]$

According to Brumaghim *et al.* [25] NADH oxidation experiment, 16 μM of *in vitro* initial NADH concentration are oxidized by 80 μM of Fe^{3+} with an initial rate constant (obtained by measurement of NADH absorbance at 340 nm) $k_{NADH}\,\left[Fe^{3+}\right]$ =2.3×10^{-4} s^{-1}, so with physiological concentration, the maximal rate constant for Fe^{3+} reduction will be near $k_{NADH}[NADH]_0\,[Fe]$ =10^{-7} M s^{-1}.

Brumaghim *et al.* produce the same study with NADPH, and according to their experimental results we have $k_{NADPH}[NADPH]_0\,[Fe]$ =4×10^{-9} M s^{-1} and $C_{1/2}^{NADPH}$ =4 mM.

Moreover, cell counts many reductants like ascorbate which may represent an alternative way to generate Fe^{2+} [27]. Thiols and in particular glutathione GSH in physiological systems, are important agents responsible for helping to maintain aerobic cells in a reducing state, despite an oxidizing environment. Nevertheless, a growing body of evidence suggests that thiols, as electron donors of metal-catalyzed oxidation systems, can paradoxically be responsible for the generation of reactive oxygen species [28]. For instance, Netto and Stadtman [29] report that Dithiothreitol reduces Fe^{3+} with a constant rate near 2.5 M^{-1}s^{-1}, therefore $v_{\max}^{RSH} = k_{RSH}\,[Fe]\,[RSH]_0 \geq 10^{-6}$ M s^{-1}.

We can notice that the upper limit for $v_{\max}^{Red} = k_{Red}\,[Fe]\,[Red]_0$ is near 10^{3} M s^{-1} (using the rate constant of diffusion limited reaction which is near 10^{10} M^{-1}s^{-1}, and assuming $[Red] \leq 10^{-2}$M and $[Fe] \approx 20$ μM). Of course the real (but unknown) value should be much weaker.

By adding N reductants (noted R_i), reduction rate can be written :

$$v_{red} = \sum_{i=1}^{N} \left(v_{\max,i} \frac{[Fe] - \left[Fe^{2+}\right]}{[Fe]} \frac{C_{1/2}^{i}}{[H_2O_2] + C_{1/2}^{i}} \right)$$

Of course, we cannot find the values of all kinetic constants in literature for *in vivo* system whereas it is a crucial issue; we therefore use an average formula with only two constants:

$$v_{red} = v_{\max} \frac{C_0}{[H_2O_2] + C_0} \frac{[Fe] - \left[Fe^{2+}\right]}{[Fe]}$$

When $[H_2O_2] \to C_0$, the efficiency of the reduction is reduced by half, $v_{\max}$ represents the maximal rate of Fe^{3+} reduction, this rate is obtained in a hypothetic scheme when $[H_2O_2] \to 0$ (meaning that reductants are the most efficient at low H_2O_2 concentration) and when $\left[Fe^{2+}\right] \to 0$ (meaning that Fe^{3+} concentration is maximal).

We then have to examine the involvement of these two constants ($v_{\max}$ and C_0) on mode one killing. Finally free iron kinetic is approached to:

$$\frac{\mathrm{d}\left[Fe^{2+}\right]}{\mathrm{d}t} = -k_F \left[Fe^{2+}\right] [H_2O_2] + v_{\max} \frac{C_0}{[H_2O_2] + C_0} \frac{[Fe] - \left[Fe^{2+}\right]}{[Fe]}$$

The figure 2.3 represents the principal interactions between the reagents used in the mathematical model.

Scheme of the model

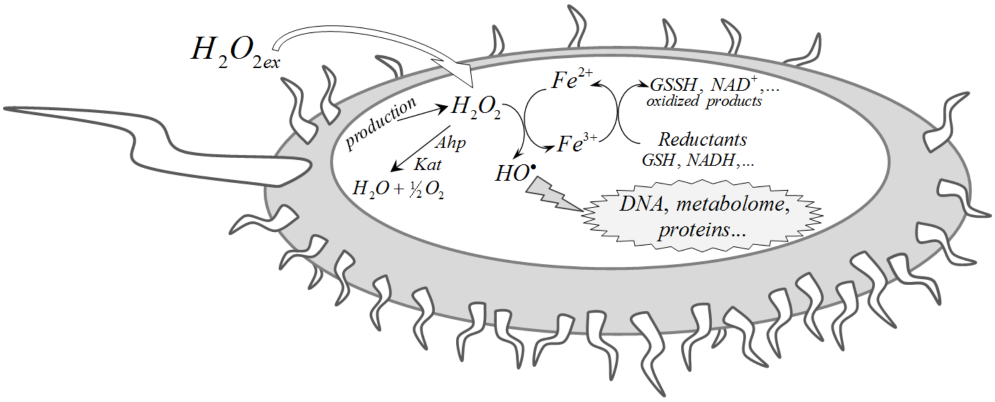
H_2O_{2ex}
production
H_2O_2
Ahp
Kat
$H_2O + ½O_2$
Fe^{2+}
Fe^{3+}
$HO^\bullet$
$GSSH$, NAD^+,...
oxidized products
Reductants
GSH, NADH,...
DNA, metabolome, proteins...

FIGURE 2.3: Scheme of ROS interaction in the mathematical model.

Choice of kinetic constants

According to Park et al. [5] experiments, at 37°C and neutral pH, the Fenton rate constant for DNA-bound iron was $k_F = 4400$ M s^{-1} but this constant is higher when iron is bound to ATP. As mode one killing concerns DNA damage, we use $k_F = 4400$ M s^{-1} for our simulation. Indeed $HO^{\bullet}$ reacts very fast and therefore only impacts the nearest organic compounds.

DNA concentration refers to nitrogenous bases concentration, this concentration is set to 5 $\times 10^{-3}$ M, corresponding to approximately 4.6 $\times 10^{6}$ pairs (with the proportion of each base set at 25 %, which is close to the value proposed by the CBS genome atlas database of Hallin and Ussery [30]).

We then consider N reactions of rate constant k_i between an organic X_i compound (or site) and $HO^{\bullet}$ ($\sum_{i=1}^{N} k_i\,[X_i]\,[HO^{\bullet}]$). For instance Bennett *et al.* [31] report total metabolome concentration of 300 mM (100 millions metabolites/cell) greatly exceeded the reported total protein concentration of 7 mM (2.4 million proteins/cell). Nevertheless, with an average of 400 residues per protein, it represents 2.8 M of feeding sites for $HO^{\bullet}$.

Using Bennett *et al.* [31] metabolome concentration and Buxton and Greenstock [19] rate constant we evaluate $\sum_{i=1}^{N} k_i\,[X_i]$. For unknown values, we set $k_i = 2 \times 10^{9}$ Mol L^{-1} s^{-1} (this value is assumed to be the *in vivo* diffusion-limited rate constant), or we use the rate constant of a similar compounds (see Table 2.1).

By adding all metabolite of this partial table 2.1 we obtain $\sum_{\substack{i=1\\ metabolomes}}^{N} [X_i] \approx 230$ mM and $\sum_{\substack{i=1\\ metabolomes}}^{N} k_i\,[X_i] \approx 243 \times 10^{6}$ s^{-1} by linear extrapolation, if $\sum_{\substack{i=1\\ metabolomes}}^{N} [X_i] \approx 230$ converge to 300 mM, then $\sum_{\substack{i=1\\ metabolomes}}^{N} k_i\,[X_i]$ will converge to 3.2×10^{8} s^{-1}.

Adding the 7×400 mM of protein residues that can react by nearly diffusion-limited rate constant (2×10^{9} M^{-1}s^{-1}), it gives $\sum_{\substack{i=1\\ proteins}}^{N} k_i\,[X_i] \approx 70 \times 10^{8}$ s^{-1}.

Finally $\sum_{\substack{i=1\\ organic}}^{N} k_i\,[X_i] \approx 73 \times 10^{8}$ s^{-1}.

We assume that $\sum_{i=1}^{N} k_i\,[X_i] \approx 7.3 \times 10^{9}$ s^{-1} (Supplementary Material A), which corresponds to a mean rate constant of 2×10^{9} M s^{-1} for reaction between $HO^{\bullet}$ and organic compounds.

Influence of the viscosity of the medium

Chemical rate constants were estimated in aqueous solutions, in which the rates of diffusion-controlled reactions are limited by viscosity to an estimated 10^{10} M s^{-1}. For our model, the first step towards approximating the cytoplasmic conditions was the re-estimation of all chemical rate constants limited by diffusion phenomena. Indeed, in a diffusion-controlled reaction, the formation of products in second-order chemical reactions occurs more rapidly than the diffusion of reactants. The rate of reaction is thus limited by collision frequency kinetics. Smoluchowski [32] suggested that the upper limit (almost 10^{10} M s^{-1} in aqueous solution) for the diffusion-limited rates of bimolecular reactions depended on molecule size and shape, but that this limit was also linearly dependent on the diffusion coefficient of the medium. According to the Stocks-Einstein equation, viscosity is one of the major parameters determining the diffusion coefficient of species in condensed media. Some experimental measurements [33–35] have indicated that the cytoplasm has a viscosity about one or two orders of magnitude greater than that of water. The diffusion coefficient and, consequently, the diffusion-limited rate of reaction, should be about one or two orders of magnitude lower (100-10 times lower) than that in water. Nevertheless, according to other measurements [36, 37], diffusion of small molecules in the cytoplasm is only 2-5 times lower than in aqueous solutions, therefore we assumed that all second-order reaction rate constants would be limited to 2×10^9 M s^{-1} in cytoplasm which is only five time less than in aqueous solution.

TABLE 2.1: Ordered kinetic rate constants and concentration of the major metabolites in *E.coli*. (*) values limited *in vivo* by the diffusion-limited rate constant assumed to be 2×10^{9} $M^{-1}s^{-1}$

Metabolites X_i	Concentration $[X_i]$ (Mol L^{-1})	Rate constant k_i (Mol L^{-1} s^{-1})	cumulative $\sum_{i=1}^{N} k_i\,[X_i]$ (10^6 s^{-1})
Glutamate	9.6×10^{-2}	2.3×10^{8}	22
Glutathione	1.7×10^{-2}	1.3×10^{10} (*)	56
Fructose-1,6-bisphosphate	1.5×10^{-2}	2.6×10^{8}	60
ATP	9.6×10^{-3}	8.9×10^{9} (*)	79
UDP-*N*-acetylglucosamine	9.2×10^{-3}	4×10^{9} for uridine (*)	97
Hexose-P	8.8×10^{-3}	1.4×10^{9} for glucose-P	115
UTP	8.3×10^{-3}	4×10^{9} for uridine (*)	131
GTP	4.9×10^{-3}	8×10^{9} for guanosine (*)	141
dTTP	4.6×10^{-3}	4.7×10^{9} for thymidine (*)	150
Aspartate	4.2×10^{-3}	7.5×10^{7}	151
Valine	4.0×10^{-3}	8.5×10^{8}	159
Glutamine	3.8×10^{-3}	8.4×10^{8}	166
6-Phosphogluconate	3.8×10^{-3}	3.0×10^{9} for gluconate (*)	174
CTP	2.7×10^{-3}	6.1×10^{9} (*)	179

Alanine	2.6×10^{-3}	7.7×10^{7}	180
NAD^{+}	2.6×10^{-3}	3.2×10^{9} (*)	185
UDP-glucose	2.5×10^{-3}	4×10^{9} for uridine (*)	190
Glutathione disulfide	2.4×10^{-3}	9.3×10^{9} (*)	194
Uridine	2.1×10^{-3}	4×10^{9} (*)	199
Citrate	2.0×10^{-3}	5×10^{7}	199
UDP	1.8×10^{-3}	4×10^{9} for uridine (*)	202
Malate	1.7×10^{-3}	8.6×10^{9} (*)	206
3-Phosphoglycerate	1.5×10^{-3}	$? \Rightarrow 2 \times 10^{9}$	209
Glycerate	1.4×10^{-3}	$? \Rightarrow 2 \times 10^{9}$	211
Coenzyme A	1.4×10^{-3}	3.1×10^{9} (*)	214
Citrulline	1.4×10^{-3}	1.2×10^{9}	217
Pentose-P	1.3×10^{-3}	1.6×10^{9} for ribose	220
Glucosamine-6-phosphate	1.2×10^{-3}	$? \Rightarrow 2 \times 10^{9}$	222
Acetylphosphate	1.1×10^{-3}	$? \Rightarrow 2 \times 10^{9}$	224
Gluconolactone	1.0×10^{-3}	1.7×10^{9}	226
GDP	6.8×10^{-4}	8×10^{9} for guanosine (*)	228

Acetyl-CoA	6.1×10^{-4}	3.1×10^{9} for CoA (*)	229
Carbamylaspartate	5.9×10^{-4}	7.5×10^{7} for aspartate	229
Arginine	5.7×10^{-4}	3.5×10^{9} (*)	230
Succinate	5.7×10^{-4}	3.1×10^{8}	230
UDP-glucuronate	5.7×10^{-4}	4×10^{9} for uridine (*)	231
ADP	5.6×10^{-4}	8.1×10^{9} (*)	232
Asparagine	5.1×10^{-4}	4.9×10^{7}	233
α-Ketoglutarate	4.4×10^{-4}	8.3×10^{8} for glutaric	233
Lysine	4.1×10^{-4}	3.5×10^{8}	234
Proline	3.9×10^{-4}	3.1×10^{8}	234
dTDP	3.8×10^{-4}	4.7×10^{9} for thymidine (*)	235
Dihydroxyacetone-P	3.7×10^{-4}	$? \Rightarrow 2 \times 10^{9}$	235
Homocysteine	3.7×10^{-4}	3.5×10^{10} (*)	236
CMP	3.6×10^{-4}	6.5×10^{9} (*)	237
Deoxyribose-5-P	3.0×10^{-4}	2.1×10^{9}	237
Isoleucine+leucine	3.0×10^{-4}	1.8×10^{9}	238
AMP	2.8×10^{-4}	4.1×10^{9} (*)	238

Inosine monophosphate	2.7×10^{-4}	2.6×10^{9} (*)	239
PRPP	2.6×10^{-4}	1.6×10^{9} for ribose	239
Succinyl-CoA	2.3×10^{-4}	3.1×10^{9} for CoA (*)	240
Inosine triphosphate	2.1×10^{-4}	4×10^{9} for inosine	240
Guanine	1.9×10^{-4}	9.2×10^{9} (*)	241
Phosphoenolpyruvate	1.8×10^{-4}	3.7×10^{7} for pyruvate	241
S-Adenosyl-L-methionine	1.8×10^{-4}	8.5×10^{9} for methionine (*)	241
Threonine	1.8×10^{-4}	5.1×10^{8}	241
FAD	1.7×10^{-4}	$? \Rightarrow 2 \times 10^{9}$	242
Methionine	1.5×10^{-4}	8.5×10^{9} (*)	242
2,3-Dihydroxybenzoic acid	1.4×10^{-4}	$? \Rightarrow 2 \times 10^{9}$	242
NADPH	1.2×10^{-4}	$? \Rightarrow 2 \times 10^{9}$	242
Fumarate	1.2×10^{-4}	6.0×10^{9} (*)	243
Phenylpyruvate	9.0×10^{-5}	$? \Rightarrow 2 \times 10^{9}$	243

Position and width of mode one killing

Position of mode one killing corresponds to the concentration of H_2O_2 where the maximum of DNA damage occurs. Position and width of mode one killing of course depend on reaction rate constants and in particular on the recycling rate of free iron characterized by $v_{\max}$ and C_0. Mode one killing can also be described by its intensity (DNA oxidized proportion) but it is impossible to directly link bacterial survival curve to intensity of DNA oxidized proportion whereas survival bacterial curve should occur at the same position and should present approximately the same shape. Therefore we focus on the position and the width of mode one killing. We previously show the particular importance of iron evolution; therefore we will next focus on the two parameters $v_{\max}$ and C_0 introduced to describe its kinetic.

The influence of $v_{\max}$

For next simulations we set $C_0 = 1\text{mM}$ (the influence of this constant will be discussed later) and we observe the influence of the parameter $v_{\max}$. According to the previous discussion $v_{\max} > 10^{-6}$ M s^{-1}.

Figure 2.4 shows that an increasing value of $v_{\max}$ involves a higher position of mode-one killing but also a higher intensity of DNA oxidation. Indeed $v_{\max}$is linked to the cell potential to reduce Fe^{3+} to Fe^{2+} and therefore to drive Fenton reaction more efficiently.

The simulations are consistent with the mode-one killing experimental position near 1-3 mM.

When Fe^{2+} recycling rate is too high (inset fig. 2.4) mode-one killing disappear because Fe^{2+} concentration remains constant.

Moreover, Imlay et al. [13] showed that if the availability of cellular reducing equivalents is increased as the result of respiration inhibition (through cyanide and NADH

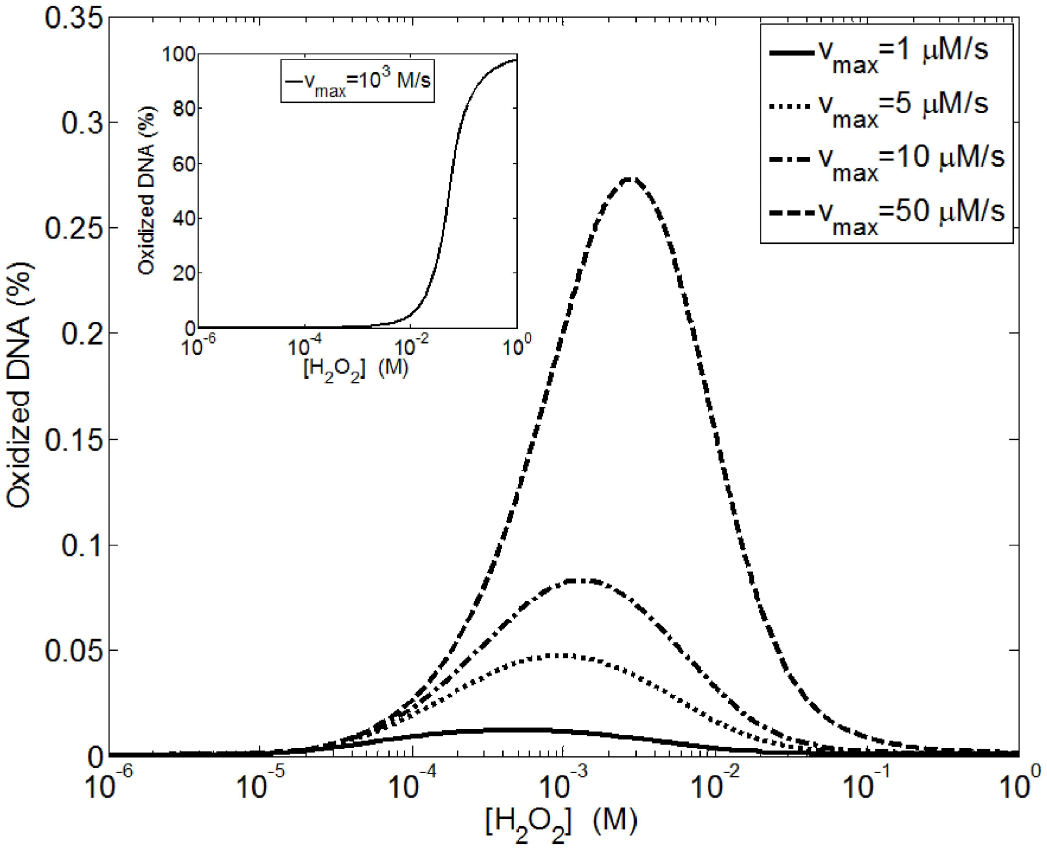

FIGURE 2.4: Average DNA oxidation (during 15 minutes) dependence upon H_2O_2 external concentration and maximal Fe^{2+} recycling rate $v_{\max}$. C_0 is set to 1 mM. Initially, cell density was set to 10^7 cell/mL. The kinetic parameters used for the simulation are gathered in table 2.2.

dehydrogenase mutations), mode I killing was enhanced. Our model is able to reproduce this phenomenology, as demonstrated by the direct correlation between the $v_{\max}$ parameter and the percentage of oxidized DNA (Figure 2.4).

The influence of C_0

As C_0 is increasing, mode-one killing is shifting into high position and high intensity according to figure 2.5. In order to fit with Imlay's experimental results C_0 has to stay in a range between 0.1 and 1 mM.

The influence of free available iron $[Fe]$

TABLE 2.2: Summary of the different constants used for *in silico* simulations. (*) this value is limited the *in vivo* diffusion-limited rate constant assumed to be 2×10^9 M s^{-1}. (**) We also tested value from 10 to 40 μM for the simulation showed in figure 2.6.

Constants	Value	Reference
$k_{prod}^{H_2O_2}$	15 μM s^{-1}	[8, 38]
K_M^{Kat}	5.9 $\times 10^{-3}$ M	[9]
K_M^{Ahp}	1.2 $\times 10^{-6}$ M	[12]
$k_{cat}^{Kat}\,[Kat]$	4.9 $\times$ 10^{-1} M s^{-1}	
$k_{cat}^{Ahp}\,[Ahp]$	6.6 $\times 10^{-4}$ M s^{-1}	
k_{diff}	70 s^{-1}	
$V_{internal}$	3.2 $\times$ 10^{-15} L	[11]
k_{DNA}	4.7 $\times$ 10^9 M s^{-1} (*)	[20]
k_F	4400 M s^{-1}	[5]
Initial Fe^{2+} concentration	By default 20 μM (**)	
Initial cell density *n*	From 10^6 to 10^9	
C_0	Tested from 0.1 to 5 mM	This work
$v_{\max}$	Tested from 1 to 50 μM s^{-1} and 3 M s^{-1}	This work
Simulation time	15 minutes	[14, 39]

Iron chelators such as dipyridyl that can penetrate bacteria prevent external H_2O_2 from damaging DNA by reducing free available iron thanks to chelation [13]. Overexpression of ferritin, a storage protein that specifically sequesters iron also prevents damage [40]. But *E. coli* mutants that over-import iron are more sensitive to DNA damage when challenging external H_2O_2 [41]. Figure 2.6 reports the same conclusion with increasing damage when free available iron concentration increases.

2.3.3 Cell density involvement.

Under conditions of exogenous H_2O_2 stress, H_2O_2 elimination is dependent on cell density. However, nothing is currently known about internal H_2O_2 concentration during H_2O_2 exposure. Under these conditions, internal H_2O_2 concentration results mostly from influx due to diffusion across the cell membrane, because endogenous production is negligible. Moreover, the more cell density increases, the faster the medium is detoxified. This phenomenon involves a decrease in exogenous H_2O_2 concentration and

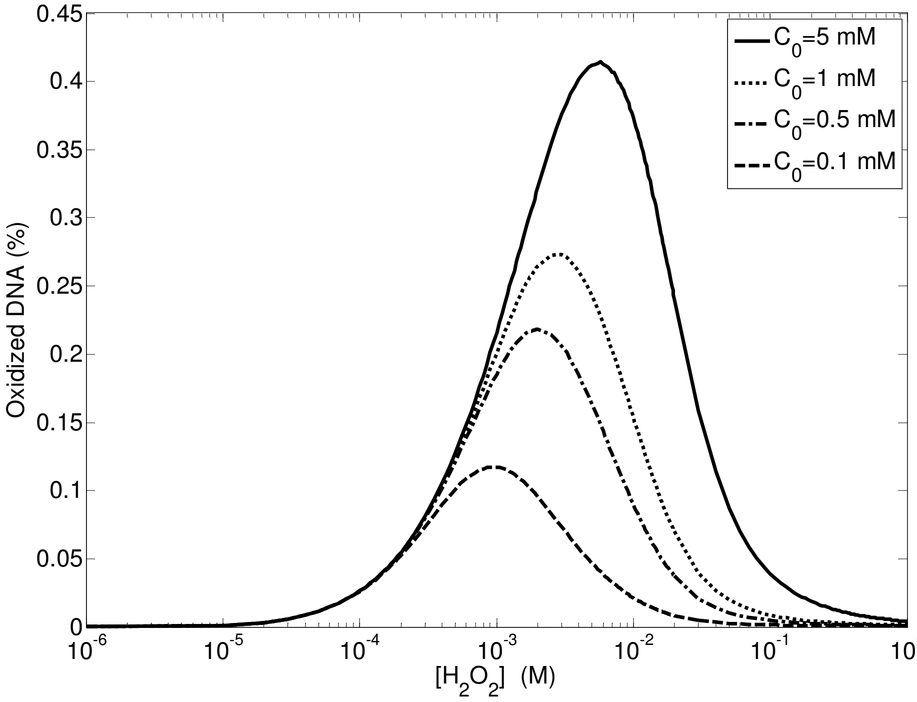

FIGURE 2.5: Average DNA oxidation (during 15 minutes) dependence upon H_2O_2 external concentration and parameter C_0. $v_{\max}$ is set to 50 μM s^{-1}. Initially, cell density was set to 10^7 cell/mL. The kinetic parameters used for the simulation are gathered in table 2.2.

consequently in internal H_2O_2 concentration. Figure 2.7 reports *in vivo* experimental detoxification of the medium with two different concentrations (A) and it also shows the corresponding *in silico* simulation which correctly fits the experiment (B).

As reported in figure 2.8, simulation shows that depending on cell density external average H_2O_2 concentration can be two orders of magnitude lower as the initial H_2O_2 exogenous concentration. This difference is involved in the disappearance of the mode one killing at high cell density as observed in figure 2.9.

The major characteristics (intensity, width, position) of mode one killing is strongly dependent on cell density. Whereas the mode one killing seems to be present under 3×10^7 cell/ml, it disappears over 10^8 cell/ml. This phenomenon has been observed

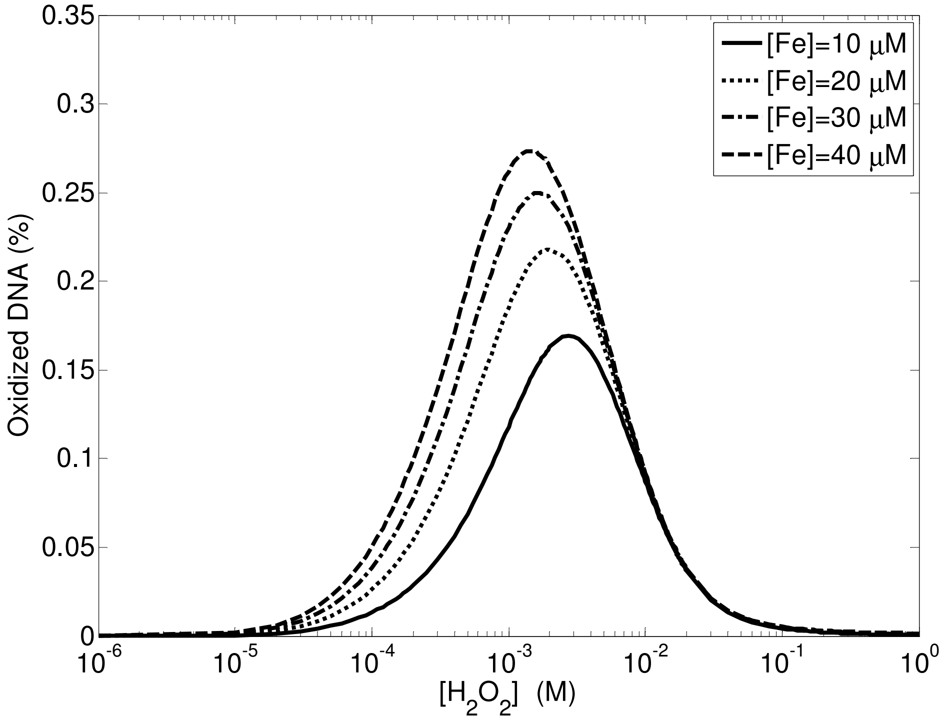

FIGURE 2.6: DNA oxidation (average during 15 minutes) dependence upon H_2O_2 external concentration and free available iron concentration. Parameter C_0 is set to 0.5 mM and $v_{\max}$ is set to 50 μM s^{-1}. Initially cell density was set to 10^7 cell/mL. The kinetic parameters used for the simulation are gathered in table 2.2.

experimentally by our team (unpublished data). Indeed even at 10^8 cell/ml the mode one killing may disappear because it may be combined with mode two killing which emerges after 10 mM. This phenomenon is particularly non linear (see inset of figure 2.9) whereas external average H_2O_2 concentration follows a nearly linear evolution compared with initial H_2O_2 exogenous or compared with cell density.

2.4 Conclusions

We present here a simple model that allows the understanding of DNA oxidation dynamics within *E. coli* after H_2O_2 exposure. The objective of the model presented is to essentially describe in a dynamic way the nature of H_2O_2 toxicity to an organism, in this case *E. coli*. Even if this model could seem imperfect, we believe that the scientific community will be able to challenge and improve it. For instance, using this approach,

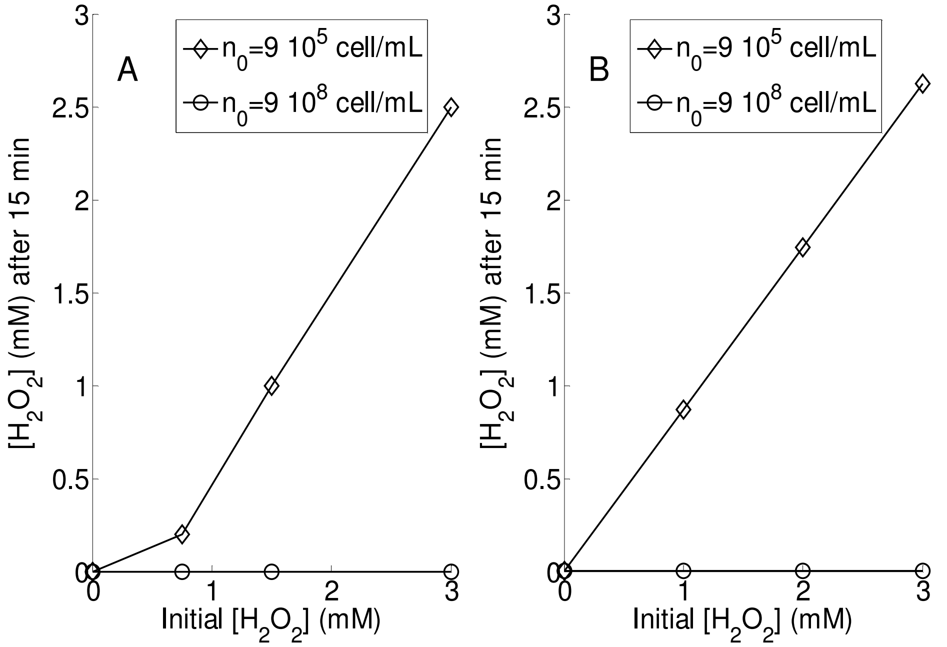

FIGURE 2.7: *E. coli* (MG1655) (*in vivo* A) cells were grown aerobically in liquid LB broth, at 37°C, with shaking at 160 rpm. When the OD_{600} reached 1, the cells (diluted till 9 10^5/ml or not diluted) were exposed to various concentrations of H_2O_2 for 15 minutes. Extracellular H_2O_2 concentration was determined by TECAN readings at OD_{560}, with the Amplex® red hydrogen peroxide/peroxidase kit. Extracellular H_2O_2 concentration, determined after 15 minutes of incubation with various amounts of exogenous H_2O_2, in a wild-type strain incubated in LB, at 37°C, in the presence of 400 ppm CO_2. (This experiment was carried out by A. Gerstel) Exogenous H_2O_2 concentration simulated under the same experimental conditions (*in silico* B).

we were able to demonstrate iron or cell density involvement in $HO^\bullet$ dynamic and by consequence in DNA oxidation within *E. coli*. Indeed, without taking into account the evolution of those two parameters, we were not able to reproduce mode one killing experimental results obtained in the literature. Moreover the first killing mode can only be explained with iron decrease and not with quenching reactions which are responsible for slowing down oxidation but not for the oxidation peak.

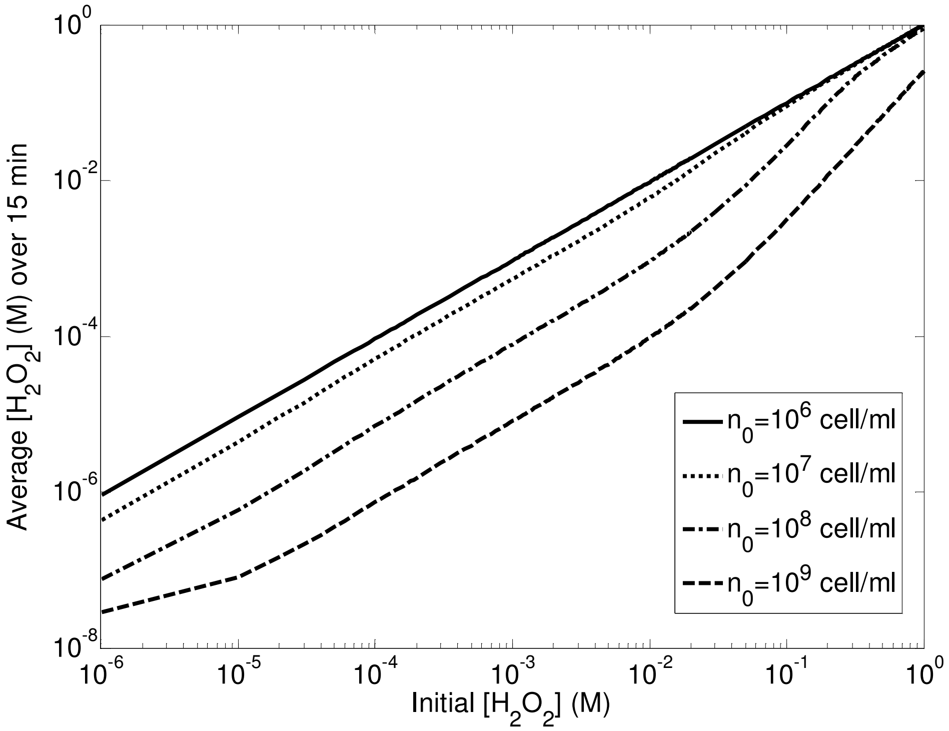

FIGURE 2.8: Simulation of the average H_2O_2 external concentration dependence with cell density and initial H_2O_2 exogenous concentration. The kinetic parameters used for the simulation are gathered in table 2.2.

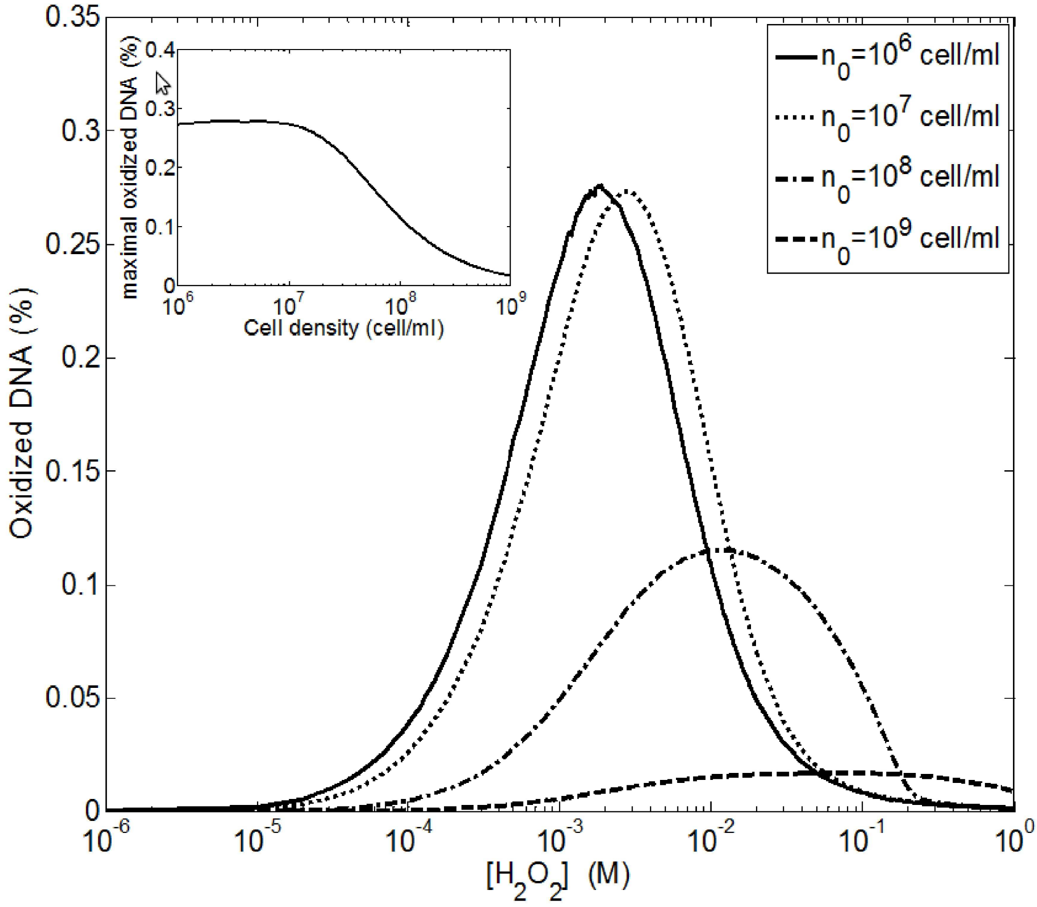

FIGURE 2.9: Simulation of the average oxidized DNA proportion dependence with cell density and initial H_2O_2 exogenous concentration. Inset shows the maximal oxidized DNA proportion dependence with cell density. The kinetic parameters used for the simulation are gathered in table 2.2.

Bibliography

[1] J. A. Imlay, "The molecular mechanisms and physiological consequences of oxidative stress: Lessons from a model bacterium", Nature Reviews Microbiology, vol. 11, no. 7, pp. 443–454, 2013.

[2] M. Jimenez-Del-Rio and C. Velez-Pardo, "The bad, the good, and the ugly about oxidative stress", Oxidative medicine and cellular longevity, vol. 2012, 2012.

[3] I. Fridovich, "The biology of oxygen radicals", Science, vol. 201, no. 4359, pp. 875–880, 1978.

[4] K. Keyer and J. A. Imlay, "Superoxide accelerates dna damage by elevating free-iron levels", Proceedings of the National Academy of Sciences, vol. 93, no. 24, pp. 13 635–13 640, 1996.

[5] S. Park, X. You, and J. A. Imlay, "Substantial dna damage from submicromolar intracellular hydrogen peroxide detected in hpx-mutants of escherichia coli", Proceedings of the National Academy of Sciences of the United States of America, vol. 102, no. 26, pp. 9317–9322, 2005.

[6] A. Kowald, H. Lehrach, and E. Klipp, "Alternative pathways as mechanism for the negative effects associated with overexpression of superoxide dismutase", Journal of Theoretical Biology, vol. 238, no. 4, pp. 828–840, 2006.

[7] B. González-Flecha and B. Demple, "Metabolic sources of hydrogen peroxide in aerobically growing escherichia coli", Journal of Biological Chemistry, vol. 270, no. 23, pp. 13 681–13 687, 1995.

[8] L. C. Seaver and J. A. Imlay, "Are respiratory enzymes the primary sources of intracellular hydrogen peroxide?", Journal of Biological Chemistry, vol. 279, no. 47, pp. 48 742–48 750, 2004.

[9] A. Hillar, B. Peters, R. Pauls, A. Loboda, H. Zhang, A. G. Mauk, and P. C. Loewen, "Modulation of the activities of catalase-peroxidase hpi of escherichia coli by site-directed mutagenesis", Biochemistry, vol. 39, no. 19, pp. 5868–5875, 2000.

[10] F. Åslund, M. Zheng, J. Beckwith, and G. Storz, "Regulation of the oxyr transcription factor by hydrogen peroxide and the cellular thiol—disulfide status", Proceedings of the National Academy of Sciences, vol. 96, no. 11, pp. 6161–6165, 1999.

[11] J. Imlay and I. Fridovich, "Assay of metabolic superoxide production in escherichia coli.", Journal of Biological Chemistry, vol. 266, no. 11, pp. 6957–6965, 1991.

[12] L. C. Seaver and J. A. Imlay, "Alkyl hydroperoxide reductase is the primary scavenger of endogenous hydrogen peroxide in escherichia coli", Journal of bacteriology, vol. 183, no. 24, pp. 7173–7181, 2001.

[13] J. A. Imlay, S. M. Chin, and S. Linn, "Toxic dna damage by hydrogen peroxide through the fenton reaction in vivo and in vitro", Science, vol. 240, no. 4852, p. 640, 1988.

[14] J. A. Imlay and S. Linn, "Bimodal pattern of killing of dna-repair-defective or anoxically grown escherichia coli by hydrogen peroxide.", Journal of bacteriology, vol. 166, no. 2, pp. 519–527, 1986.

[15] F. Antunes, A. Salvador, H. S. Marinho, R. Alves, and R. E. Pinto, "Lipid peroxidation in mitochondrial inner membranes. i. an integrative kinetic model", Free Radical Biology and Medicine, vol. 21, no. 7, pp. 917–943, 1996.

[16] R. L. Bertrand, "Lag phase-associated iron accumulation is likely a microbial counter-strategy to host iron sequestration: Role of the ferric uptake regulator (fur)", Journal of theoretical biology, vol. 359, pp. 72–79, 2014.

[17] L. Macomber, C. Rensing, and J. A. Imlay, "Intracellular copper does not catalyze the formation of oxidative dna damage in escherichia coli", Journal of bacteriology, vol. 189, no. 5, pp. 1616–1626, 2007.

[18] Y. Luo, Z. Han, S. M. Chin, and S. Linn, “Three chemically distinct types of oxidants formed by iron-mediated fenton reactions in the presence of dna”, Proceedings of the National Academy of Sciences, vol. 91, no. 26, pp. 12 438–12 442, 1994.

[19] G. V. Buxton, C. L. Greenstock, W. P. Helman, and A. B. Ross, “Critical review of rate constants for reactions of hydrated electrons, hydrogen atoms and hydroxyl radicals oh/o in aqueous solution”, Journal of physical and chemical reference data, vol. 17, no. 2, pp. 513–886, 1988.

[20] H. B. Michaels and J. Hunt, “Reactions of the hydroxyl radical with polynucleotides”, Radiation Research, vol. 56, no. 1, pp. 57–70, 1973.

[21] W. H. Koppenol, “The haber-weiss cycle–70 years later”, Redox Report, vol. 6, no. 4, pp. 229–234, 2001.

[22] S. I. Liochev and I. Fridovich, “The haber-weiss cycle—70 years later: An alternative view”, Redox report, vol. 7, no. 1, pp. 55–57, 2002.

[23] M. Valko, H. Morris, and M. Cronin, “Metals, toxicity and oxidative stress”, Current medicinal chemistry, vol. 12, no. 10, pp. 1161–1208, 2005.

[24] J. A. Imlay, “Pathways of oxidative damage”, Annual Reviews in Microbiology, vol. 57, no. 1, pp. 395–418, 2003.

[25] J. L. Brumaghim, Y. Li, E. Henle, and S. Linn, “Effects of hydrogen peroxide upon nicotinamide nucleotide metabolism in escherichia coli changes in enzyme levels and nicotinamide nucleotide pools and studies of the oxidation of nad (p) h by fe (iii)”, Journal of Biological Chemistry, vol. 278, no. 43, pp. 42 495–42 504, 2003.

[26] A. Polynikis, S. Hogan, and M. di Bernardo, “Comparing different ode modelling approaches for gene regulatory networks”, Journal of theoretical biology, vol. 261, no. 4, pp. 511–530, 2009.

[27] Y.-H. P. Hsieh and Y. P. Hsieh, "Kinetics of fe (iii) reduction by ascorbic acid in aqueous solutions", Journal of agricultural and food chemistry, vol. 48, no. 5, pp. 1569–1573, 2000.

[28] M. Giannessi, A. Delcorso, M. Cappiello, M. Voltarelli, I. Marini, D. Barsacchi, D. Garland, M. Camici, and U. Mura, "Thiol-dependent metal-catalyzed oxidation of bovine lens aldose reductase i. studies on the modification process", Archives of biochemistry and biophysics, vol. 300, no. 1, pp. 423–429, 1993.

[29] L. E. Netto and E. R. Stadtman, "The iron-catalyzed oxidation of dithiothreitol is a biphasic process: Hydrogen peroxide is involved in the initiation of a free radical chain of reactions", Archives of biochemistry and biophysics, vol. 333, no. 1, pp. 233–242, 1996.

[30] P. F. Hallin and D. W. Ussery, "Cbs genome atlas database: A dynamic storage for bioinformatic results and sequence data", Bioinformatics, vol. 20, no. 18, pp. 3682–3686, 2004.

[31] B. D. Bennett, E. H. Kimball, M. Gao, R. Osterhout, S. J. Van Dien, and J. D. Rabinowitz, "Absolute metabolite concentrations and implied enzyme active site occupancy in escherichia coli", Nature chemical biology, vol. 5, no. 8, pp. 593–599, 2009.

[32] M. v. Smoluchowski, "Attempt for a mathematical theory of kinetic coagulation of colloid solutions", Z. Phys. Chem., vol. 92, p. 129, 1917.

[33] K. Luby-Phelps, S. Mujumdar, R. Mujumdar, L. Ernst, W. Galbraith, and A. Waggoner, "A novel fluorescence ratiometric method confirms the low solvent viscosity of the cytoplasm.", Biophysical journal, vol. 65, no. 1, p. 236, 1993.

[34] M. K. Kuimova, G. Yahioglu, J. A. Levitt, and K. Suhling, "Molecular rotor measures viscosity of live cells via fluorescence lifetime imaging", Journal of the American Chemical Society, vol. 130, no. 21, pp. 6672–6673, 2008.

[35] Z. Petrášek and P. Schwille, "Precise measurement of diffusion coefficients using scanning fluorescence correlation spectroscopy", Biophysical journal, vol. 94, no. 4, pp. 1437–1448, 2008.

[36] M. Kushmerick and R. Podolsky, "Ionic mobility in muscle cells", Science, vol. 166, no. 3910, pp. 1297–1298, 1969.

[37] A. M. Mastro, M. A. Babich, W. D. Taylor, and A. D. Keith, "Diffusion of a small molecule in the cytoplasm of mammalian cells", Proceedings of the National Academy of Sciences, vol. 81, no. 11, pp. 3414–3418, 1984.

[38] L. C. Seaver and J. A. Imlay, "Hydrogen peroxide fluxes and compartmentalization inside growing escherichia coli", Journal of bacteriology, vol. 183, no. 24, pp. 7182–7189, 2001.

[39] J. A. Imlay and S. Linn, "Dna damage and oxygen radical toxicity.", Science(Washington), vol. 240, no. 4857, pp. 1302–1309, 1988.

[40] K. Keyer, A. S. Gort, and J. A. Imlay, "Superoxide and the production of oxidative dna damage.", Journal of bacteriology, vol. 177, no. 23, pp. 6782–6790, 1995.

[41] D. Touati, M. Jacques, B. Tardat, L. Bouchard, and S. Despied, "Lethal oxidative damage and mutagenesis are generated by iron in delta fur mutants of escherichia coli: Protective role of superoxide dismutase.", Journal of bacteriology, vol. 177, no. 9, pp. 2305–2314, 1995.

Chapter 3

The major defences relative roles and consequences in *E. coli*

PLOS | ONE

RESEARCH ARTICLE

Hydrogen Peroxide Induced Cell Death: The Major Defences Relative Roles and Consequences in *E. coli*

Lionel Uhl, Sam Dukan¤*

Institut de Microbiologie de la Méditerranée – Université Aix-Marseille, Laboratoire de Chimie Bactérienne, CNRS UMR7283, 31 Chemin Joseph Aiguier, 13009 Marseille, France

¤ Current address: Click4Tag SAS, Grand Luminy Technopole, Zone Luminy Entreprise Biotech Case 922, 163 Avenue de Luminy 13288 Marseille Cedex 09 France
* sdukan@imm.cnrs.fr; sam.dukan@click4tag.com

Abstract

We recently developed a mathematical model for predicting reactive oxygen species (ROS) concentration and macromolecules oxidation *in vivo*. We constructed such a model using *Escherichia coli* as a model organism and a set of ordinary differential equations. In order to evaluate the major defences relative roles against hydrogen peroxide (H_2O_2), we investigated the relative contributions of the various reactions to the dynamic system and searched for approximate analytical solutions for the explicit expression of changes in H_2O_2 internal or external concentrations. Although the key actors in cell defence are enzymes and membrane, a detailed analysis shows that their involvement depends on the H_2O_2 concentration level. Actually, the impact of the membrane upon the H_2O_2 stress felt by the cell is greater when micromolar H_2O_2 is present (9-fold less H_2O_2 in the cell than out of the cell) than when millimolar H_2O_2 is present (about 2-fold less H_2O_2 in the cell than out of the cell). The ratio between maximal external H_2O_2 and internal H_2O_2 concentration also changes, reducing from 8 to 2 while external H_2O_2 concentration increases from micromolar to millimolar. This non-linear behaviour mainly occurs because of the switch in the predominant scavenger from Ahp (Alkyl Hydroperoxide Reductase) to Cat (catalase). The phenomenon changes the internal H_2O_2 maximal concentration, which surprisingly does not depend on cell density. The external H_2O_2 half-life and the cumulative internal H_2O_2 exposure do depend upon cell density. Based on these analyses and in order to introduce a concept of dose response relationship for H_2O_2-induced cell death, we developed the concepts of "maximal internal H_2O_2 concentration" and "cumulative internal H_2O_2 concentration" (e.g. the total amount of H_2O_2). We predict that cumulative internal H_2O_2 concentration is responsible for the H_2O_2-mediated death of bacterial cells.

CrossMark
click for updates

OPEN ACCESS

Citation: Uhl L, Dukan S (2016) Hydrogen Peroxide Induced Cell Death: The Major Defences Relative Roles and Consequences in *E. coli*. PLoS ONE 11(8): e0159706. doi:10.1371/journal.pone.0159706

Editor: John Travers Hancock, University of the West of England, UNITED KINGDOM

Received: February 27, 2016

Accepted: July 7, 2016

Published: August 5, 2016

Copyright: © 2016 Uhl, Dukan. This is an open access article distributed under the terms of the Creative Commons Attribution License, which permits unrestricted use, distribution, and reproduction in any medium, provided the original author and source are credited.

Data Availability Statement: All relevant data are within the paper and its Supporting Information files.

Funding: This work was supported by ANR (Agence National de la Recherchegrant) (ANR-12-BS07-0022 ROSAS). The funders had no role in study design, data collection and analysis, decision to publish, or preparation of the manuscript.

Competing Interests: The authors have declared that no competing interests exist.

The previous chapter developed a mathematical model for predicting reactive oxygen species (ROS) concentration and macromolecules oxidation *in vivo*. We constructed such a model using *Escherichia coli* as a model organism and a set of ordinary differential equations. In order to evaluate the major defences relative roles against hydrogen peroxide (H_2O_2), we investigated the relative contributions of the various reactions to the dynamic system and searched for approximate analytical solutions for the explicit expression of changes in H_2O_2 internal or external concentrations.

3.1 Introduction

Oxygen is indisputably essential for life, but it can also impair cell ability to function normally or it can participate in its destruction ([1] and [2]) because of the generation of reactive oxygen species (ROS) like hydrogen peroxide (H_2O_2), superoxide ($O_2^{\bullet -}$) or hydroxyl radical ($HO^{\bullet}$).

In order to better understand ROS dynamic within cells, we recently developed a mathematical model ([3]) for predicting reactive oxygen species (ROS) concentration and macromolecules oxidation $in\,vivo$. This first study principally focuses on $HO^{\bullet}$ dynamic and its consequence on DNA whereas the current study will mainly focus on H_2O_2 dynamic.

Escherichia coli was used as a model organism. In order to build our mathematical model we used data from a large number of articles dealing with enzymes or molecule concentrations (in *E. coli*, kinetic properties and chemical reaction rate constants). We were then able to propose a mathematical model based on a set of ordinary differential equations relating to fundamental principles of mass balance and reaction kinetics. It offers the possibility to simulate properly the experimental results obtained by biologists and therefore to understand the biological parameters involved in the observed phenomena.

The purpose of this study is to use our mathematical model in order to better understand H_2O_2 mode of action on *E. coli* as a model organism.

In aerobic organisms, oxygen oxidizes redox enzymes, generating a flux of H_2O_2 that can potentially damage the cell. For instance, *Escherichia coli* generates about 14 μM H_2O_2 per second when it grows aerobically on glucose ([4]). In order to cope with H_2O_2 stress, microbes typically contain multiple catalases and/or peroxidases. *E. coli* contains one Alkyl hydroperoxide reductase (Ahp) and two different catalases (Cat). Alkyl hydroperoxide reductase is the primary scavenger for endogenous H_2O_2 in *E. coli* ([5]). Catalase contributes little when H_2O_2 levels are low, but it becomes the most effective scavenger when H_2O_2 levels are high ([5]). Moreover, membrane permeability is part of the global defence process against H_2O_2 ([4]). However, to our knowledge, the question of their relative involvement remains unsolved especially with regard to the exogenous H_2O_2 concentration.

Mechanisms involved in H_2O_2 induced cell death were studied by Imlay and Linn ([6] and [7]) who showed that the exposure of *E. coli* to H_2O_2 led to two different modes of killing. The first was observed at low H_2O_2 concentration (1-3 mM H_2O_2) and resulted from the DNA damage caused by $HO^\bullet$ ([7]). The second resulted from damage to unknown macromolecules, inflicted more directly, through H_2O_2-mediated oxidation. However, and to our knowledge, the question of the relative involvement of the cumulative or the maximal H_2O_2 dose involvement in this phenomenon remains unsolved. Dose response is a question often raised about radiative hazards. For instance Harrison *et al.* ([8]) indicated median survival times in rats following intravenous injection of polonium-210. The total alpha-particles-emitted numbers show that the cumulative dose and not the maximal dose is principally responsible for death.

Using our mathematical model, we first investigated the relative role of the different ways (principally Ahp, Cat and membrane) for cells to decrease and fight H_2O_2 oxidative stress. Here we predict that their involvement depends on the H_2O_2 stress level. Moreover and as observed for radiative hazards, we predict that cumulative internal H_2O_2 concentration is responsible for the H_2O_2-mediated death of bacterial cells.

3.2 Materials and Methods

The model assumes that all molecule concentrations are homogeneous in cells. We therefore describe the problem with a dynamic system of ordinary differential equations (ODE) instead of using a complex algorithm such as the Next-Sub-Volume Method. Indeed, one algorithm generally used to study the compartmentalization of molecules in microorganisms (for instance *E. coli*) is the Next-Sub-volume Method. It is a Gillespie-like ([9] and [10]) method approaching the spatial effects of diffusive phenomena and chemical reaction. According to the Next Sub-volume Method, the side length ℓ of the square sub-volumes has to satisfy the two inequalities

$$R \ll \ell \text{ and } \tau_{diff} = \frac{\ell^2}{6D} \ll \tau_{react}$$

where R is the larger radius of a molecule of substrat

and D the diffusion constant of H_2O_2

τ_{diff} represents the characteristic time of diffusion

τ_{react} represents the characteristic time of reaction

The first inequality indicates that dissociation events can be properly defined within sub-volumes. The second criterion specifies that the time for any molecule to leave a sub-volume is much smaller than the shortest reaction time τ_{min} among the molecular species, so that all molecules are homogeneously distributed within the sub-volumes. For example, the 3D simulations are typically performed with ℓ =0,1 μm and the depth $h = \ell$ of the sub-volumes, which is many times larger than the average radius of a substrat even protein. Considering the H_2O_2 molecule maximal number, the reaction initially follows a pseudo-first order kinetic with rate constant $k' = k\,[H_2O_2]$ and the characteristic time of reaction is therefore $\tau = 1/k'$. This time has to be compared to the characteristic time of diffusion of H_2O_2 : $\tau_{diff} = \frac{\ell^2}{6D}$ ≈10^{-6} s (with H_2O_2 diffusion constant D = 2 10^{-9} $\text{m}^2.\text{s}^{-1}$). This comparison gives $\tau = 1/k' = 1/k\,[H_2O_2] \gg 10^{-6}$ or $[H_2O_2] \ll 10^6/k$. Even with very high rate constant such as 10^6 $\text{M}^{-1}\text{s}^{-1}$, the inequality imposes $[H_2O_2] \ll 1\,\text{M}$. In conclusion, while $[H_2O_2] \ll 1\,\text{M}$, the diffusion within the cell is faster than the reaction rate and we do not need to consider compartmentalization.

$O_2^{\bullet -}$ and H_2O_2 are involved in many reactions. Of course we do not take all possible reactions into account, for instance, we do not consider the Haber-Weiss reaction, because our simulations showed no change with or without its consideration and moreover because the relevance of this reaction *in vivo* is questionable ([11] and [12]); actually adding the Haber-Weiss reaction, numerical simulations show that it is negligible whether H_2O_2 concentration is under 0.1 mol·L^{-1}. Using published rate constants, we propose here some simplifications and approximations of the system achieved by neglecting the kinetically non-significant reaction. $HO^{\bullet}$ was studied in a previous article ([3]).

3.2.1 Superoxide kinetics

Superoxide is involved in the following kinetically significant reactions:
Its production :

$$metabolism\ production \xrightarrow{k_1} O_2^{\bullet -}$$

Its tree ways of dismutation (by SOD, by GSH and spontaneously)

$$O_2^{\bullet -} + H^+ \xrightarrow[SOD]{k_2} \frac{1}{2} H_2O_2 + \frac{1}{2} O_2$$

$$O_2^{\bullet -} + GSH + H^+ \xrightarrow{k_{GSH}} \frac{1}{2} GSSG + H_2O_2$$

$$2O_2^{\bullet -} + 2H^+ \xrightarrow{k_{sp}} H_2O_2 + O_2$$

Those reactions lead to the following ordinary differential equation (ODE) coming from the balance between production and consumption:

$$\begin{aligned} \frac{\mathrm{d}\left[O_2^{\bullet -}\right]}{\mathrm{d}t} &= k_1 \\ &\quad -k_2 \left[SOD\right]\left[O_2^{\bullet -}\right] - k_{GSH}\left[GSH\right]\left[O_2^{\bullet -}\right] - 2k_{sp}\left[O_2^{\bullet -}\right]^2 \end{aligned}$$

3.2.2 Internal hydrogen peroxide kinetics

H_2O_2 appears significantly in the following reactions : Its productions :

$$metabolism\,production \xrightarrow{k_1'} H_2O_2$$

$$O_2^{\bullet -} + H^+ \xrightarrow[SOD]{k_2} \frac{1}{2}H_2O_2 + \frac{1}{2}O_2$$

Its dismutation by catalase (Cat) or Alkylhydroperoxidase (Ahp)

$$H_2O_2 \xrightarrow{Cat} H_2O + \frac{1}{2}O_2$$

$$H_2O_2 \xrightarrow{Ahp} H_2O + \frac{1}{2}O_2$$

Its diffusion across cell membrane

$$H_2O_2 \xrightarrow{k_{diff}} H_2O_{2out}$$

k_{diff} has been calculated using the membrane permeability coefficient ($P = 1.6 \times 10^{-3}$ cm/s), the membrane surface area ($A = 1.41 \times 10^{-7}$ cm^2) and cell volume ($V = 3.2 \times 10^{-15}$ L) given by Seaver and Imlay ([4]), therefore $k_{diff} = \frac{P \times S}{V}$.

The ODE becomes :

$$\begin{aligned}
\frac{\mathrm{d}\,[H_2O_2]}{\mathrm{d}t} = \; & k_1' \\
& + \frac{1}{2}k_2\,[SOD]\left[O_2^{\bullet -}\right] \\
& - \frac{k_{cat}^{Ahp}\,[Ahp]\,[H_2O_2]}{[H_2O_2] + K_M^{Ahp}} - \frac{k_{cat}^{Kat}\,[Cat]\,[H_2O_2]}{[H_2O_2] + K_M^{Kat}} \\
& - k_{diff}\left([H_2O_2] - [H_2O_2]_{out}\right)
\end{aligned}$$

where H_2O_{2out} corresponds to H_2O_2 in the external habitat of the cell.

K_M (K_M^{Kat} for catalase and K_M^{Ahp} for alkylhydroperoxidase) is the Michaelis constant. k_{cat} (k_{cat}^{Kat} for catalase and k_{cat}^{Ahp} for alkylhydroperoxidase) is the turnover number, it represents the maximum number of molecules (here H_2O_2) that an enzyme is able to convert into products per second.

3.2.3 External hydrogen peroxide

$$\frac{\mathrm{d}\,[H_2O_2]_{out}}{\mathrm{d}t} = k_{diff}\frac{n \cdot V_{in}}{V_{out} - nV_{in}}\left([H_2O_2] - [H_2O_2]_{out}\right)$$

The cell density is given by n. V_{in} represents the cell internal volume and V_{out} corresponds to the total volume. Of course, as microorganisms cannot take up more space than their medium, we have the inequality $V_{out} - nV_{in} \gg 0$.

3.2.4 Cell density

For under 10 minutes experimental time (consistent with most of our simulation), cell density could be considered as a constant but for long time simulation we propose the logistic equation for cell growing function. The logistic equation (also called the Verhulst model) is a model of population growth first published by Pierre Verhulst ([13] and [14]). The continuous version of the Verhulst model is described by the following differential equation:

$$\frac{\mathrm{d}n}{\mathrm{d}t} = r \cdot n\left(1 - \frac{n}{n_{max}}\right)$$

where r is the Malthusian parameter (rate of population growth) and n_{max} the maximum sustainable population. This differential equation gives an analytical solution:

$$n(t) = \frac{n_0 e^{rt}}{1 + \frac{n_0}{n_{max}}\left(e^{rt} - 1\right)}$$

where n_0 is the initial density. This value depends on the experiment. We choose carrying capacity $n_{max} = 5 \times 10^9$ cell/mL. The maximal rate of growth usually shows that a growing bacterial population doubles at regular intervals near a characteristic time $\tau_d \approx 20$ minutes. Therefore $n(t)$ expression also gives:

$$n(t) = \frac{n_0 2^{t/\tau_d}}{1 + \frac{n_0}{n_{max}}\left(2^{t/\tau_d} - 1\right)}$$

where $r = \ln(2)/\tau_d$.

Nevertheless this characteristic time depends on cell history and stress. For example, even 0.2 mM of H_2O_2 when added to a logarithmically growing *E. coli* population is enough to generate an immediate decrease in the number of viable cells. This phenomenon is transient and the original number of viable cells is recovered only about 40 minutes after the occurrence of the sub-lethal stress ([15]). This transient phenomenon is mirrored at the population level by a lag phase in which optical density remains almost constant for about 40 minutes. A fraction dies, and then the remaining bacteria resume growth so that the number of viable cells reaches the original number. For instance Chang *et al.* ([16]) also report a lag phase of about 40 minutes after an addition of 1.5 mM of H_2O_2. In order to take into account this phenomenon we consider that $\tau_d \to \infty$ if $t < 40$ minutes so that $n(t < 40\,min) = constant$ after H_2O_2 oxidative stress.

We were not concerned with stationary phase because no experiment carried out in this work reached the maximum sustainable population.

3.2.5 Kinetic constants

The kinetic constants used in this work are gathered in Table 3.1 and 3.2 according to Imlay and Fridovich ([17]) and Seaver and Imlay ([5] and [4]).

TABLE 3.1: Kinetic constants used to describe H_2O_2 evolution.

Kinetic constants	
k_1	5.7×10^{-6} mol·L^{-1}·s^{-1}
$k_2[SOD]$	2.8×10^{4} s^{-1}
k_2	1.5×10^{9} mol^{-1}·L·s^{-1}
V_{in}	3.2×10^{-15} L
k_1'	12×10^{-6} mol·L^{-1}·s^{-1}
$k_{cat}^{Ahp}[Ahp]$	6.6×10^{-4} mol·L^{-1}·s^{-1}
K_M^{Ahp}	1.2×10^{-6} mol·L^{-1}
$k_{cat}^{Kat}[Cat]$	4.9×10^{-1} mol·L^{-1}·s^{-1}
K_M^{Kat}	5.9×10^{-3} mol·L^{-1}
k_{diff}	70 s^{-1}

TABLE 3.2: Kinetic constants used to describe $O_2^{\bullet -}$ evolution.

Constants	**Value**
k_1	5.7×10^{-6} mol·L^{-1}·s^{-1}
$k_2[SOD]$	2.8×10^{4} s^{-1}
k_2	1.5×10^{9} mol^{-1}·L·s^{-1}
$k_{GSH}[GSH]$	1.3×10^{1} s^{-1}
k_{GSH}	2.6×10^{3} mol^{-1}·L·s^{-1}
k_{sp}	5.0×10^{5} mol^{-1}·L·s^{-1}

3.2.6 Numerical simulations

All numerical simulations were carried out using the MATLAB ODE solver ode15s for stiff differential equations. The multistep solver ode15s is a variable order solver based on the numerical differentiation formulas.

3.3 Results and discussion

This section presents the analytical study of the dynamic system. This analysis will provide us with insight into the kinetic parameters significantly important for the dynamics of *ROS*. The first subsection introduces $O_2^{\bullet -}$ kinetics and evolution with different phenotypes of *E. coli*. The second subsection then develops H_2O_2 kinetics which lightly depends on $O_2^{\bullet -}$ kinetic.

3.3.1 Superoxide evolution

According to this dynamical system the following analysis is made without exogenous stress.

In the wild-type strain

In the wild-type strain, the resolution of $O_2^{\bullet -}$ concentration gives :

$$\left[O_2^{\bullet -}\right] \approx \left[O_2^{\bullet -}\right]_{\infty} \left(1 - e^{-k_2[SOD]t}\right)$$

indeed GSH and spontaneous dismutation are negligible because $k_{sp} \ll k_{GSH}\,[GSH] \ll k_2\,[SOD]\,the.$ $O_2^{\bullet -}$ concentration rapidly reached its steady-state value, in less than 1 ms, actually the characteristic time is given by $\frac{1}{k_2[SOD]}$. This time, which was dependent solely on *SOD* concentration and the *SOD* catalytic degradation rate k_2, corresponds to the characteristic time require for the re-establishment of equilibrium.

If we assume that *SOD* concentration and $O_2^{\bullet-}$ production change over time, and that their equilibrium time values are probably significantly shorter than 1 ms, then the steady-state value of $O_2^{\bullet-}$ concentration is always reached but depends purely on $O_2^{\bullet-}$ production rate and *SOD* catalytic degradation rate (k_2), which are time-dependent.

For each time, we can write that the $O_2^{\bullet-}$ concentration is $\left[O_2^{\bullet-}\right](t) = \frac{k_1(t)}{k_2[SOD](t)}$. For example, with published values [18], $O_2^{\bullet-}$ concentration is 2.1×10^{-10} M : this value fits the Imlay prediction well, and it corresponds to the equilibrium between $O_2^{\bullet-}$ production (parameter k_1) and the rate of scavenging of this radical by *SOD*.

We confirmed this approximation, by comparing the analytical solution (▲) with the numerical solution (■) in figure 3.1. Indeed this comparison help us to check whether the suggested approximations used to find an analytical expression are valid.

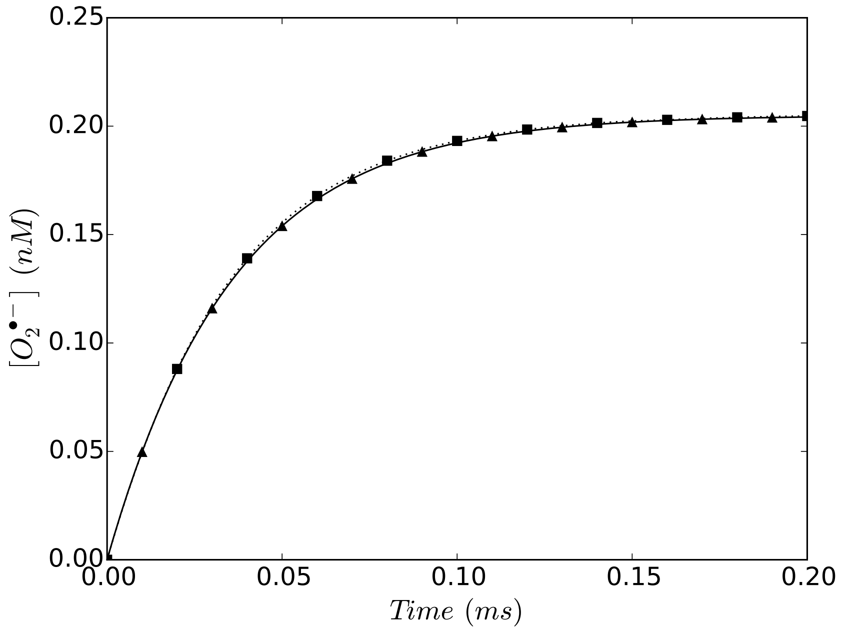

FIGURE 3.1: Change in $O_2^{\bullet-}$ concentration in the *E. coli* wild-type strain. (▲) corresponds to the analytical solution according to the simplified system and (■) corresponds to whole model solved with numerical methods. Cell density has no influence on the pattern of superoxide concentration evolution.

In a wild strain, the two major reaction involving superoxide are its production and its consumption by SOD.

In a SOD(-) mutant

In a *SOD* (-) mutant, changes in $O_2^{\bullet -}$ concentration were explained principally by the following differential equation :

$$\frac{\mathrm{d}\left[O_2^{\bullet -}\right]}{\mathrm{d}t} = k_1 - k_{GSH}\left[GSH\right]\left[O_2^{\bullet -}\right]$$

The resolution of $O_2^{\bullet -}$ concentration gave: $\left[O_2^{\bullet -}\right] \approx \left[O_2^{\bullet -}\right]_\infty \left(1 - e^{-k_{GSH}[GSH]t}\right)$, which rapidly reached its steady-state value, in less than 0.5 s. Actually the characteristic time is $\frac{1}{k_{GSH}[GSH]}$. This time, which was dependent only on *GSH* concentration and the *GSH* catalytic degradation rate k_{GSH}, corresponds to the characteristic time required for the re-establishment of equilibrium.

If we assume that *GSH* concentration and $O_2^{\bullet -}$ production can change over time, and that their equilibrium time values are probably significantly shorter than 0.5 s, then the steady state value of $O_2^{\bullet -}$ concentration is always reached but is dependent purely on $O_2^{\bullet -}$ production rate and the *GSH* catalytic degradation rate k_{GSH}, which are time-dependent.

For each time point, we can write that $O_2^{\bullet -}$ concentration is $\left[O_2^{\bullet -}\right](t) = \frac{k_1(t)}{k_{GSH}[GSH](t)}$. For example, with published values [18], $O_2^{\bullet -}$ concentration is 4.4×10^{-7} M. This value is consistent with the predictions of Imlay and corresponds to the equilibrium between $O_2^{\bullet -}$ production (parameter k_1) and the rate of scavenging of this radical by *GSH*.

For confirmation of this approximation, we compared (figure 3.2) the analytical solution (▲) with the numerical one (■):

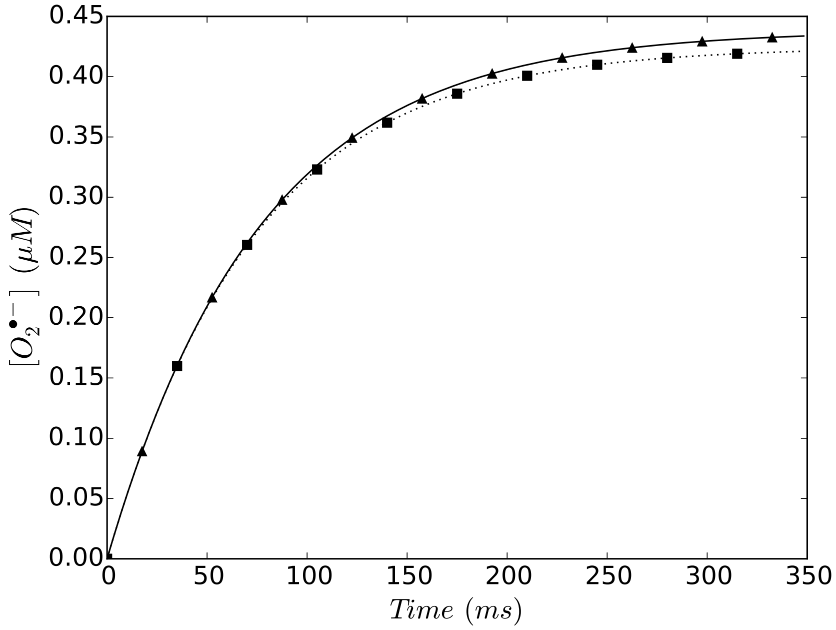

FIGURE 3.2: Changes in $O_2^{\bullet -}$ concentration in a $SOD(-)$ mutant. (▲) corresponds to the analytical solution according to the simplified system and (■) corresponds to the whole model solved with numerical methods. Cell concentration has no influence on this pattern of superoxide concentration evolution.

In a *SOD*(-) *GSH*(-) mutant

In a *SOD*(-) *GSH*(-) mutant, the change in $O_2^{\bullet -}$ concentration can be explained principally by the following differential equation according to the spontaneous dismutation:

$$\frac{\mathrm{d}\left[O_2^{\bullet -}\right]}{\mathrm{d}t} = k_1 - 2k_{sp}\left[O_2^{\bullet -}\right]^2$$

$O_2^{\bullet -}$ concentration obeys the function :

$$\left[O_2^{\bullet -}\right] = \left[O_2^{\bullet -}\right]_\infty \frac{1 - \mathrm{e}^{-\mathrm{t}/2\tau}}{1 + \mathrm{e}^{-\mathrm{t}/2\tau}}$$

where $\tau = \frac{1}{\sqrt{2k_1 k_{sp}}}$ and $\left[O_2^{\bullet -}\right]_\infty = \sqrt{\frac{k_1}{2k_{sp}}}$

$O_2^{\bullet -}$ concentration rapidly reaches its steady-state $\left[O_2^{\bullet -}\right]_\infty$ value, in less than 1 s (τ is the characteristic time). This time, which is dependent solely on the dismutation rate k_{sp}, corresponds to the characteristic time required to re-establish equilibrium.

If we assume that $O_2^{\bullet -}$ production can change over time, and that the equilibrium time is probably significantly shorter than 1 s, then the steady-state value of $O_2^{\bullet -}$ concentration is always reached but is dependent purely on $O_2^{\bullet -}$ production rate, which is time-dependent.

For each time point, we can write that $O_2^{\bullet -}$ concentration is $\left[O_2^{\bullet -}\right](t) \approx \sqrt{\frac{k_1(t)}{2k_{sp}}}$. With published values, the $O_2^{\bullet -}$ concentration is 2.4 × 10^{-6}M, a value consistent with the predictions of Imlay [18], and corresponding to the equilibrium between $O_2^{\bullet -}$ production (parameter k_1) and its spontaneous dismutation.

The analytical solution (▲) and the numerical solution (■) are the identical because they solved the same system (figure 3.3).

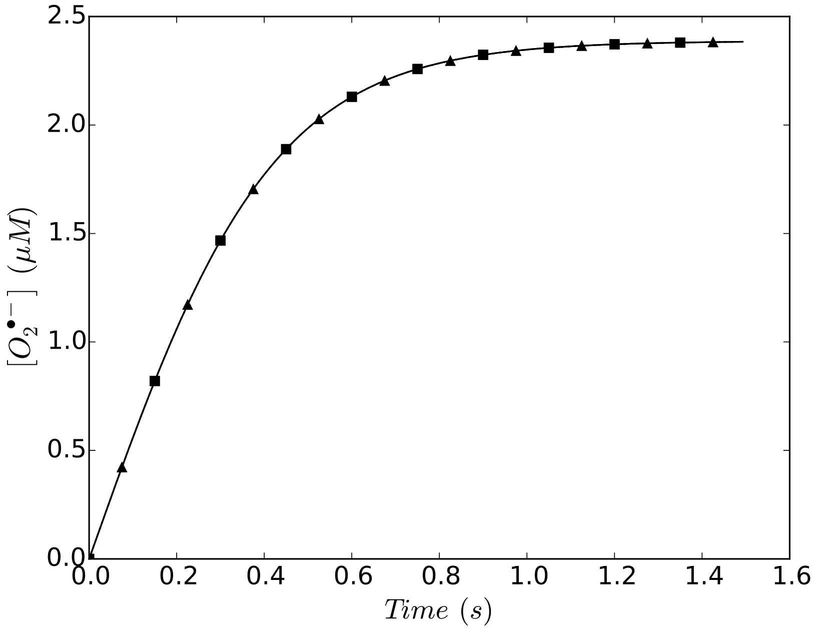

FIGURE 3.3: Change in $O_2^{\bullet -}$ concentration in $SOD(-)\,GSH(-)$ mutants. (▲) corresponds to the analytical solution according to the simplified system and (■) corresponds to the whole model with numerical methods. Cell concentration has no influence on this pattern of superoxide concentration evolution.

Superoxide summary

The table 3.3 summarizes the superoxide steady-state concentrations.

TABLE 3.3: Superoxide steady-state concentration. Superoxide steady-state concentration. At steady state, the internal concentration is shown for cells in LB at 37 °C without exogenous hydrogen peroxide.

$\left[O_2^{\bullet -}\right]$ **(mol L^{-1})**	**In this work**	**Imlay, Fridovich [18]**
Wild type	2.1×10^{-10}	2.0×10^{-10}
SOD(-) GSH(+)	4.2×10^{-7}	4.9×10^{-7}
SOD(-) GSH(-)	2.4×10^{-6}	6.7×10^{-6}

In a wild-type strain, *Fe* concentration is 10 μM, and, in a SOD$^-$ strain, *Fe* concentration is 80 μM [19].

3.3.2 Internal hydrogen peroxide

Without exogenous stress

In the wild-type strain, $O_2^{\bullet -}$ equilibrium is rapidly reached. Indeed the characteristic time of $O_2^{\bullet -}$ evolution is $\frac{1}{k_2[SOD]} \approx 35\,\mu$s. Therefore we can consider $O_2^{\bullet -}$ as a constant and we can assume that $\left[O_2^{\bullet -}\right](t) \approx \left[O_2^{\bullet -}\right]_\infty$ (supporting information data for demonstration).

So in terms of changes to internal H_2O_2 concentration, we approach $k_1' + {}^1\!/_2 k_2 [SOD] \left[O_2^{\bullet -}\right] \approx k_1' + {}^1\!/_2 k_1$ because $\left[O_2^{\bullet -}\right] \approx \left[O_2^{\bullet -}\right]_\infty$ Let us call $k_1' + {}^1\!/_2 k_1 = k_{prod}$.

That is a first point, $O_2^{\bullet -}$ dismutation by SOD involved nearly an increase of 25 % in the endogenous H_2O_2 production.

Moreover, in the absence of exogenous H_2O_2, we can consider that :

$$[H_2O_2] \ll K_M^{Ahp}, K_M^{Cat}$$

so the differential equation system can be simplified to a linear system:

$$\frac{\mathrm{d}\,[H_2O_2]}{\mathrm{d}t} = k_{prod} - \left(\frac{k_{cat}^{Ahp}\,[Ahp]}{K_M^{Ahp}} + \frac{k_{cat}^{Kat}\,[Cat]}{K_M^{Kat}}\right)[H_2O_2] - k_{diff}\left([H_2O_2] - [H_2O_2]_{out}\right)$$

$$\frac{\mathrm{d}\,[H_2O_2]_{out}}{\mathrm{d}t} = k'_{diff}\left([H_2O_2] - [H_2O_2]_{out}\right)$$

with :

$$k'_{diff} = k_{diff}\frac{n \cdot V_{in}}{V_{out} - nV_{in}}$$

Let us call $\frac{k_{cat}^{Ahp}[Ahp]}{K_M^{Ahp}} + \frac{k_{cat}^{Kat}[Cat]}{K_M^{Kat}} = k_{enz}$, then the differential equation system can be written with a matrix structure:

$$\frac{\mathrm{d}}{\mathrm{dt}}\begin{pmatrix}[H_2O_2]\\ [H_2O_2]_{out}\end{pmatrix} = \begin{pmatrix}k_{prod}\\ 0\end{pmatrix} + \begin{pmatrix}-\left(k_{enz}+k_{diff}\right) & k_{diff}\\ k'_{diff} & -k'_{diff}\end{pmatrix}\begin{pmatrix}[H_2O_2]\\ [H_2O_2]_{out}\end{pmatrix}$$

The matrix eigenvalues are $\lambda_1 > \lambda_2$:

$$\lambda_1 = \frac{-\left(k_{enz}+k_{diff}+k'_{diff}\right)+\sqrt{\left(k_{enz}+k_{diff}+k'_{diff}\right)^2-4k_{enz}k'_{diff}}}{2} < 0$$

$$\lambda_2 = \frac{-\left(k_{enz}+k_{diff}+k'_{diff}\right)-\sqrt{\left(k_{enz}+k_{diff}+k'_{diff}\right)^2-4k_{enz}k'_{diff}}}{2} < 0$$

According to the value of the reaction rate constant, we can make the following approximation: $\lambda_1 \approx -\frac{k_{enz}}{\left(k_{enz}+k_{diff}\right)}k'_{diff}$ and $\lambda_2 \approx -\left(k_{enz}+k_{diff}\right)$.
The full matrix V with columns corresponding to the eigenvectors is:

$$V = \begin{pmatrix}k'_{diff}+\lambda_1 & k'_{diff}+\lambda_1\\ k'_{diff} & k'_{diff}\end{pmatrix}$$

The system becomes $\begin{pmatrix}[H_2O_2]\\ [H_2O_2]_{out}\end{pmatrix} = V\begin{pmatrix}Ae^{\lambda_1 t} & 0\\ 0 & Be^{\lambda_2 t}\end{pmatrix}$
The resolution shows a bi-exponential expression:

$$[H_2O_2] = \left(k'_{diff}+\lambda_1\right)Ae^{\lambda_1 t} + \left(k'_{diff}+\lambda_2\right)Be^{\lambda_2 t} + \frac{k_{prod}}{k_{enz}}$$

$$[H_2O_2]_{out} = k'_{diff}Ae^{\lambda_1 t} + k'_{diff}Be^{\lambda_2 t} + \frac{k_{prod}}{k_{enz}}$$

with

$$A = \frac{\left([H_2O_2]_0 - \frac{k_{prod}}{k_{enz}}\right)k'_{diff} - \left([H_2O_2]_{out0} - \frac{k_{prod}}{k_{enz}}\right)\left(k'_{diff}+\lambda_2\right)}{\left(\lambda_1-\lambda_2\right)k'_{diff}}$$

$$B = \frac{\left([H_2O_2]_0 - \frac{k_{prod}}{k_{enz}}\right)k'_{diff} - \left([H_2O_2]_{out0} - \frac{k_{prod}}{k_{enz}}\right)\left(k'_{diff}+\lambda_1\right)}{\left(\lambda_2-\lambda_1\right)k'_{diff}}$$

In this first approach, $[H_2O_2]_0 = 0$ and $[H_2O_2]_{out0} = 0$: initial concentrations are taken to be zero.

From the very beginning,

$[H_2O_2] \approx (k'_{diff} + \lambda_1)\, A + (k'_{diff} + \lambda_2)\, Be^{\lambda_2 t} + \frac{k_{prod}}{k_{enz}}$ as $e^{\lambda_1 t} \approx 1$ because $|\lambda_1| \approx 0$.

Therefore $A \approx -\frac{k_{prod}}{k_{enz}k'_{diff}}$ and $B = \frac{k_{prod}}{\left(k_{enz}+k_{diff}\right)^2}$

$$k'_{diff} + \lambda_1 = k'_{diff} - \frac{k_{enz}}{(k_{enz} + k_{diff})} k'_{diff} = \frac{k_{diff}}{(k_{enz} + k_{diff})} k'_{diff};$$

$$k'_{diff} + \lambda_2 \approx -\left(k_{enz} + k_{diff}\right);$$

In conclusion : $[H_2O_2] \approx \frac{k_{prod}}{k_{enz}+k_{diff}} \left(1 - e^{-\left(k_{enz}+k_{diff}\right)t}\right)$

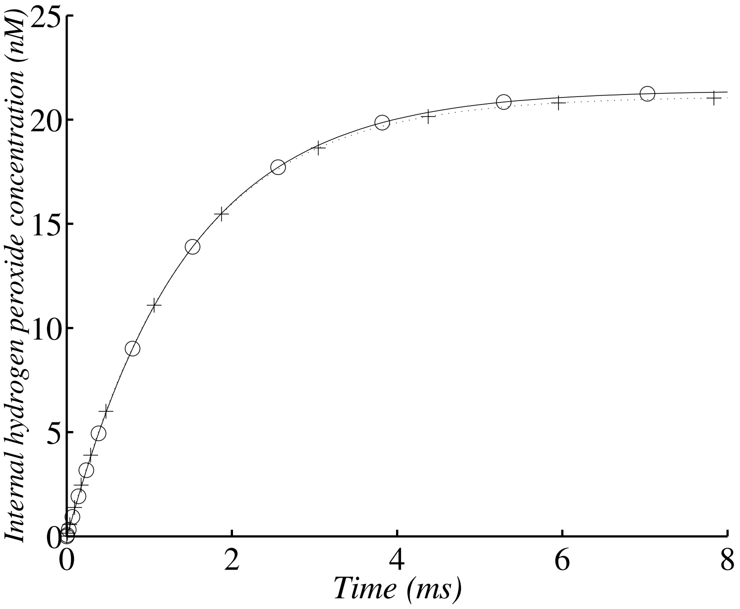

FIGURE 3.4: Changes in internal H_2O_2 concentration in the wild-type strain with 10^7 cells ml^{-1}. (+) corresponds to the analytical solution of internal H_2O_2 evolution according to the simplified system and (○)) corresponds to the whole model solved with numerical methods.

The first plateau (in Fig. 3.4) corresponds to the compromise between production and consumption, but consumption now also depends on diffusion across cell membrane. Indeed, the value of this first plateau is approximately $\frac{k_{prod}}{k_{enz}+k_{diff}}$.

The numerical values are ([4]) :

$$k_{enz} = 633\ \mathrm{s}^{-1} \text{ with } \frac{k_{cat}^{Ahp}[Ahp]}{K_M^{Ahp}} = 550\ \mathrm{s}^{-1}\ ;\ \frac{k_{cat}^{Kat}[Cat]}{K_M^{Kat}} = 83\ \mathrm{s}^{-1}\ ;\ k_{diff} = 70\ \mathrm{s}^{-1}$$

These values indicate that diffusion across the cell membrane accounts for approximately 10 % of the H_2O_2 eliminated, a level of activity close to that of Cat activity ($\approx$ 12 %). As previously reported ([5]), Ahp was identified as the principal scavenger ($\approx$ 78 %).

The first plateau concentration for H_2O_2 is therefore $\frac{k_{prod}}{k_{enz}+k_{diff}} \approx 21$ nM.

For instance, in an Ahp(-) mutant without Cat induction, this concentration would be $\frac{k_{prod}}{\frac{k_{cat}^{Kat}[Cat]}{K_M^{Kat}}+k_{diff}} \approx 97$ nM.

After this transition step, we had $e^{\lambda_2 t} \approx 0$. The change in H_2O_2 concentration therefore follows this equation:

$$[H_2O_2] = \frac{k_{prod}}{k_{enz}} - \frac{k_{prod}}{k_{enz}} \frac{k_{diff}}{(k_{enz}+k_{diff})} e^{\lambda_1 t}$$

This second step is slower and depends on the number of cells, with the final steady-state concentration of H_2O_2 reached more rapidly for denser cell populations (Fig 3.5 and 3.6).

The final steady-state value is $[H_2O_2]_\infty = \frac{k_{prod}}{k_{enz}} \approx 23.5$ nM and is not dependent on cell number. This value is close to that obtained by numerical simulation (23.9 nM) and to that proposed by Imlay (20 nM) ([4]).

For instance, in an Ahp(-) mutant without Cat induction, this value would be $\frac{k_{prod}K_M^{Kat}}{k_{cat}^{Kat}[Cat]} \approx$ 179 nM (identical to the numerical simulation value and close to the value of 100 nM proposed by Seaver and Imlay ([4]).

This second step in the change in H_2O_2 concentration depends on $\lambda_1 \approx -\frac{k_{enz}}{(k_{enz}+k_{diff})} k'_{diff}$, which depends on cell concentration *via* the k'_{diff}.

The results are summarized in Table 3.4.

TABLE 3.4: H_2O_2 steady-state concentration.

$[H_2O_2]$ **(nmol L^{-1})**	**In this work**	**Seaver, Imlay [4]**
Wild type	24	21
HPI+ HPII+ Ahp- ($AhpCF^{(a)}$)	179	100
HPI- HPII- Ahp+ ($KatE\ KatG$)	28	23

At steady state, the internal concentration is shown for cells in LB at 37°C.
(a) without induced HPI levels.

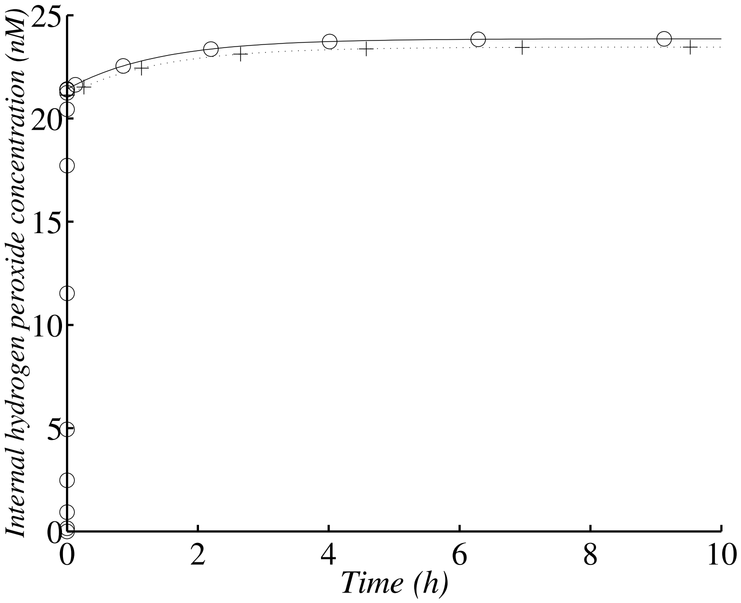

FIGURE 3.5: Changes in internal H_2O_2 concentration in the wild-type strain with 10^6 cells ml^{-1}. (+) corresponds to the analytical solution according to the simplified system and (○)) corresponds to the whole model and a numerical solution.

With exogenous stress

We propose linear approximations of Michaelis-Menten kinetics. Internal H_2O_2 concentration approximately follows the law outlined below. Let us consider an experiment involving the addition of exogenous H_2O_2. The initial *ROS* concentrations in the cell are taken to be the steady-state values obtained without exogenous H_2O_2. The system requires modification as follows :

$$\begin{aligned}\frac{\mathrm{d}\,[H_2O_2]}{\mathrm{d}t} &= k_1' + {}^1\!/_2 k_2\,[SOD]\left[O_2^{\bullet -}\right] \\ &\quad -\frac{k_{cat}^{Ahp}\,[Ahp]\,[H_2O_2]}{[H_2O_2]+K_M^{Ahp}} - \frac{k_{cat}^{Kat}\,[Cat]\,[H_2O_2]}{[H_2O_2]+K_M^{Kat}} \\ &\quad -k_{diff}\left([H_2O_2]-[H_2O_2]_{out}\right)\end{aligned}$$

$$\frac{\mathrm{d}[H_2O_2]_{out}}{\mathrm{dt}} = k_{diff}\frac{n\cdot V_{in}}{V_{out}-nV_{in}}\left([H_2O_2]-[H_2O_2]_{out}\right)$$

As the system is nonlinear there is no analytical solution so with a view to solving

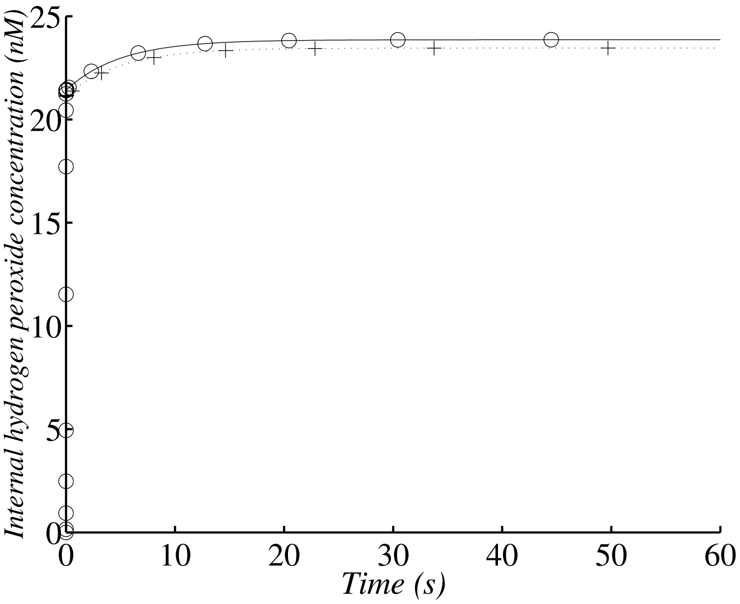

FIGURE 3.6: Changes in H_2O_2 concentration in the wild-type strain with 10^9 cells ml^{-1}. (+) corresponds to the analytical solution according to the simplified system and (○)) corresponds to the whole model and a numerical solution.

the system, we had to compare the value obtained for the internal concentration of H_2O_2 with the K_M values of Ahp and Cat to simplify the Michaelis-Menten expression. Moreover, cell behavior (and thus the dynamic system) depends on the comparison of internal H_2O_2 concentration with the K_M values of Ahp and Cat. This comparison is essential to simplify the system into a linear one, which will then be solvable. This kind of study is frequently carried out and provides useful insight into the workings of systems. For example, Polynikis *et al.* ([20]) compared different modeling approaches (complete nonlinear model, simplified piecewise linear model etc.) for gene regulatory networks using Hill functions, a general form of the Michaelis-Menten equation.

To approximate the Michaelis-Menten hyperbole into a piecewise linear function, let us first examine the contribution of the two enzymes.

The rate (see Fig. 3.7) followed the same pattern of change as that presented by Seaver and Imlay ([5]). Ahp was the leading scavenger in conditions of 17 μM exogenous H_2O_2 (see intersection point in Fig. 3.8).

We can consider that, in the presence of less than 10 μM H_2O_2, Ahp activity is linear (Fig. 3.8) and that Cat activity is linear at concentrations below 10 mM (due to its K_M

value). At H_2O_2 concentrations of more than 30 μM, Ahp activity is saturated.

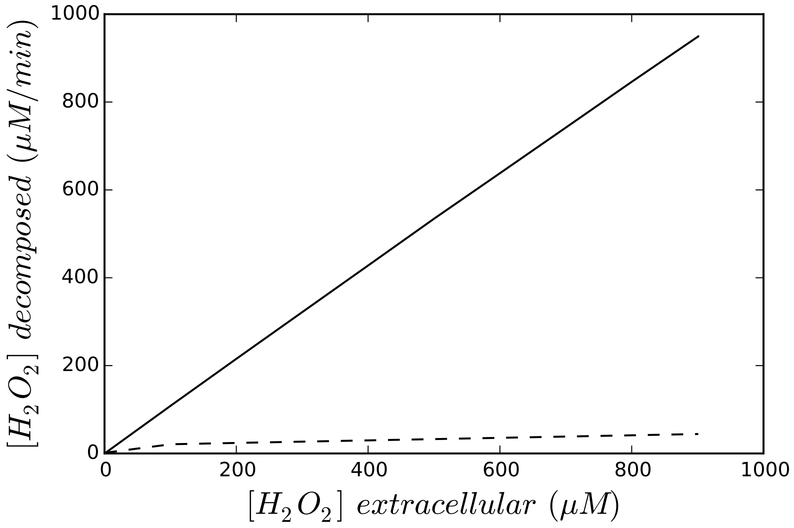

FIGURE 3.7: Kinetics of exogenous H_2O_2 decomposition for 1.5×10^8 *E. coli* cells ml^{-1}. The dotted line corresponds to the Cat(-) mutant and solid line corresponds to the Ahp (-) mutant.

According to the Michaelis-Menten equation, we should consider Ahp activity to be linear when $[H_2O_2] \ll K_M^{Ahp} \approx 1$ μM, but linearity was observed when $[H_2O_2]_{out} < 10$ μM. It is unclear why there is a difference of one order of magnitude between exogenous $[H_2O_2]_{out}$ and internal $[H_2O_2]$ at the limit of linearity.

Such a difference was reported in another experiment presented by Seaver and Imlay ([4]) while studying H_2O_2 fluxes.

In this experiment, whole cells seemed to scavenge H_2O_2 less efficiently than cell extracts. The cell membrane slows the entry of H_2O_2 , resulting in lower rates of decomposition. It also protects cells against high H_2O_2 concentrations, by decreasing the maximum value of H_2O_2 concentration. This phenomenon is described in more detail below. The simulation (Fig. 3.9) for extract was modeled by eliminating membrane diffusion and the metabolism associated with *ROS* production. There is a perfect match between numerical simulation and the experimental results of Seaver and Imlay.

Two situations can be distinguished based on these previous observations.

In the first case, $[H_2O_2] \ll K_M^{Ahp}$ corresponds to $[H_2O_2]_{out} < 10\,\mu$M and to $[H_2O_2] \ll K_M^{Cat}$. The system approaches Michaelis-Menten terms as follows:

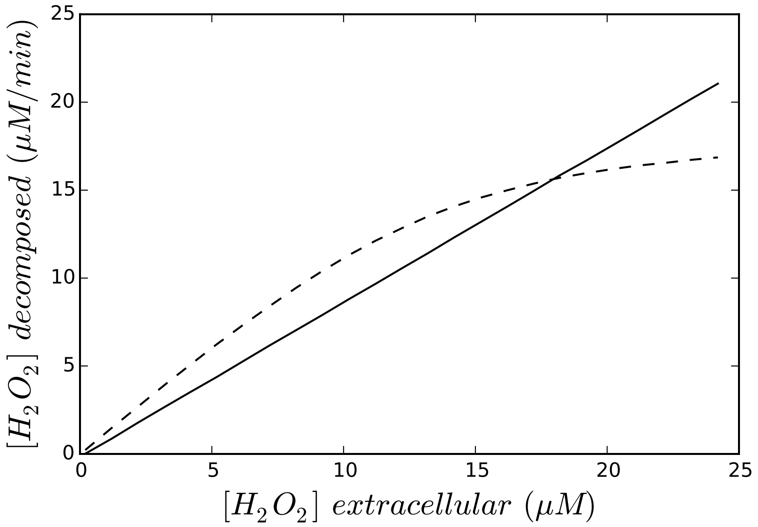

FIGURE 3.8: Kinetics of exogenous H_2O_2 decomposition for 1.5×10^8 *E. coli* cells ml^{-1}. The dotted line corresponds to the Cat(-) mutant and solid line corresponds to the Ahp (-) mutant (higher magnification for Fig. 3.7).

$$\begin{aligned}\frac{k_{cat}^{Ahp}\,[Ahp]\,[H_2O_2]}{[H_2O_2]+K_M^{Ahp}}+\frac{k_{cat}^{Kat}\,[Cat]\,[H_2O_2]}{[H_2O_2]+K_M^{Kat}} &\approx \frac{k_{cat}^{Ahp}\,[Ahp]}{K_M^{Ahp}}+\frac{k_{cat}^{Kat}\,[Cat]}{K_M^{Kat}}\,[H_2O_2]\\ &= k_{enz}\,[H_2O_2]\end{aligned}$$

In the second case, if $[H_2O_2] \gg K_M^{Ahp}$, corresponding to $[H_2O_2]_{out} > 30\,\mu$M and to $[H_2O_2] \ll K_M^{Cat}$, then the system approaches Michaelis-Menten terms as follows :

$$\begin{aligned}\frac{k_{cat}^{Ahp}\,[Ahp]\,[H_2O_2]}{[H_2O_2]+K_M^{Ahp}}+\frac{k_{cat}^{Kat}\,[Cat]\,[H_2O_2]}{[H_2O_2]+K_M^{Kat}} &\approx \left(k_{cat}^{Ahp}\,[Ahp]+\frac{k_{cat}^{Kat}\,[Cat]}{K_M^{Kat}}\right)[H_2O_2]\\ &= k_{cat}^{Ahp}\,[Ahp]+k'_{enz}\,[H_2O_2]\end{aligned}$$

where $\frac{k_{cat}^{Kat}[Cat]}{K_M^{Kat}} = k'_{enz}$.

Then we examine Ahp activity with a micromolar exogenous H_2O_2 concentration. In the first case ($[H_2O_2] \ll K_M^{Ahp}$ and $[H_2O_2] \ll K_M^{Cat}$), the differential equation system appears to be the same as that without exogenous H_2O_2, but $[H_2O_2]_{out} \neq 0$. As

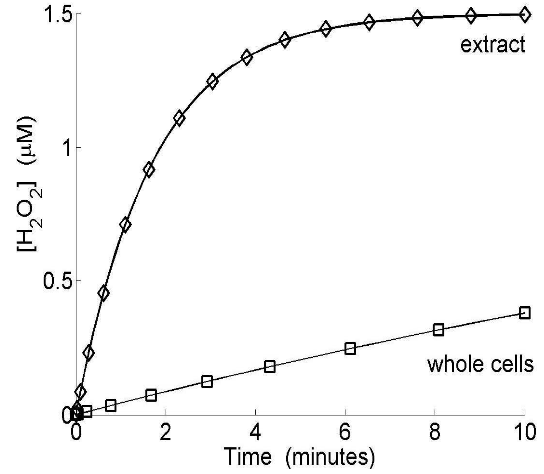

FIGURE 3.9: *In silico*, breakdown of exogenous H_2O_2 by whole cells (Ahp(-) mutant) or cell extract. Simulation runs with 4×10^6 cells ml^{-1}. Moreover, Seaver and Imlay ([5]) observed that an Ahp(-) mutant contained seven times as much total Cat as wild-type cells. We therefore used the same ratio. This figure can be compared with the figure 3.10.

$[H_2O_2]_0 = \frac{k_{prod}}{k_{enz}}$, the constants A and B can be simplified as follows:

$$A = \frac{-\left([H_2O_2]_{out0} - \frac{k_{prod}}{k_{enz}}\right)\left({k'}_{diff} + \lambda_2\right)}{\left(\lambda_1 - \lambda_2\right){k'}_{diff}}$$

and

$$B = \frac{-\left([H_2O_2]_{out0} - \frac{k_{prod}}{k_{enz}}\right)\left({k'}_{diff} + \lambda_1\right)}{\left(\lambda_2 - \lambda_1\right){k'}_{diff}}$$

Moreover as $\lambda_1 \approx -\frac{k_{enz}}{\left(k_{enz}+k_{diff}\right)}k'_{diff}$ and $\lambda_2 \approx -\left(k_{enz} + k_{diff}\right)$ with $|\lambda_1| << |\lambda_2|$ and $|{k'}_{diff}| << |\lambda_2|$

$$\left({k'}_{diff} + \lambda_1\right) A \approx -\left({k'}_{diff} + \lambda_2\right)$$

$$B \approx \left([H_2O_2]_{out0} - \frac{k_{prod}}{k_{enz}}\right) \frac{k_{diff}}{k_{diff} + k_{enz}}$$

therefore:

$$[H_2O_2] = \left([H_2O_2]_{out0} - \frac{k_{prod}}{k_{enz}}\right) \frac{k_{diff}}{k_{diff} + k_{enz}} \left(e^{\lambda_1 t} - e^{\lambda_2 t}\right) + \frac{k_{prod}}{k_{enz}}$$

This bi-exponential function shows that changes in internal H_2O_2 concentration follow

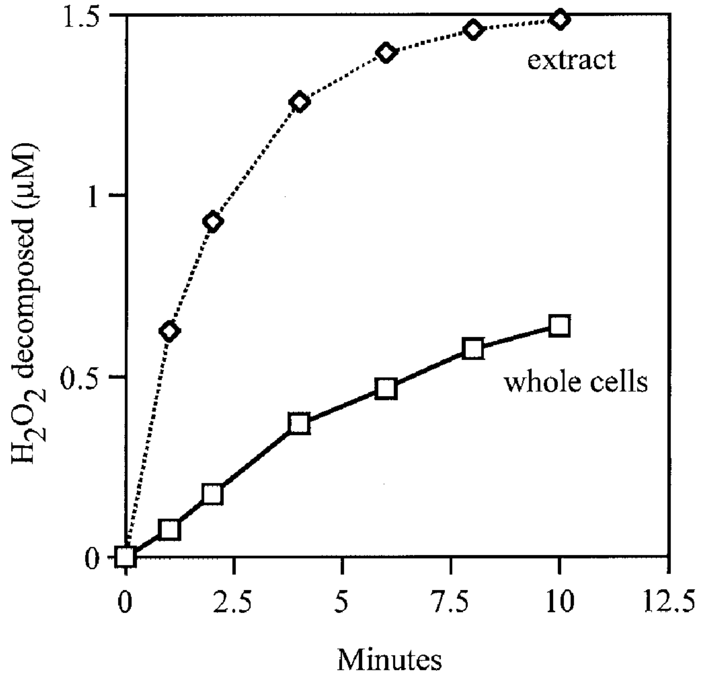

FIG. 2. Decomposition of H_2O_2 by equivalent amounts of extracellular and intracellular HPI. Extract and whole cells of JI372 (*ahpCF katE*) were prepared as described in Materials and Methods, and the decomposition of 1.5 µM H_2O_2 was monitored.

FIGURE 3.10: Extract of Seaver and Imlay [5].

two phases. There is a first phase, with a large rate constant $-\lambda_2 \approx k_{enz} + k_{diff}$ corresponding to the scavenging process, followed by a much slower second phase, with a low rate constant $-\lambda_1 > 0$ corresponding to the diffusion from the external H_2O_2 into the cell. This second phase is faster for larger numbers of cells because k'_{diff} is highly dependent on cell concentration.

$-\lambda_1 \approx \frac{k_{enz}}{(k_{enz}+k_{diff})} k'_{diff}$ and as $k_{enz} \gg k_{diff}$ we can approach $-\lambda_1 \approx k'_{diff}$.

This function therefore reaches a maximum as $\frac{\mathrm{d}[H_2O_2]}{\mathrm{d}t} = 0$ for:

$$t_{\max} = \frac{1}{\lambda_2 - \lambda_1} \ln\left(\frac{\lambda_1}{\lambda_2}\right) \approx \frac{1}{(k_{enz} + k_{diff})} \ln\left(\frac{(k_{enz} + k_{diff})^2}{k_{enz} k'_{diff}}\right)$$

This time is weakly dependent on cell numbers. For example, $t_{\max}$ ≈18 ms with 10^7 cells ml^{-1} and 11 ms with 10^9 cells ml^{-1}.

The maximum internal H_2O_2 concentration is approximately:

$$[H_2O_2]_{\max} \approx \left([H_2O_2]_{out0} - \frac{k_{prod}}{k_{enz}}\right)\frac{k_{diff}}{k_{diff}+k_{enz}} + \frac{k_{prod}}{k_{enz}}$$

and as $[H_2O_2]_{out0} \gg \frac{k_{prod}}{k_{enz}} = [H_2O_2]_{\infty}$ it can be approached by:

$$[H_2O_2]_{\max} \approx \frac{k_{diff}\,[H_2O_2]_{out0}}{k_{diff}+k_{enz}}$$

therefore

$$\frac{[H_2O_2]_{\max}}{[H_2O_2]_{out0}} \approx \frac{1}{1+k_{enz}/k_{diff}} \approx \frac{1}{9}$$

The balance between the elimination processes in the value of the maximal internal H_2O_2 concentration is due to:

$$\frac{k_{cat}^{Ahp}\,[Ahp]}{K_M^{Ahp}\,(k_{enz}+k_{diff})} \approx 78\% \text{ to Ahp}$$

$$\frac{k_{cat}^{Kat}\,[Cat]}{K_M^{Kat}\,(k_{enz}+k_{diff})} \approx 12\% \text{ to Cat}$$

and

$$\frac{k_{diff}}{k_{enz}+k_{diff}} \approx 10\%$$

to elimination by diffusion throughout cell membrane

The maximal value of internal H_2O_2 concentration is almost one tenth the initial exogenous H_2O_2 concentration. This phenomenon reflects the role of the cell membrane in limiting diffusion. The need to diffuse across the cell membrane limits the influx of exogenous H_2O_2 and this process is highly effective at low exogenous H_2O_2 concentrations. The difference of one order of magnitude between exogenous $[H_2O_2]_{out}$ and internal $[H_2O_2]$ arises because the membrane creates a rate-limiting step.

To illustrate this, we will investigate cell behaviour in the presence of 1.5 μM exogenous H_2O_2.

After its peak value (Fig. 3.11), internal H_2O_2 concentration decreases because of scavenging, but diffusion across cell membrane is the process which limits the rate of

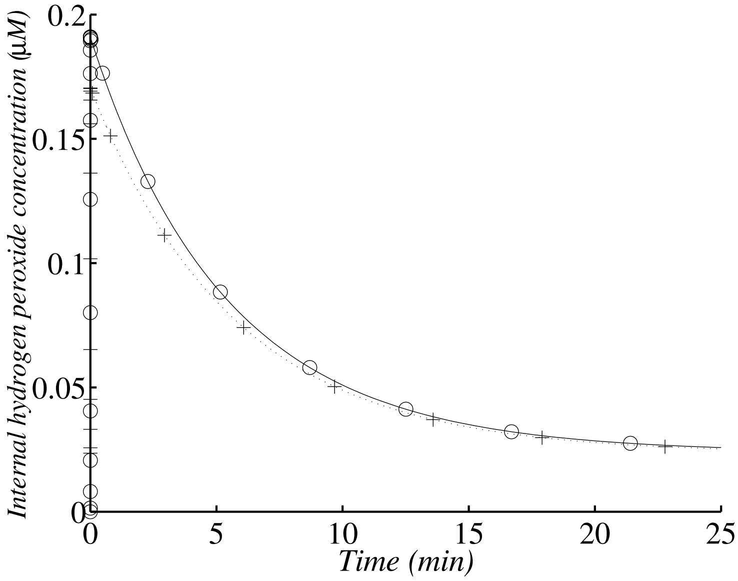

FIGURE 3.11: Changes in internal H_2O_2 concentration in the wild type after the addition of 1.5 μM exogenous H_2O_2 with 1.45×10^7 cells ml^{-1}. (+) corresponds to the analytical solution according to the simplified system and ($\circ$) corresponds to the numerical solution of the whole model. The simulation was run with 1.45×10^7 cells ml^{-1} (corresponding to an OD$_{600}$ value of 0.1).

H_2O_2 disappearance, therefore H_2O_2 decrease is slow. The membrane creates a rate-limiting step.

The maximal value is the approximate value of the first plateau proposed by Gonzalez-Flecha and Demple ([21]). It corresponds to the ratio of the rate of H_2O_2 influx by diffusion to levels of scavenging and elimination by diffusion.

The experiments of Seaver and Imlay ([5]) showed that even non-induced cells scavenged micromolar concentrations of exogenous H_2O_2 very quickly. For example, in a culture corresponding to 0.1 OD$_{600}$ unit (corresponding to around 1.5×10^7 cells ml^{-1}), they found that the half time of H_2O_2 in the medium was only 3.5 minutes, and that in a culture of 1.0 OD unit it was 20 s.

The exogenous H_2O_2 concentration approximately follows the law outlined below:

$$[H_2O_2]_{out} = \left([H_2O_2]_0 - \frac{k_{prod}}{k_{enz}}\right) e^{\lambda_1 t} + \frac{k_{prod}}{k_{enz}}$$

where

$$\lambda_1 \approx -\frac{k_{enz}}{(k_{enz}+k_{diff})}k'_{diff} \approx k'_{diff}$$

Its exponential decrease depends on the k'_{diff} rate constant, which is strongly dependent on cell numbers. The half-life of H_2O_2 in the medium is approximately $t_{1/2} \approx \frac{\ln 2}{k'_{diff}}$ and is a decreasing function of cell number. So, with an OD$_{600}$ of 0.1 (Fig. 3.12) we find that $t_{1/2} \approx 210$ s (3.5 min) and with an OD$_{600}$ of 1 we find that $t_{1/2} \approx 21$ s (Fig. 3.13). A comparison of the experimental data and the analytical results indicates that our model describes the change in H_2O_2 correctly.

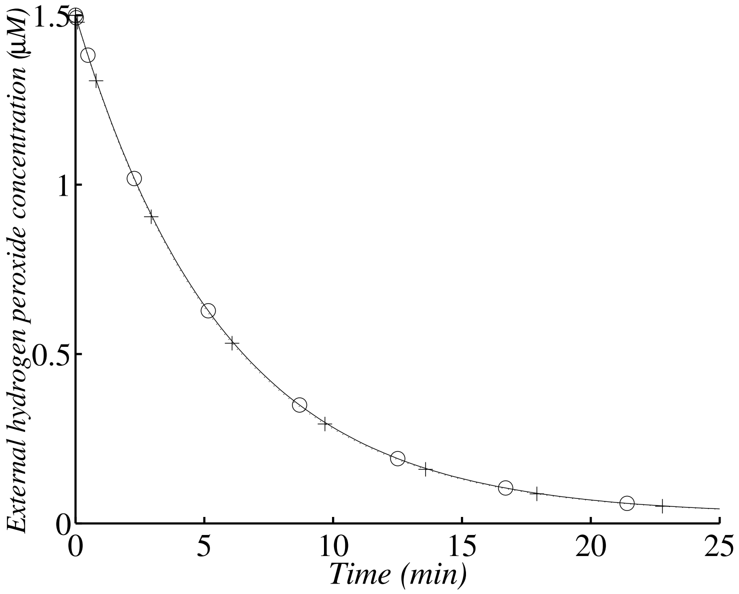

FIGURE 3.12: Changes in external H_2O_2 concentration in the wild type after the addition of 1.5 μM exogenous H_2O_2 with 1.45×10^7 cells ml^{-1}. (+) corresponds to the analytical solution according to the simplified system and ($\circ$)) corresponds to the numerical solution of the whole model. The simulation was run with 1.45×10^7 cells ml^{-1} (corresponding to an OD$_{600}$ value of 0.1).

Finally we examine Ahp activitys, with a high H_2O_2 concentration. In the second

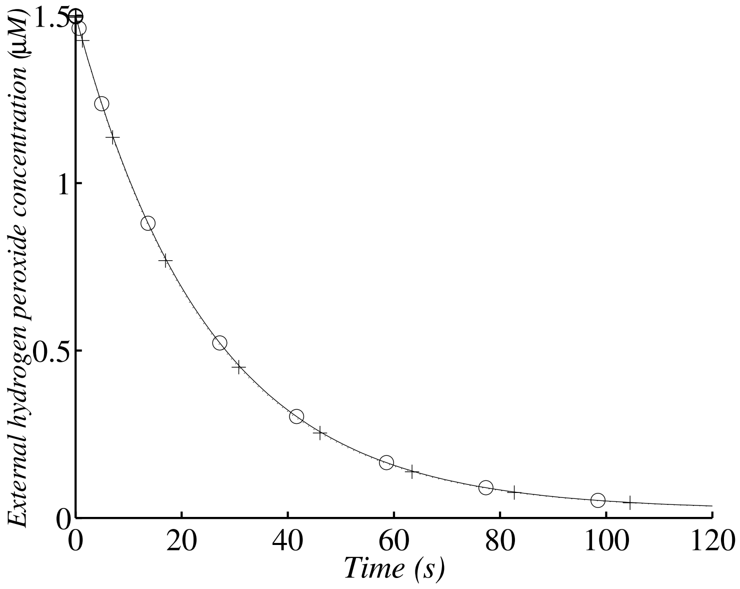

FIGURE 3.13: Changes in external H_2O_2 concentration in the wild type after the addition of 1.5 μM exogenous H_2O_2 with 2×10^8 cells ml^{-1}. (+) corresponds to the analytical solution according to the simplified system and (○)) corresponds to the numerical solution of the whole model. The simulation was run with 2×10^8 cells ml^{-1} (corresponding to an OD$_{600}$ value of 0.1).

case, when $[H_2O_2] \gg K_M^{Ahp}$, corresponding to $[H_2O_2]_{out} > 30\,\mu$M, the differential equation system can be written with a matrix structure:

$$\frac{\mathrm{d}}{\mathrm{d}t}\begin{pmatrix}[H_2O_2]\\ [H_2O_2]_{out}\end{pmatrix} = \begin{pmatrix}k'_{prod}\\ 0\end{pmatrix} + \begin{pmatrix}-\left(k'_{enz}+k_{diff}\right) & k_{diff}\\ k'_{diff} & -k'_{diff}\end{pmatrix}\begin{pmatrix}[H_2O_2]\\ [H_2O_2]_{out}\end{pmatrix}$$

where $k'_{prod} = k'_1 + {}^1\!/_2 k_1 - k_{cat}^{Ahp}\,[Ahp]$ is the usual production reduced by Ahp activity on saturation; and $k'_{enz} = \frac{k_{cat}^{Kat}[Cat]}{K_M^{Kat}}$ (only Cat follows linear kinetics)

The study is similar to the previous one and internal H_2O_2 concentration can be expressed as follows:

$$[H_2O_2] = \left([H_2O_2]_{out0} - \frac{k'_{prod}}{k'_{enz}}\right)\frac{k_{diff}}{k_{diff}+k'_{enz}}\left(e^{\lambda'_1 t} - e^{\lambda'_2 t}\right) + \frac{k'_{prod}}{k'_{enz}}$$

with the eigenvalue $\lambda_1 \approx -\frac{k'_{enz}}{\left(k'_{enz}+k_{diff}\right)}k'_{diff}$ and $\lambda_2 \approx -\left(k'_{enz}+k_{diff}\right)$

The maximum will be $[H_2O_2]_{\max} \approx \frac{k_{diff}[H_2O_2]_{out0}}{k_{diff}+k'_{enz}}$. With large concentrations of exogenous H_2O_2, $[H_2O_2]_{\max} \approx \frac{k_{diff}[H_2O_2]_{out0}}{k_{diff}+\frac{k_{cat}^{Kat}[Cat]}{K_M^{Kat}}}$. This corresponds to the ratio of the rate of H_2O_2 influx by diffusion to its elimination by Cat or by diffusion only.

This expression shows that the ratio between the initial exogenous H_2O_2 concentration and the maximal internal H_2O_2 concentration in the cell is:

$$\frac{[H_2O_2]_{\max}}{[H_2O_2]_{out0}} \approx \frac{1}{1+\frac{k_{cat}^{Kat}[Cat]}{k_{diff}K_M^{Kat}}} \approx \frac{1}{2.2}(*)$$

The contribution of each elimination process to the value of the maximal internal H_2O_2 concentration is:

$$\frac{k'_{enz}}{k'_{enz}+k_{diff}} \approx 55\ \% \text{ to Cat}$$

$$\text{and } \frac{k_{diff}}{k'_{enz}+k_{diff}} \approx 45\ \% \text{ to elimination by diffusion across the cell membrane}$$

We notice that : $\frac{[H_2O_2]_{\max}}{[H_2O_2]_{out0}}$ is equal to the ratio of elimination by diffusion across the membrane to the sum diffusion and scavenging. Of course, without membrane this ratio will equal 1, so thanks to membrane, enzymes have to face less H_2O_2. Moreover, at high exogenous H_2O_2 concentrations, this ratio is quite different from the one (i.e. 1/9) obtained at low concentration.

For instance, with an initial H_2O_2 exogenous concentration $[H_2O_2]_{out0}$ =1 mM, we obtain $[H_2O_2]_{\max} \approx 0.45$ mM (Fig. 3.14). The maximal value is lower than the exogenous concentration because of diffusion and Cat activity, in this case Ahp is saturated and therefore plays a less important role.

The exogenous H_2O_2 concentration approximately follows the law outlined below:

$$[H_2O_2]_{out} = \left([H_2O_2]_0 - \frac{k_{prod}}{k_{enz}}\right) e^{\lambda'_1 t} + \frac{k_{prod}}{k_{enz}}$$

where

$$\lambda'_1 \approx -\frac{k'_{enz}}{(k'_{enz}+k_{diff})} k'_{diff} \neq k'_{diff}$$

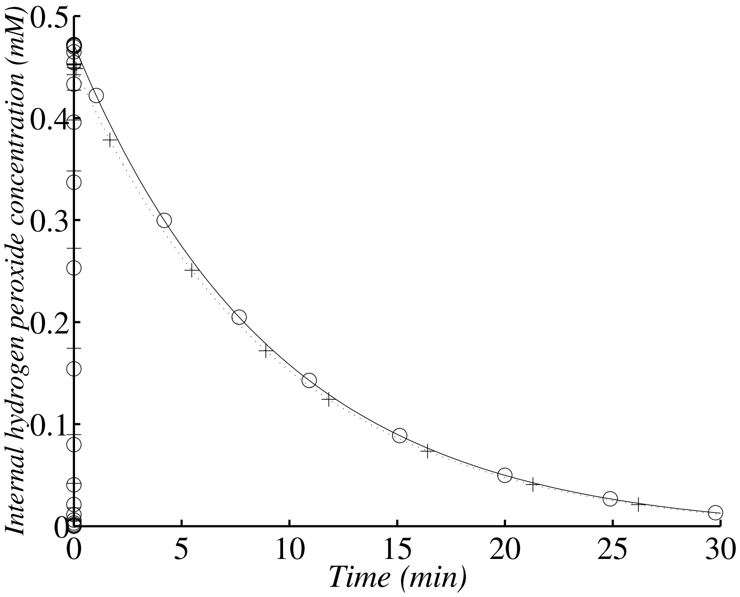

FIGURE 3.14: Changes in internal H_2O_2 concentration in the wild type after the addition of 1 mM exogenous H_2O_2 with 1.45×10^7 cells ml^{-1}. (+) corresponds to the analytical solution according to the simplified system and (∘)) corresponds to the numerical solution of the whole model.

This exponential decrease depends on λ'_1 , which is a cell density function. The decrease rate of H_2O_2 can be characterized by the half-time $t_{1/2}$. This time is approximately the same for internal and external concentration, as internal and external H_2O_2 decrease are strongly linked. For instance, with an addition of 1 mM of exogenous H_2O_2 and with a cell density of 1.45 $\times 10^7$ cells ml^{-1}, the half-live is approximately $t_{1/2} \approx \frac{\ln 1/2}{\lambda'_1} \approx 6.5$ minutes, this results is consistent with Fig. 3.14.

Moreover, as the exponential decrease in rate is dependent on λ'_1, it ranges from zero when there is no scavenger (in a cat- mutant) to k'_{diff} when scavengers have a non-limiting rate constant (much higher than k_{diff}). Thus, a 10-fold induction of Cat (experimentally observed in an Ahp(-) mutant) should increase the rate of medium detoxification of high H_2O_2 concentrations only with a ratio of:

$$\frac{\lambda'_{1,induction}}{\lambda'_1} = \lambda'_1 \approx \frac{10\,(k'_{enz} + k_{diff})}{(10k'_{enz} + k_{diff})} \approx 1.7$$

This result is consistent with the experimental data of Seaver and Imlay ([5]), who examined a doubling in efficiency when comparing the wild type and an Ahp(-) mutant.

It should also be noted that, in a Cat(-) mutant $[H_2O_2]_{\max} \approx [H_2O_2]_{out0} \approx [H_2O_2]_0$ (according to equation *). The maximum internal H_2O_2 concentration rapidly increases the exogenous H_2O_2 concentration and, as there is no Cat, this value remains constant, resulting in the rapid death of the surviving bacteria. The only way to protect Cat(-) mutant cells against high exogenous H_2O_2 concentrations is to add the wild type to the medium. This experiment has been reported by Ma and Eaton ([22]). This point will be examined in the following subsection.

3.3.3 Consequence of defence switch in the primary scavenger

Fig. 3.15 shows that increasing exogenous H_2O_2 concentration involves the switch between the two primary scavengers. This switch has already been reported by Seaver and Imlay ([5]), but we show here another consequence. Actually this switch also triggers a change in the maximal internal H_2O_2 concentration viewed by cell. We also find that this maximal internal concentration does not depend on the cell density. Nevertheless the temporal internal or external H_2O_2 decrease strongly depends on cell density (as previously reported in Fig. 3.11 and Fig. 3.12 or in the previous subsection). The switch between the two scavengers also occurs in Fig. 3.16, actually it shows that H_2O_2 half-life increases when shifting from Ahp to Cat while exogenous H_2O_2 increases.

This switch involves non-linear behaviour in half-life external H_2O_2 dependence. Once again, Ahp seems to be more efficient but it only concerns external H_2O_2 concentration under 10 μM. Above 30 μM, Cat plays the major role. Unlike maximal internal H_2O_2 , half-life depends on cell density, and the more concentrated cells are, the faster medium detoxification occurs. Nevertheless, as reported in Fig. 3.17, under 10 μM (Ahp is the primary scavenger) the half-life does almost not depend on the initial exogenous H_2O_2 concentration. Above 50 μM, Cat is the primary scavenger and the half-life depends on the initial exogenous H_2O_2 concentration.

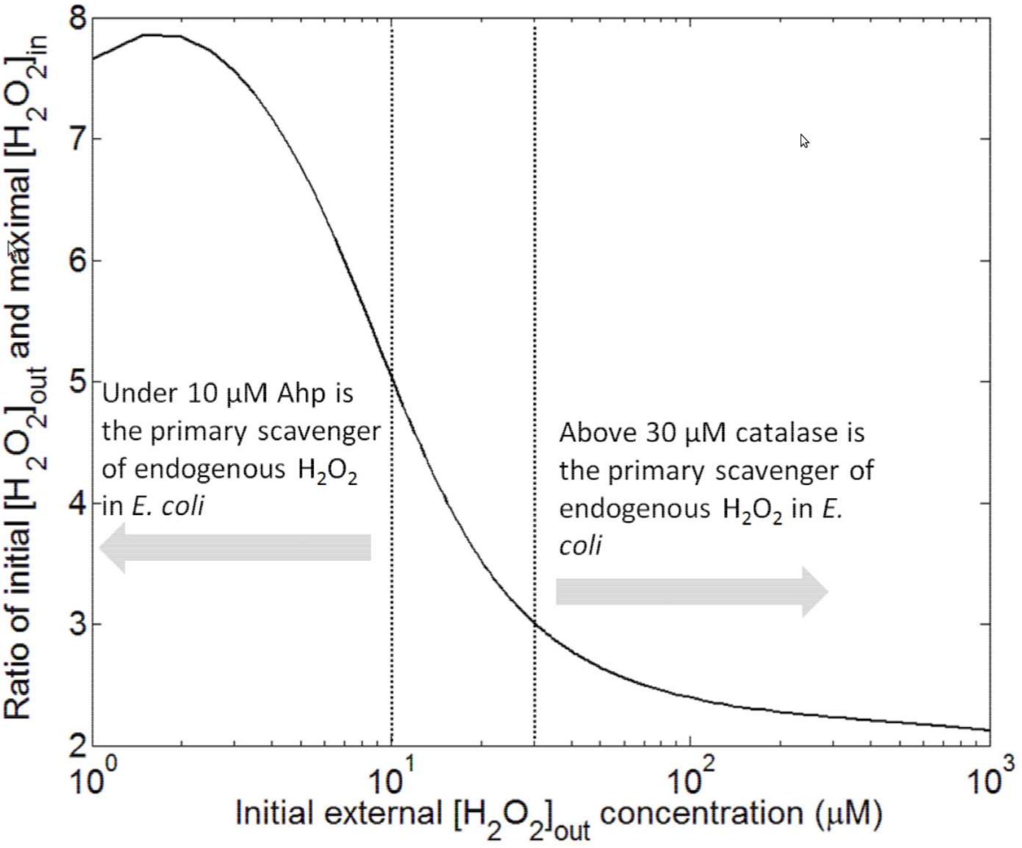

FIGURE 3.15: Changes in the ration between external initial H_2O_2 concentration and internal maximal H_2O_2 concentration in *E. coli* wild type. The numerical solution presented in this graph was running according to the whole model without approximation.

Cumulative internal H_2O_2 concentration, rather than maximum internal H_2O_2 concentration, is involved in the H_2O_2-mediated death of bacterial cells

We investigated whether the decrease in *E. coli* survival with increasing exogenous H_2O_2 concentration was linked to theoretical maximum internal H_2O_2 concentration or to the rate of decrease in internal H_2O_2 concentration. Indeed, a steep decrease indicates the perception of a low mean internal H_2O_2 concentration by the cell. We investigated this aspect by carrying out experiments in which only one of these two parameters was affected at any one time. We therefore reproduced *in silico* the experiments of Ma and Eaton on H_2O_2-mediated killing by *E. coli* wild-type (Cat(+)) or Cat(-) strains alone or by cultures of *E. coli* containing similar numbers of Cat(+) and Cat(-) bacteria. Cat(-) cells from cultures of Cat(-) cells alone or from equal numbers of Cat(-)

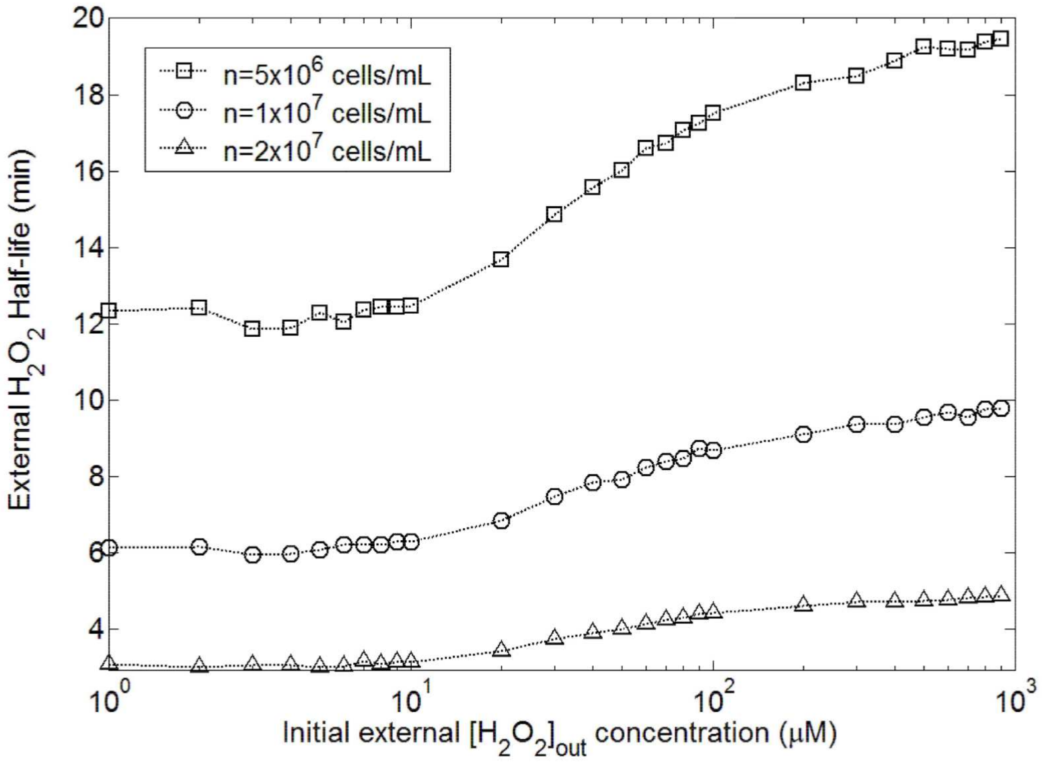

FIGURE 3.16: Changes in external H_2O_2 half-life with different initial external H_2O_2 concentrations and 3 different cell densities in *E. coli* wild type. The numerical solution presented in this graph was running according to the whole model without approximation.

and Cat(+) cells had similar peak H_2O_2 concentrations but different rates of decrease in internal H_2O_2 concentration. This result led us to evaluate the involvement of these two parameters. Moreover, as these experiments were performed with diluted and concentrated cell cultures, giving similar peak H_2O_2 concentrations but different rates of decrease in internal H_2O_2 concentration, we also assessed the effect of these two parameters on cell death.

Simulations were performed with a dilute cell suspension (5×10^2 cells ml^{-1}, Fig. 3.18 and Fig. 3.19) and a higher density of cells (10^7 cells ml^{-1}). Dilute populations of Cat(-) cells were unable to decrease exogenous H_2O_2 concentration. Dilute populations of Cat(+) cells were also unable to detoxify the medium (Fig. 3.18), whereas the dense population of Cat(+) cells halved exogenous H_2O_2 concentration within 10 minutes

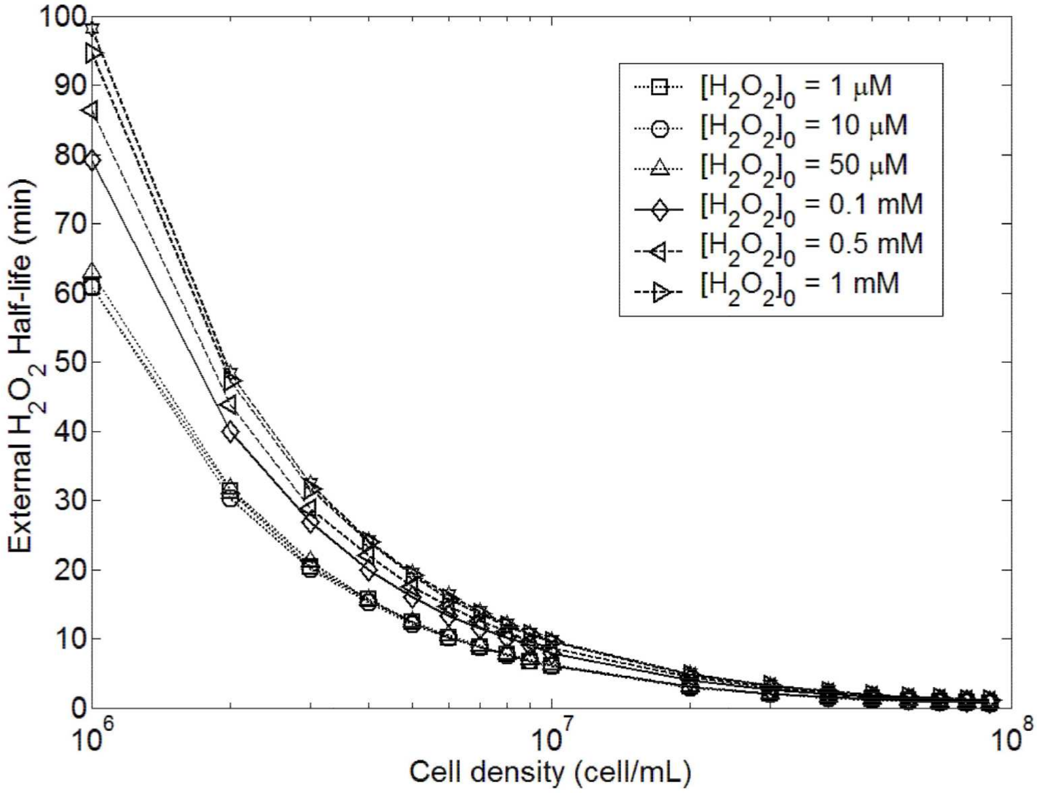

FIGURE 3.17: Changes in external H_2O_2 half-life with cell densities and with 7 different initial external H_2O_2 concentrations in *E. coli* wild type. The numerical solution presented in this graph was running according to the whole model without approximation.

(Fig. 3.18). In a Cat(-) mutant, the maximum internal concentration of H_2O_2 was only 2.5 times higher than that in Cat(+) cells, but survival rates were similar for dilute populations of both Cat(-) and Cat(+) cells ([22]). As a conclusion, the maximum internal concentration of H_2O_2 is not a biological significant factor determining survival rate. Each single cell of the separate Cat(-) and Cat(+) populations had a maximum internal H_2O_2 concentration of about the same magnitude, but only cells from the high-density populations survived in the Eaton experiments. Survival rate was always high when medium detoxification was activated rapidly by a dense Cat(+) cell population. Thus, even Cat(-) *E. coli* can survive if they are mixed with Cat(+) cells able to detoxify the medium. We conclude that H_2O_2 scavengers do not protect individual cells against bulk-phase H_2O_2, because the maximum internal concentration of H_2O_2 did not differ significantly between Cat(-) and Cat(+) cells. The major difference between these two types of cells concerned the rate of decrease in exogenous H_2O_2 concentration and, consequently, the rate of decrease in internal H_2O_2 concentration (Fig. 3.19). We conclude that mean internal H_2O_2 concentration has a significant impact on bacterial survival, whereas maximum internal H_2O_2 concentration does not. So H_2O_2 action can be compared to that of the radiative exposure. This means of action is the opposite of the one generally observed for drugs. For instance, the maximum amount of paracetamol for adults is 4 grams per day with a regular intake of 0.5 gram over 3 days, but a single intake of 10 grams can lead to liver failure ([23]).

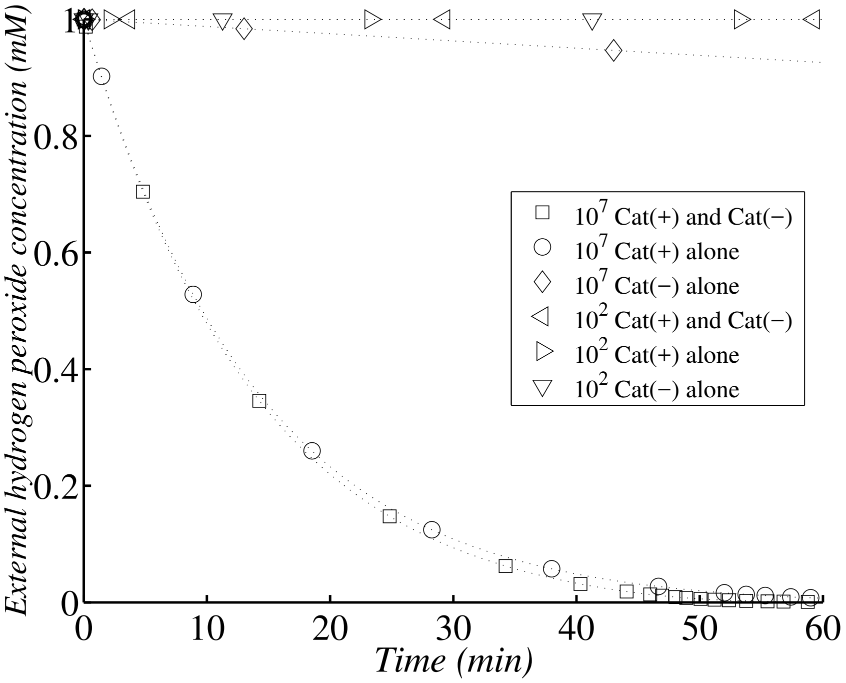

FIGURE 3.18: Simulation of Ma and Eaton experiment following external hydrogen peroxide concentration. Simulation of H_2O_2 external concentration change with dilute (10^2 cells per ml) Cat(-) *E. coli* alone (▽) or Cat(+) *E. coli* alone (▷) or admixed with an equal number of Cat(+),Cat(-) *E. coli* (◁); and with concentrated (10^7 cells per ml) Cat(-) *E. coli* alone (◊) or Cat(+) *E. coli* alone (○) or admixed with an equal number of Cat(+),Cat(-) *E. coli* (□). At zero time, H_2O_2 was added to a final concentration of 1.0 mM, and the bacterial suspension was then incubated at 37°C.

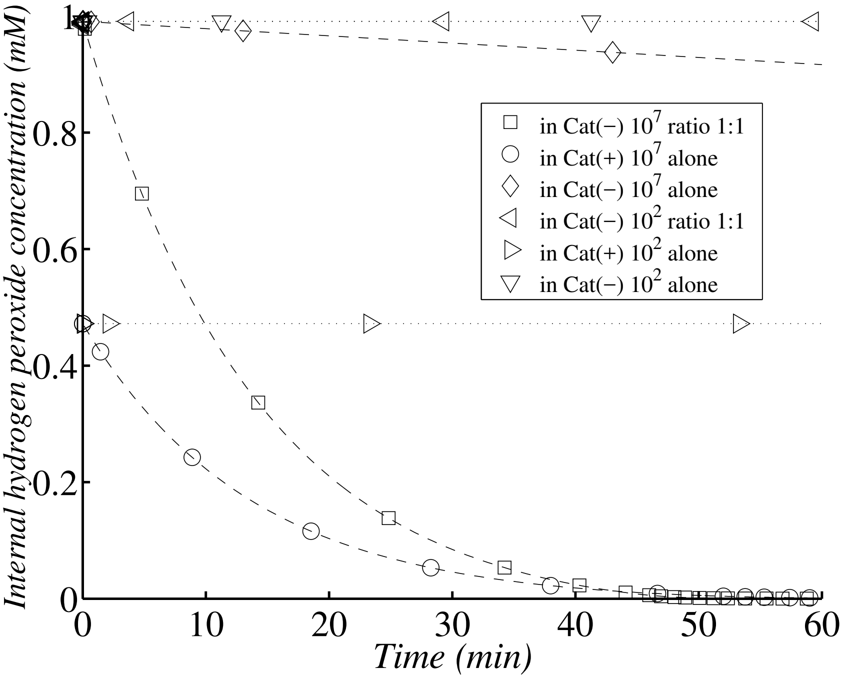

FIGURE 3.19: Simulation of Ma and Eaton experiment following internal hydrogen peroxide concentration. Simulation of H_2O_2 internal concentration change with dilute (10^2 cells per ml) Cat(-) *E. coli* alone (▽) or Cat(+) *E. coli* alone (▷) or admixed with equal numbers of Cat(+),Cat(-) *E. coli* (◁); and with concentrated (10^7 cells per ml) Cat(-) *E. coli* alone (◇) or Cat(+) *E. coli* alone (○) or admixed with equal numbers of Cat(+),Cat(-) *E. coli* (□). At zero time, H_2O_2 was added to a final concentration of 1.0 mM, and the bacterial suspension was then incubated at 37°C.

3.4 Conclusions

3.4.1 In the absence of exogenous stress

An analysis of the most significant kinetic reactions confirmed that steady-state internal concentration H_2O_2 results from the balance between its production and a combination of Ahp degradation (78%), Cat degradation (12%) and membrane permeability (10%).

3.4.2 With exogenous H_2O_2 stress

Prediction of H_2O_2 levels

Under conditions of exogenous H_2O_2 stress, H_2O_2 elimination is dependent on cell density. However, nothing is currently known about internal H_2O_2 concentration during H_2O_2 exposure. Under these conditions, internal H_2O_2 concentration results mostly from influx due to diffusion across the cell membrane, because endogenous production is negligible. Moreover, the rate of diffusion into the cell is governed by membrane permeability. The internal concentration of H_2O_2 must therefore be lower than the exogenous H_2O_2 concentration. Consequently, exogenous H_2O_2 stress leads to an increase in internal H_2O_2 concentration until a maximum is reached. This peak is followed by a decrease in H_2O_2 concentration, due to elimination by the cells. We aimed to identify the most significant parameters (kinetic constants and cell concentrations) accounting for the maximum internal H_2O_2 concentration value reached and for the characteristic time points (time required to reach half the nearest steady–state concentration) during increases and decreases in internal H_2O_2 concentration.

Surprisingly, based on our model, the maximal internal H_2O_2 concentrations reached in individual cells was not dependent on cell density, suggesting that there is no population protection effect. This maximum, which is reached in a few milliseconds, and its characteristic timing, are dependent solely on exogenous H_2O_2 concentration and the three routes of elimination of this radical (membrane permeability, Ahp and Cat scavenging).

For estimation of the maximal internal H_2O_2 concentration, we needed to distinguish internal H_2O_2 concentrations for which Ahp activity predominated from those for which Cat activity predominated. For initial exogenous H_2O_2 concentrations below 10 μM, the maximal internal H_2O_2 concentration was defined by the balance between the exogenous H_2O_2 diffusion rate and the three routes of elimination. In these conditions, Ahp was responsible for about 78 % of all the H_2O_2 eliminated.The peak internal H_2O_2 concentration was almost one tenth the concomitant exogenous H_2O_2 concentration. At initial exogenous H_2O_2 concentrations of more than 30 μM, the peak internal H_2O_2 concentration was defined by the balance between the exogenous H_2O_2 diffusion rate and the possible elimination routes (Ahp activity being negligible due to saturation). Thus, peak H_2O_2 concentrations are determined not only by Cat activity (55 %), but also by membrane permeability (45 %). Surprisingly, at the peak internal H_2O_2 concentration sensed by each cell, limited membrane permeability served as a passive defence against H_2O_2, to a similar extent to Cat. In these conditions, internal H_2O_2 concentration was only half the concomitant exogenous H_2O_2 concentration.

We then showed that the rate of decrease in internal H_2O_2 concentration and its characteristic timing were dependent principally on cell density and membrane permeability. This decrease was mediated not only by enzyme activity, but also by H_2O_2 transport from the extracellular to the intracellular medium. The global kinetics of the decrease in internal H_2O_2 concentration was determined by the slowest step in the process, diffusion across the membrane, which was limited by cell membrane permeability. Finally, similar conclusions were reported for exogenous H_2O_2 concentration. The Imlay group has shown that the elimination rate for exogenous H_2O_2 is much lower in intact cells than in cell extracts, indicating that diffusion across the cell membrane is the limiting process. This observation is consistent with what is known about the most significant kinetic parameters, including the major role played by the cell membrane. Indeed, diffusion across the cell membrane involves the bridging of a gap between internal and extracellular concentrations. This gap provides protection against the oxidizing extracellular medium, but it also decreases the efficiency with which *E. coli* can decrease the H_2O_2 concentration of the extracellular medium (Fig. 3.13). The kinetics of extracellular decomposition is almost exclusively diffusion-dependent and, therefore, very slow. As expected, the rate of H_2O_2 disappearance (intra or extracellular) was greater at higher cell densities.

Instead of conducting real-world experiments, using simulations is generally cheaper, safer and sometimes more ethical. Simulations can also be conducted faster than experiments in real time. For instance, at the University of Pittsburgh School of Pharmacy, high-fidelity patient simulators are used in addition to therapeutics ([24]). Of course simulations have to be confronted with real experiments to test their robustness and to be improved. Our model is one step in a global modelling of the *E. coli* ROS dynamic.

Bibliography

[1] Barry Halliwell, John M. C. Gutteridge, Free radicals in biology and medicine. Clarendon Press, 1989.

[2] J. P. Kehrer, "Free radicals as mediators of tissue injury and disease", Crit. Rev. Toxicol., vol. 23, no. 1, pp. 21–48, 1993.

[3] L. Uhl, A. Gerstel, M. Chabalier, and S. Dukan, "Hydrogen peroxide induced cell death: One or two modes of action?", Heliyon, vol. 1, no. 4, Article e00049, 2015.

[4] L. C. Seaver and J. A. Imlay, "Hydrogen peroxide fluxes and compartmentalization inside growing Escherichia coli", J. Bacteriol., vol. 183, no. 24, pp. 7182–7189, Dec. 2001.

[5] ——, "Alkyl hydroperoxide reductase is the primary scavenger of endogenous hydrogen peroxide in Escherichia coli", J. Bacteriol., vol. 183, no. 24, pp. 7173–7181, Dec. 2001.

[6] J. A. Imlay and S. Linn, "Bimodal pattern of killing of DNA-repair-defective or anoxically grown Escherichia coli by hydrogen peroxide", J. Bacteriol., vol. 166, no. 2, pp. 519–527, May 1986.

[7] ——, "DNA damage and oxygen radical toxicity", Science, vol. 240, no. 4857, pp. 1302–1309, Jun. 1988.

[8] J. Harrison, R. Leggett, D. Lloyd, A. Phipps, and B. Scott, "Polonium-210 as a poison", J Radiol Prot, vol. 27, no. 1, pp. 17–40, Mar. 2007.

[9] D. T. Gillespie, "A general method for numerically simulating the stochastic time evolution of coupled chemical reactions", Journal of Computational Physics, vol. 22, no. 4, pp. 403–434, 1976.

[10] D. T. Gillespie, “Exact stochastic simulation of coupled chemical reactions”, J. Phys. Chem., vol. 81, no. 22, pp. 2340–2361, 1977.

[11] W. H. Koppenol, “The Haber-Weiss cycle–70 years later”, Redox Rep., vol. 6, no. 4, pp. 229–234, 2001.

[12] S. I. Liochev and I. Fridovich, “The Haber-Weiss cycle – 70 years later: an alternative view”, Redox Rep., vol. 7, no. 1, pp. 55–57, 2002.

[13] P. F. Verhulst, “Recherches mathématiques sur la loi d’accroissement de la population”, Nouv. mém. de l’Academie Royale des Sci. et Belles-Lettres de Bruxelles, vol. 18, pp. 1–41, 1845.

[14] ——, “Deuxième mémoire sur la loi d’accroissement de la population”, Mém. de l’Académie Royale des Sci., des Lettres et des Beaux-Arts de Belgique, vol. 20, pp. 1–32, 1847.

[15] B. Demple and J. Halbrook, “Inducible repair of oxidative DNA damage in Escherichia coli”, Nature, vol. 304, no. 5925, pp. 466–468, 1983.

[16] D. E. Chang, D. J. Smalley, and T. Conway, “Gene expression profiling of Escherichia coli growth transitions: an expanded stringent response model”, Mol. Microbiol., vol. 45, no. 2, pp. 289–306, Jul. 2002.

[17] J. A. Imlay and I. Fridovich, “Assay of metabolic superoxide production in Escherichia coli”, J. Biol. Chem., vol. 266, no. 11, pp. 6957–6965, Apr. 1991.

[18] J. Imlay and I. Fridovich, “Assay of metabolic superoxide production in escherichia coli.”, Journal of Biological Chemistry, vol. 266, no. 11, pp. 6957–6965, 1991.

[19] K. Keyer and J. A. Imlay, “Superoxide accelerates dna damage by elevating free-iron levels”, Proceedings of the National Academy of Sciences, vol. 93, no. 24, pp. 13 635–13 640, 1996.

[20] A. Polynikis, S. J. Hogan, and M. di Bernardo, “Comparing different ODE modelling approaches for gene regulatory networks”, J. Theor. Biol., vol. 261, no. 4, pp. 511–530, Dec. 2009.

[21] B. Gonzalez-Flecha and B. Demple, “Metabolic sources of hydrogen peroxide in aerobically growing Escherichia coli”, J. Biol. Chem., vol. 270, no. 23, pp. 13 681–13 687, Jun. 1995.

[22] M. Ma and J. W. Eaton, “Multicellular oxidant defense in unicellular organisms”, Proc. Natl. Acad. Sci. U.S.A., vol. 89, no. 17, pp. 7924–7928, Sep. 1992.

[23] R. C. Dart, A. R. Erdman, K. R. Olson, G. Christianson, A. S. Manoguerra, P. A. Chyka, E. M. Caravati, P. M. Wax, D. C. Keyes, A. D. Woolf, E. J. Scharman, L. L. Booze, and W. G. Troutman, “Acetaminophen poisoning: an evidence-based consensus guideline for out-of-hospital management”, Clin Toxicol (Phila), vol. 44, no. 1, pp. 1–18, 2006.

[24] K. Lin, D. V. Travlos, J. W. Wadelin, and P. H. Vlasses, “Simulation and introductory pharmacy practice experiences”, Am J Pharm Educ, vol. 75, no. 10, p. 209, Dec. 2011.

Chapter 4

ROS stochasticity can explain single cell biological specialization

4.1 Introduction

Physical laws applied to macroscopic systems are generally not adequate for microscopic systems. For example, Newton's laws of motion can solve the fall of a ball but in order to understand the fall of a neutron we have to use the Schrödinger equation. With the same idea, Arrhenius [1] or Eyring [2] laws describe chemical kinetics and they are suitable for macroscopic systems and can describe chemical reactions in a beaker where the number of molecules is large enough to obey statistical thermodynamics, indeed let us remember that in 1 mole there are approximately 6×10^{23} molecules ! But when the beaker becomes a cell, the system size forces us to re-examine our point of view. Using *E. coli*, Imlay and Fridovich [3] found that superoxide ($O_2^{\bullet -}$) steady state concentration is about 0.21 nM in a cell with a volume near 3×10^{-15} L, this value corresponds to 0.38 molecule ! This number cannot follow the usual macroscopic laws. Considering the Arrhenius law, $e^{-E_a/RT}$ (where E_a is the activation energy) represents the probability that any given collisions will result in a reaction. 0.38 molecule corresponds to an average value, but if we want to see a reaction (collision with a molecule in a cell) we have to take at least 1 molecule, but 1 molecule represents 3 times the average value. However, 0.38 molecule also means that overall, one in three cells meets a $O_2^{\bullet -}$ per unit of time, but which is the chosen cell ? It is like a wheel of fortune. Actually, we realize that we have to forget the macroscopic point of view often described by ordinary differential equation (ODE) and we have to focus on the stochastic behaviour of the cell system and to use stochastic algorithms.

An essential point of this study is to follow the concentration of specific molecules (ROS) which are present in low quantities. Let us consider a molecule which induces the transcriptional activator or which is involved in the induction of the transcriptional activator, even a small variation in its intracellular pool can cause greater disturbance in the transcriptional activation. Therefore any noise involved by this molecular variability may have consequences on variability in gene expression.

Noise trigged by stochasticity has many roles in biological systems. For example, noise generates errors in DNA replication leading to mutation and evolution, amplifies or switching signals, drives divergence of cell fates [4] or simply maintains cell individuality. According to biologists, noise mainly comes from multiple origins, such as variability in the activity of individual genes, variations in metabolic activity, or fluctuation of an external stress. Noise is now commonly admitted by the scientific community and it appears to be a dogma at the single-molecule level in living cells [5]. Whereas Van Kampen [6] investigated in a theoretical manner the possibility that variability is inevitable in biological systems because of the random nature of chemical reactions within a cell there is currently no concrete example of noise origin. In this chapter we come back to this crucial origin of noise and show an example of elementary chemical reactions that generate stochastic noise.

E. coli provided an excellent model to study responses to oxidative stress [7, 8] therefore we study the reactive oxygen species distributions and the consequence of those distributions on *E. coli* DNA damage.

4.2 Material and methods

We have already studied $HO^\bullet$ [9], H_2O_2 and $O_2^{\bullet -}$ [10] evolution in *E. coli* with a deterministic description using ODE. These previous studies focused on the consequence of H_2O_2 exogenous stress and introduced more reactions but in the present study we only consider wild type *E. coli* fate without exogenous stress. The following subsections present the assumptions and the ROS dynamics we used to describe our system.

4.2.1 Superoxide kinetics

$O_2^{\bullet-}$ is mainly involved in the following kinetically significant reactions:

Its production :

$$metabolism\, production \xrightarrow{k_1} O_2^{\bullet-}$$

Its dismutation by superoxide dismutase (SOD) scavenger of $O_2^{\bullet-}$.

$$O_2^{\bullet-} + H^+ \xrightarrow[SOD]{k_2} \frac{1}{2}H_2O_2 + \frac{1}{2}O_2$$

These two reactions lead to the following ODE coming from the balance between production and dismutation by SOD:

$$\frac{\mathrm{d}\left[O_2^{\bullet-}\right]}{\mathrm{d}t} = k_1 - k_2\,[SOD]\left[O_2^{\bullet-}\right]$$

4.2.2 Internal hydrogen peroxide kinetics

H_2O_2 appears significantly in the following reactions:

Its productions :

$$metabolism\, production \xrightarrow{k_1'} H_2O_2$$

$$O_2^{\bullet-} + H^+ \xrightarrow[SOD]{k_2} \frac{1}{2}H_2O_2 + \frac{1}{2}O_2$$

Its dismutation by catalase (Cat) or Alkylhydroperoxidase (Ahp)

$$H_2O_2 \xrightarrow{Cat} H_2O + \frac{1}{2}O_2$$

$$H_2O_2 \xrightarrow{Ahp} H_2O + \frac{1}{2}O_2$$

Its diffusion across cell membrane

$$H_2O_2 \xrightarrow{k_{diff}} H_2O_{2out}$$

k_{diff} was calculated using the membrane permeability coefficient ($P = 1.6 \times 10^{-3}$ cm/s), the membrane surface area ($A = 1.41 \times 10^{-7}$ cm^2) and cell volume ($V = 3.2 \times 10^{-15}$ L) given by Seaver and Imlay [11], therefore $k_{diff} = \frac{P \times S}{V}$.

The ODE becomes :

$$\begin{aligned}\frac{\mathrm{d}\,[H_2O_2]}{\mathrm{d}t} &= k_1' \\ &+\frac{1}{2}k_2\,[SOD]\,\left[O_2^{\bullet -}\right] \\ &-\frac{k_{cat}^{Ahp}\,[Ahp]\,[H_2O_2]}{[H_2O_2]+K_M^{Ahp}} - \frac{k_{cat}^{Kat}\,[Cat]\,[H_2O_2]}{[H_2O_2]+K_M^{Kat}} \\ &-k_{diff}\,([H_2O_2]-[H_2O_2]_{out})\end{aligned}$$

where H_2O_{2out} corresponds to H_2O_2 in the external habitat of the cell.

K_M (K_M^{Kat} for catalase and K_M^{Ahp} for alkylhydroperoxidase) is the Michaelis constant. k_{cat} (k_{cat}^{Kat} for catalase and k_{cat}^{Ahp} for alkylhydroperoxidase) is the turnover number, it represents the maximum number of molecules (here H_2O_2) that an enzyme is able to convert into products per second.

4.2.3 External hydrogen peroxide

$$\frac{\mathrm{d}\,[H_2O_2]_{out}}{\mathrm{d}t} = k_{diff}\frac{n \cdot V_{in}}{V_{out}-nV_{in}}\left([H_2O_2]-[H_2O_2]_{out}\right)$$

The cell density is given by n. V_{in} represents the internal cell volume and V_{out} corresponds to the total volume. Of course, as microorganisms cannot take up more space than their medium, we have the inequality $V_{out} - nV_{in} \gg 0$.

Moreover, as we consider only low cell density, we assume that $\frac{V_{in}}{V_{out}} \ll 1$ involves $\frac{\mathrm{d}[H_2O_2]_{out}}{\mathrm{d}t} \to 0$ and therefore we can consider $[H_2O_2]_{out}$ as a constant which is also negligible because we set no exogenous H_2O_2 stress. Biologically it means that we have to take into account the H_2O_2 flux from inside to outside whereas we can neglect the

H_2O_2 flux from outside to inside because of the low cell density and the absence of exogenous H_2O_2 stress.

4.2.4 Kinetic constants

The kinetic constants used in this work are collected in the table 4.1 (concerning superoxide) according to Imlay and Fridovich [3] and in table 4.2 (concerning H_2O_2) according to Seaver and Imlay [12].

TABLE 4.1: Kinetic constants used to describe $O_2^{\bullet -}$ evolution.

Kinetic constants	
k_1	5.7×10^{-6} mol·L^{-1}·s^{-1}
$k_2[SOD]$	2.8×10^{4} s^{-1}
k_2	1.5×10^{9} mol^{-1}·L·s^{-1}
V_{in}	3×10^{-15} L

TABLE 4.2: Kinetic constants used to describe H_2O_2 evolution.

Kinetic constants	
k_1'	12×10^{-6} mol·L^{-1}·s^{-1}
$k_{cat}^{Ahp}[Ahp]$	6.6×10^{-4} mol·L^{-1}·s^{-1}
K_M^{Ahp}	1.2×10^{-6} mol·L^{-1}
$k_{cat}^{Ahp}[Ahp]/K_M^{Ahp}$	550 s^{-1}
$k_{cat}^{Ahp}[Ahp]$	6.6×10^{-4} mol·L^{-1}·s^{-1}
$k_{cat}^{Kat}[Cat]$	4.9×10^{-1} mol·L^{-1}·s^{-1}
K_M^{Kat}	5.9×10^{-3} mol·L^{-1}
$k_{cat}^{Kat}[Cat]/K_M^{Kat}$	83 s^{-1}
k_{diff}	70 s^{-1}

4.2.5 Hydroxyl radical

The $HO^{\bullet}$ production is given by the Fenton reaction which gives:

$$\frac{\mathrm{d}\,[HO^{\bullet}]}{\mathrm{d}t} = k_f\,[Fe]\,[H_2O_2]$$

Let us consider iron concentration as a constant, indeed without exogenous H_2O_2 stress iron concentration sees no significant change. Its concentration is set to 20 μM. This assumption has been extensively covered by Uhl *et al.* [9].

We then consider N reactions of rate constant k_i between an organic X_i compound (proteins, metabolites,...) and $HO^{\bullet}$. Nevertheless, DNA was treated separately (out of the sum) in order to examine its damage during oxidative stress, therefore the following equations come:

$$\frac{d\left[HO^{\bullet}\right]}{dt} = k_F\left[Fe^{2+}\right]\left[H_2O_2\right] - \sum_{i=1}^{N} k_i\left[X_i\right]\left[HO^{\bullet}\right] - k_{DNA}\left[DNA\right]\left[HO^{\bullet}\right]$$

$$\frac{d\left[DNA\right]}{dt} = -k_{DNA}\left[DNA\right]\left[HO^{\bullet}\right]$$

4.2.6 Transcription factors that defend *E. coli*

To protect itself from H_2O_2 and $O_2^{\bullet -}$, *E. coli* mainly activates regulons controlled by OxyR ans SoxR transcription factors.

When stressed under elevated levels of $O_2^{\bullet -}$, *E. coli* responds by inducing SOD [13, 14]. SoxR is a [2Fe-2S]-containing transcription factor that binds near the $soxS$ promoter and senses the stress. SoxR induces transcription of $soxS$. SoxS is a second transcription factor that then activates scores of defensive genes that encode proteins which suppress the toxicity of $O_2^{\bullet -}$. SoxRS involvement will be discussed in relation to $O_2^{\bullet -}$ concentration level found in our simulation in the next section. We will neglect the soxRS response and check this assertion ex-post.

To address the problems that H_2O_2 causes, *E. coli* also maintains inducible defensive regulons governed by OxyR transcription factors. Like the SoxRS system, OxyR is not activated during normal aerobic growth. This transcription factor does not control the basal level of defensive systems but it becomes active when elevated concentrations of H_2O_2 emerge. Nevertheless, as OxyR quickly responds to submicromolar concentrations of H_2O_2 we included OxyR in our system (its influence is developed in the next subsections and indeed shows no activation without exogenous oxidative stress, our results indicate that the stochastic behaviour of OxyR can be neglected).

E. coli responds to DNA damage by a highly orchestrated series of events known as the SOS response [15–18]. A few dozen genes are involved in this mechanism, most of them are regulated by the transcriptional repressor LexA. Among these, the recA gene plays a major role in DNA repair. But induction of the SOS response by H_2O_2 [19] or by ultraviolet irradiation [20] in *E. coli* is clearly negligible in the next 5 minutes after the stress. Therefore we do not take into account the SOS response in our model.

4.2.7 Simulation

We use the standard assumption for biochemical models considering that the spatial distribution of reactants is homogeneous. Actually with this hypothesis, the system can be described with ODE easy to compute. The system is a square lattice of 32 by 32 cells corresponding to a dilute cell concentration of 10^3 cell/mL. According to this dilution we assume that cell interactions are negligible therefore we do not consider molecule diffusion from one cell to another.

One way to handle the vast state space of cell molecules distribution is to use the Next Sub-volume Method, a Gillespie [21, 22] like mesoscopic and stochastic algorithm proposed by Elf *et al.* [23, 24] and developed in chapter 1. At each time interval, the reaction that occurs is chosen randomly according to the probabilities for the reaction to take place in a cell. The probabilities depend on both the number of molecules and the rate constants. We adapt the algorithm considering each cell as a sub-volume where molecules are homogeneously distributed. There is no diffusion from one cell to another.

In the initial configuration all cells own the same number of each molecule so that there was no imbalance between two cells. Moreover we cancel extrinsic noise due to the random fluctuations in environmental parameters (such as cell-to-cell variation in temperature, pH, kinetic parameters, number of ribosomes,...) by taking all parameters as constants. Therefore at the end of the simulation, the observed imbalances will only appear as a consequence of the stochastic nature of chemical reactions. Indeed we only focus on the consequences of intrinsic noise resulting from the probabilistic character of the chemical reactions following exponential laws according to Arrhenius and Eyring.

Stochastic simulations were run with Python3 [25].

4.3 Results and discussion

This section first presents the analytical study of the dynamic system. This analysis will provide us with insight into the kinetic parameters significantly important for the dynamics of ROS. Then we compare those average deterministic results with the stochastic simulation which will provide us with more accurate information on cell damage distribution.

4.3.1 Deterministic previsions

Superoxide

In the wild-type strain, without exogenous stress, the resolution of $O_2^{\bullet-}$ concentration gives :

$$\left[O_2^{\bullet-}\right] \approx \left[O_2^{\bullet-}\right]_\infty \left(1 - e^{-k_2[SOD]t}\right)$$

indeed GSH and spontaneous dismutation are negligible because rate constants are much lower than the SOD one ($k_{sp}\left[O_2^{\bullet-}\right] \ll k_{GSH}\left[GSH\right] \ll k_2\left[SOD\right]$). $O_2^{\bullet-}$ concentration rapidly reached its steady-state value, in less than 1 ms, the characteristic time is given by $\frac{1}{k_2[SOD]}$. This time, which was dependent solely on SOD concentration and the SOD catalytic degradation rate k_2, corresponds to the characteristic time required for the re-establishment of equilibrium.

If we assume that SOD concentration and $O_2^{\bullet-}$ production change over time (because of fluctuations in environmental parameters), and that their equilibrium time values are probably significantly shorter than 1 ms, then the steady-state value of $O_2^{\bullet-}$ concentration is always reached but depends purely on $O_2^{\bullet-}$ production rate and SOD catalytic degradation rate (k_2), which are time-dependent.

For each time, we can write that the $O_2^{\bullet-}$ concentration is $\left[O_2^{\bullet-}\right](t) = \frac{k_1(t)}{k_2[SOD](t)}$. For example, with published values [3], $O_2^{\bullet-}$ concentration is 2.1×10^{-10} M : this value fits the Imlay prediction well, and it corresponds to the equilibrium between $O_2^{\bullet-}$ production (parameter k_1) and the rate of scavenging of this radical by SOD.

In conclusion, in a wild strain, the two major reactions involving superoxide (its production and its consumption by SOD) lead to a $O_2^{\bullet-}$ concentration at steady state near 2.1×10^{-10} M without fluctuations in environmental parameters. This value corresponds to 0.38 molecule of $O_2^{\bullet-}$ and it means that we found approximately 1 molecule of $O_2^{\bullet-}$ per 3 cells per unit of time.

Hydrogen peroxide

In the wild-type strain, without exogenous stress, $O_2^{\bullet-}$ equilibrium is rapidly reached, so, in terms of changes to internal H_2O_2 concentration, we approach $k_1' + {}^1\!/\!_2 k_2 [SOD] \left[O_2^{\bullet-}\right] \approx k_1' + {}^1\!/\!_2 k_1$ because $\left[O_2^{\bullet-}\right] \approx \left[O_2^{\bullet-}\right]_\infty$. Let us call $k_1' + {}^1\!/\!_2 k_1 = k_{prod}$.

That's a first point, superoxide dismutation by SOD involved nearly an increase of 25 % in the endogenous H_2O_2 production.

Moreover, in the absence of exogenous H_2O_2, we can consider that :

$$[H_2O_2] \ll K_M^{Ahp}, K_M^{Cat}$$

so the differential equation system can be simplified to a linear system:

$$\frac{\mathrm{d}\,[H_2O_2]}{\mathrm{d}t} = k_{prod} - \left(\frac{k_{cat}^{Ahp}\,[Ahp]}{K_M^{Ahp}} + \frac{k_{cat}^{Kat}\,[Catalase]}{K_M^{Kat}} \right) [H_2O_2] - k_{diff}\left([H_2O_2] - [H_2O_2]_{out}\right)$$

Let us assume $[H_2O_2]_{out} = 0$ (because of low cell density).
Let us call $\frac{k_{cat}^{Ahp}[Ahp]}{K_M^{Ahp}} + \frac{k_{cat}^{Kat}[Catalase]}{K_M^{Kat}} = k_{enz}$, then the differential equation becomes :

$$\frac{\mathrm{d}\,[H_2O_2]}{\mathrm{d}t} = k_{prod} - (k_{enz} + k_{diff})\,[H_2O_2]$$

The approximated H_2O_2 steady state is:

$$[H_2O_2]_\infty = \frac{k_{prod}}{k_{enz} + k_{diff}}$$

After a characteristic time near 2 ms ($\frac{1}{k_{enz}+k_{diff}}$), H_2O_2 concentration reaches a steady state concentration of 21 nM, this value corresponds to mean of 38 molecules of H_2O_2 per cell without extrinsic noise.

Hydroxyl radical production

Because of the low characteristic time, we consider the H_2O_2 steady state concentration as a constant because it is immediately reached. The $HO^\bullet$ production flux ($HO^\bullet$ amount production per time of unit and volume) is then :

$$\frac{\mathrm{d}\,[HO^\bullet]}{\mathrm{d}t}(t) = k_f\,[Fe]\,[H_2O_2]_\infty = \frac{k_f k_{prod}\,[Fe]}{k_{enz} + k_{diff}}$$

This result shows a production of 1.8 nM per seconds which corresponds to 3.3 molecules of $HO^\bullet$ produced per second. Then produced $HO^\bullet$ will damage organic compounds according to the differential equation leading to $HO^\bullet$ evolution.

DNA concentration refers to concentration of nitrogenous bases, this concentration is set to 5 $\times 10^{-3}$ M, corresponding to approximately 4.6 $\times 10^6$ pairs (with the proportion of each base set at 25 %, which is close to the value proposed by the CBS genome atlas database of Hallin and Ussery [26]). The rate constant between $HO^\bullet$ and DNA is $k_{DNA} = 4.7 \times 10^9$ M s^{-1} [27].

We then consider N reactions of rate constant k_i between an organic X_i compound (or site) and $HO^\bullet$ ($\sum_{i=1}^{N} k_i\,[X_i]\,[HO^\bullet]$). For instance Bennett et al. [28] report total metabolome concentration of 300 mM (100 million metabolites/cell) greatly exceeded the reported total protein concentration of 7 mM (2.4 million proteins/cell). Nevertheless, with an average of 400 residues per protein, it represents 2.8 M of feeding sites for $HO^\bullet$.

We assume that $\sum_{i=1}^{N} k_i\,[X_i] \approx 7.3\times10^9$ s^{-1} [9], which corresponds to a mean rate constant of 2×10^9 M s^{-1} for reaction between $HO^\bullet$ and organic compounds.

According to the production rate and the $HO^{\bullet}$ consumption, the $HO^{\bullet}$ steady state concentration is

$$[HO^{\bullet}]_{\infty} = \frac{k_f\,[Fe]\,[H_2O_2]_{\infty}}{(\sum_{i=1}^{N} k_i\,[X_i] + k_{DNA}\,[DNA])} = \frac{k_f k_{prod}\,[Fe]}{(k_{enz} + k_{diff})(\sum_{i=1}^{N} k_i\,[X_i] + k_{DNA}\,[DNA])}$$

$HO^{\bullet}$ concentration at steady state is 2.5 $\times 10^{-19}$ M, this value corresponds to a mean of 4.6 $\times 10^{-10}$ molecules of $HO^{\bullet}$. This result means that we count only 1 molecule per 2.3 $\times 10^{9}$ cell at a given time without extrinsic noise !

Therefore DNA damage quantity occurs with a rate of :

$$\frac{\mathrm{d}n_{DNA_{ox}}}{\mathrm{d}t} = k_{DNA}\,[DNA]\,[HO^{\bullet}]\,V_{cell}\mathcal{N}_A$$

which corresponds to 0.01 average DNA damage per cell per second or approximately 12 lesions per cell per generation (assuming a generation of 20 minutes and a constant amount of DNA). For instance, 8-Oxoguanine is one of the most common DNA lesions resulting from reactive oxygen species and Park *et al.* [29] reported nearly 200±50 fM/mL of 8-oxoGua per generation (for *E. coli* $A_{600} = 1$) which represents nearly 120±30 oxidations. On the other hand, when $HO^{\bullet}$ targets nearly 12 DNA per cell per generation, it also targets 3200 other molecules such as proteins, lipids,...

However this deterministic discussion does not take into account ROS distribution in cells. Therefore, in the next section, we will introduce the stochastic results. We present one sample of our results whereas we reproduced multiple simulations which all present very similar distributions.

The OxyR transcription factor

The *E. coli* OxyR transcription factor activates the expression of antioxidant defensive activities such as hydroperoxidase I (katG) and alkylhydroperoxide reductase (ahpCF).

The oxidation of OxyR leads to the formation of an intramolecular disulfide bond between cysteine residues 199 and 208 [30] and only oxidized OxyR (noted $OxyR_{ox}$) is capable of activating transcription.

Pathways of OxyR oxidation (by H_2O_2) and reduction can be divided into the two main reactions:

$$OxyR_{red} + H_2O_2 \xrightarrow{k_{Ox}} OxyR_{ox} + 2H_2O$$

$$OxyR_{ox} + Red \xrightarrow{k_{Red}} OxyR_{red} + Ox$$

These two different reactions can determine the redox status of OxyR. During normal growth of *E. coli*, without exogenous H_2O_2 stress, the reaction rate for the first pathway is low, so the second pathway is predominant. Under these conditions in wild-type strains without exogenous stress, the cellular Red/Ox (principally GSH/GSSG) ratio largely favors reduced OxyR [31]. We then assume that under physiological conditions, OxyR concentration is a constant and is principally reduced. The number of OxyR copies per cell is approximately estimed at 1300 according to Li *et al.* [32], therefore $[OxyR]_0 \approx [OxyR_{red}] \approx 0.7\,\mu$M. Moreover Aslund *et al.* [31] determined that $k_{Ox} \approx 10^5$ M^{-1}s^{-1}.

Aslund *et al.* also reveals that the half life of OxyR deactivation in cells after treatment with 200 μM of H_2O_2 at OD_{600} = 0.1 was 17 min, whereas the half life of deactivation in cells at OD_{600} = 1.6 became 2 min. This time depends on the capacity of a culture to metabolize H_2O_2; of course dense cultures are faster. Moreover this half life is the sum of the time needed to detoxify the medium (until H_2O_2 concentration reached physiological level, it took about 1 minute with dense population, according to the previous chapter) and the time needed to oxidize then re-reduce OxyR. We can conclude that half life for the OxyR deactivation (reduction) should be under 1 min.

In fact Aslund *et al.* [31] reported that the *in vitro* kinetics were similar to the *in vivo* kinetics, complete oxidation of reduced OxyR was observed in 30 sec and a half-time of deactivation of 5–30 min, but this time takes into account OxyR deactivation and the detoxification of the medium. For instance, they examined the *in vivo* kinetics of

OxyR oxidation and reduction after treatment with 200 μM H_2O_2. For wild-type cells ($OD_{600} = 0.4$, we made our simulation with a density of 8×10^7 cell/mL), OxyR was oxidized fully within 30 sec after H_2O_2 was added and 5 minutes after this treatment, half of the OxyR protein was reduced (Figure 4.2. Another experiment showed the half-time of OxyR deactivation in cells at $OD_{600} = 0.1$ (our simulation used 2×10^7 cell/mL) was 17 min. Using $k_{Red}\,[Red] \approx 0.1$ s^{-1}and the kinetic constants in our complete deterministic system based on ordinary differential equations (ODE) (presented in the previous chapter [10]) we reproduced those experiments in the figure 4.1. Those results are consistent with the experiments of Aslund *et al.*.

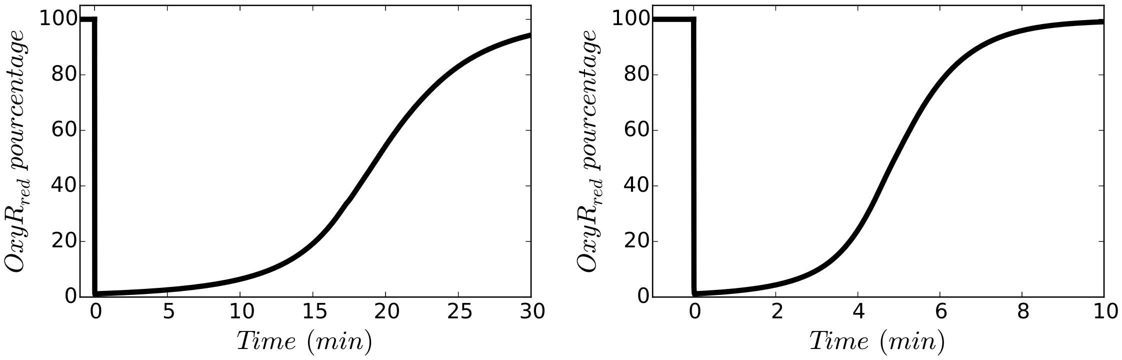

FIGURE 4.1: Numerical simulation of OxyR activation (oxidized) and deactivation (reduced) when *E. coli* was treated with 200 μM of H_2O_2 at $OD_{600} = 0.1$ (left panel) and at $OD_{600} = 0.4$ (right panel)

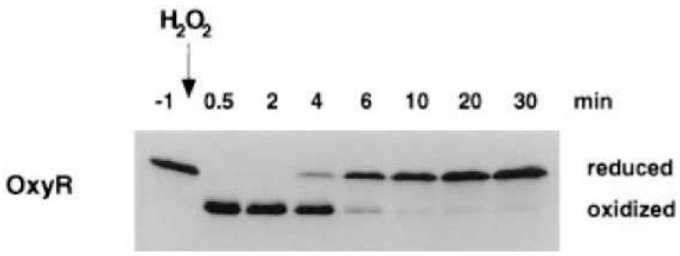

FIGURE 4.2: Extract from Aslund *et al.* [31]. OxyR activation and deactivation when *E. coli* was treated with 200 μM of H_2O_2 at $OD_{600} = 0.4$

The two chemical reactions of OxyR activation (oxidation) and deactivation (reduction) lead to the following differential equation:

$$\frac{\mathrm{d}\,[OxyR_{red}]}{\mathrm{d}t} = -k_{Ox}\,[H_2O_2]\,[OxyR_{red}] + k_{Red}\,[Red]\,([OxyR]_0 - [OxyR_{red}])$$

Where $[OxyR]_0$ is the total OxyR concentration in the cell. This equation was added to the ODE system in order to reproduce the Aslund *et al.* experiments. At steady state $OxyR_{red}$ ratio is:

$$\frac{[OxyR_{red}]}{[OxyR]_0} = \frac{1}{1 + \frac{k_{Ox}[H_2O_2]}{k_{Red}[Red]}}$$

OxyR is normally inactive during routine aerobiosis. However, González-Flecha and Demple [33] revealed that a intramolecular H_2O_2 concentration ranged from 130 to 250 nM points to the existence of regulatory systems that maintain the normal intracellular H_2O_2 level near 21 nM. Indeed the OxyR response is activated by micromolar levels of external H_2O_2 and according to the previous chapter [10] 1 μM of external H_2O_2 corresponds to nearly 130 nM of internal H_2O_2. Therefore an intracellular H_2O_2 concentration of approximately 130-250 nM is sufficient to drive OxyR into its active form (oxidized) that actively promotes the transcription of a dozen operons around the bacterial chromosome [34].

In order to run our numerical simulation we propose the following constants close to the one approximately proposed by Aslund *et al.* [31]:

$$k_{Ox} = 1 \times 10^5 \text{ M}^{-1}\text{s}^{-1};\ k_{red}\,[Red] = 0.1 \text{ s}^{-1};\ [OxyR]_0 = 0.7\,\mu\text{M (1300 copies)}$$

k_{Ox} value is also consistent with Lee *et al.*s' measurements [35]. We also reproduce Aslund *et al.*s' experiments looking for *in vivo* minimum concentrations of H_2O_2 required to oxidized OxyR. We also found that the lowest concentration of exogenously added H_2O_2 able to oxidize 50 % of OxyR within 30 sec is near 5 μM (this external concentration corresponds to 750 nM of initial internal H_2O_2). We can compare our simulation (Figure 4.3) with the results of Aslund *et al.* and Tao [36] (Figure 4.4). According to Tao [36] who reproduced Aslund *et al.*, nearly all the OxyR is found to be in the oxidized form after 40 μM of external H_2O_2 (this external H_2O_2 concentration corresponds to nearly 15 μM of an internal H_2O_2 concentration).

Using our kinetic constants, we also calculated:

- $\frac{[OxyR_{red}]}{[OxyR]_0} \approx 98\%$ when $[H_2O_2] = 21$ nM (internal H_2O_2 physiological concentration).

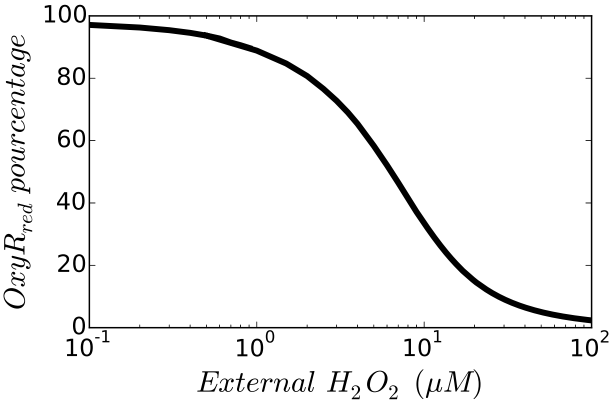

FIGURE 4.3: Simulation of OxyR (reduced form) *in vivo* activation following exposure to increasing concentrations of H_2O_2

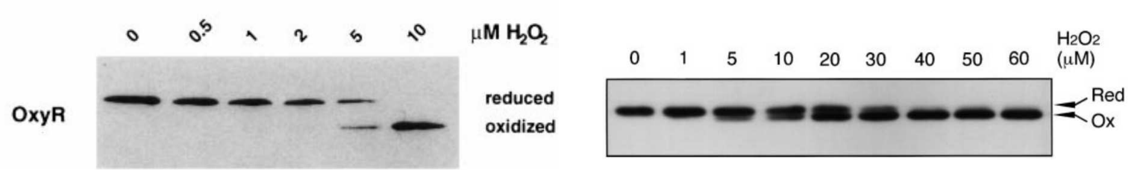

FIGURE 4.4: Extract from Aslund *et al.* [31] (left panel) and Tao [36] (right panel). OxyR activation and deactivation when *E. coli* was treated with increasing concentrations of external H_2O_2

- $\frac{[OxyR_{red}]}{[OxyR]_0} \approx 88\%$ when $[H_2O_2] = 130$ nM (internal H_2O_2 minimal activation concentration corresponding to 1 μM of external H_2O_2 concentration)
- $\frac{[OxyR_{red}]}{[OxyR]_0} \approx 57\%$ when $[H_2O_2] = 750$ nM (internal H_2O_2 concentration needed to oxidize nearly half of oxyR, it corresponds to 5 μM of external H_2O_2 concentration)
- $\frac{[OxyR_{red}]}{[OxyR]_0} \approx 6\%$ when external $[H_2O_2] = 40\,\mu$M (external H_2O_2 concentration needed for a complete OxyR oxidation according to Tao)

These values obtained with our model are consistent with the experimental data. Under physiological conditions OxyR principally remains in its reduced form, and its activation triggers near 200 nM of intracellular H_2O_2. According to those values, numerical simulations will start with a total amount of 1300 molecules of OxyR divided into 1273 (98 %) reduced molecules and 27 oxidized forms. OxyR response started to be activated beyond 12 % of oxidation which corresponds to 156 oxidized molecules (greater than the 27 initial oxidized forms). The next section will show that even stochastic effects could not trigger OxyR response because OxyR oxidized forms distribution is not large enough.

4.3.2 Stochastic results

According to the kinetic constants used in the previous section, we implemented a stochastic simulation lasting 200 seconds. This time is short enough to neglect biological induction (for instance DNA repair) and long enough to reach a chemical steady-state comportment for cell molecules. Indeed chemical characteristic times are lower than 1 ms because of kinetic rate constant high value.

Superoxide distribution

The figures 4.5 and 4.6 show $O_2^{\bullet -}$ homogeneous distribution around an average value of 0.366 molecule (consistent with deterministic calculation obtained after 200 s). The figure 4.7 indicates the maximum number of $O_2^{\bullet -}$ molecules observed in a cell, it shows that cells sometimes have to fight between 6 to 10 $O_2^{\bullet -}$ molecules which represent 20 to 30 times the average value. If most cells experience 0 or 1 $O_2^{\bullet -}$ at a given time, they can however fight a bigger account in a short period. Nevertheless, the average number of $O_2^{\bullet -}$ is evenly distributed on all cells according to the figures 4.6 and 4.8. We can also notice (figure 4.9) that the total amount of $O_2^{\bullet -}$ experiences by cell is homogeneously distributed between 2.046 and 2.058 million (during 200 s of simulation) of oxidative molecules which represent a very narrow range. Of course, this high value is consistent with the deterministic expression $k_1 t V_{in} \mathcal{N}_A \approx 2.052$ millions (where $\mathcal{N}_A \approx 6 10^{23}$ $\text{mol}^{-1}$is the Avogadro constant). Those observations let us think that significant fluctuations are not hazardous to cell and that cell evolution seems to be more sensitive to the global oxidative impact.

By comparing the concentrations of $O_2^{\bullet -}$ found in cells without oxidative stress with the concentrations necessary to disrupt cell functions, Imlay and Fridovich [37] show that 15 μM paraquat decrease 10-fold the growth rate of *E. coli*. They also indicated

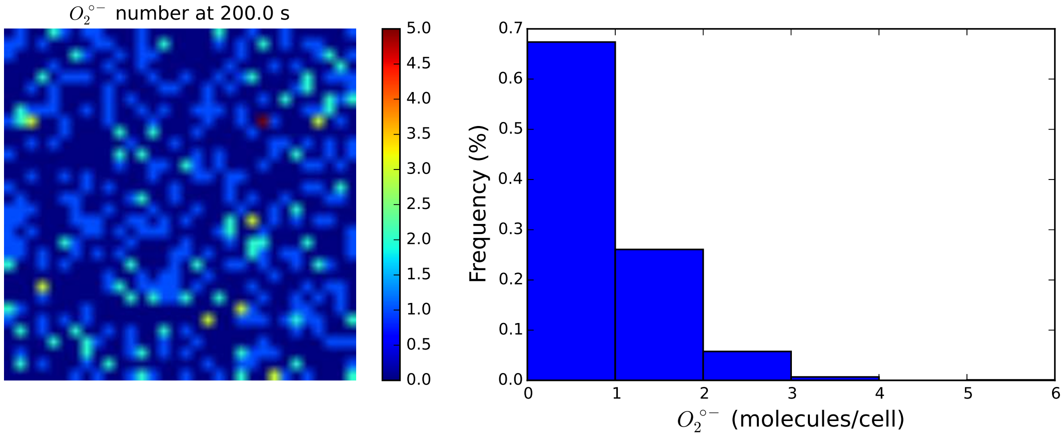

FIGURE 4.5: Superoxide number in each cell represented in a square lattice of 32 by 32 cells (left panel) and Superoxide distribution histogram (right panel). $O_2^{\bullet -}$ number is given after 200 seconds of the stochastic simulation.

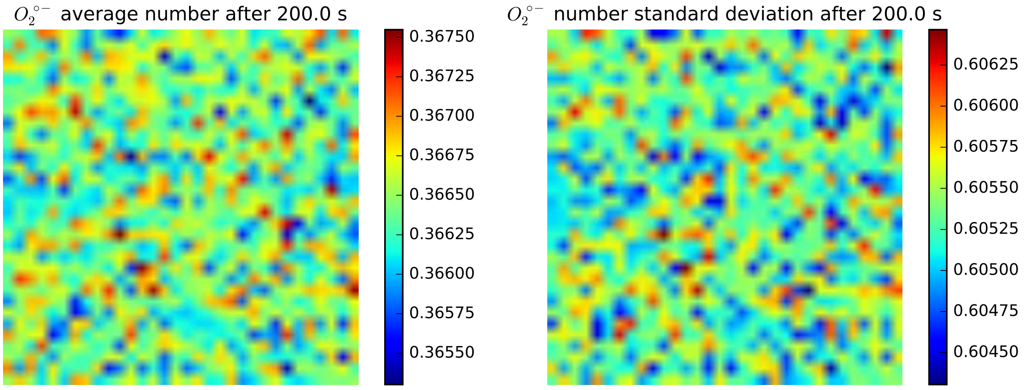

FIGURE 4.6: Superoxide average number in each cell represented in a square lattice of 32 by 32 cells (left panel) and the corresponding standard deviation. $O_2^{\bullet -}$ average value and standard deviation have been calculated after 200 seconds of the stochastic simulation.

that 15 μM paraquat should raise the steady-state $O_2^{\bullet -}$ concentration to 4 nM which represents an average value of nearly 7 molecules of $O_2^{\bullet -}$ per cell. According to our simulation (figure 4.7) nearly all cells met more than 7 molecules of $O_2^{\bullet -}$ as maximum number whereas the average value is only 0.37. This result confirms the idea that cell are sensitive to the average number and cumulative damage caused by $O_2^{\bullet -}$ and not by the maximal number. Figure (4.10) shows the fate of one cell that indeed met a maximum number of $O_2^{\bullet -}$ equal to 7 in a tiny time interval; we noticed that this evolution looks like a Dirac comb therefore it confirms that the maximum number does not have

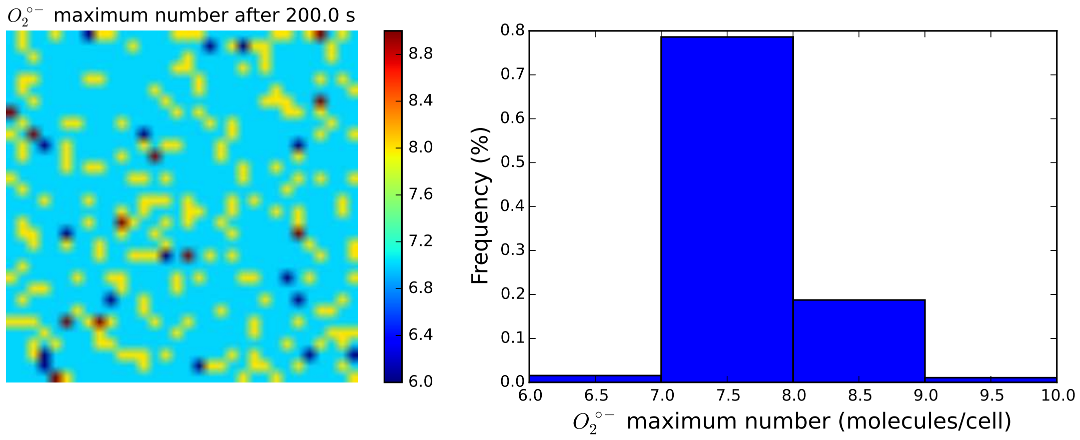

FIGURE 4.7: Superoxide maximal number in each cell represented in a square lattice of 32 by 32 cells (left panel) and Superoxide maximal number distribution histogram (right panel). $O_2^{\bullet -}$ maximal number is calculated after 200 seconds of the stochastic simulation.

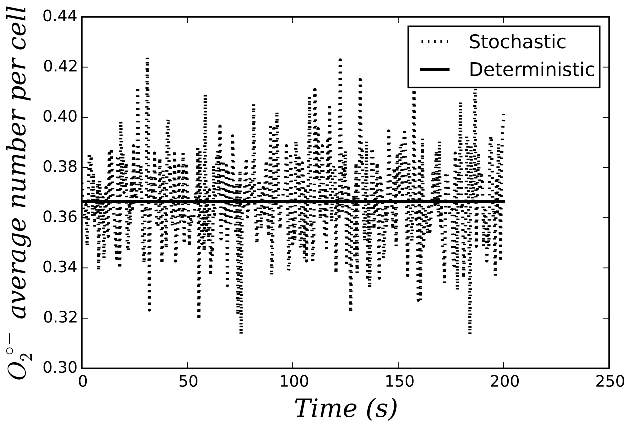

FIGURE 4.8: Superoxide average number in cell versus time for a system of 1032 cells. $O_2^{\bullet -}$ average value has been calculated during 200 seconds of the stochastic simulation.

a real influence. This result agrees with the one we developed with H_2O_2 [10].

Moreover Imlay and Fridovich [37] estimated that 100 μM of paraquat should raise the steady-state $O_2^{\bullet -}$ concentration to 27 nM which represents nearly 48 molecules of $O_2^{\bullet -}$ per cell which is 100-fold more than the average number of $O_2^{\bullet -}$ without oxidative stress and even 5-fold more than the maximum number (Figure 4.7) observed in our simulations. Hassan and Fridovich [38] indicated that 100 μM of paraquat only doubles the amount of SOD. Actually SOD efficiency (because of a very high turn over) is so important that it does not need a large number of copies.

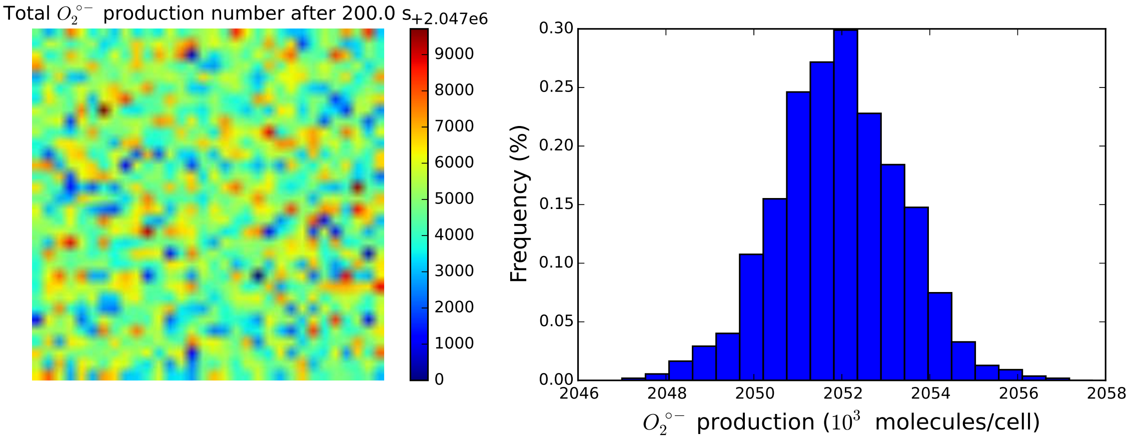

FIGURE 4.9: Superoxide total number produced in each cell represented in a square lattice of 32 by 32 cells (left panel) and Superoxide total number produced distribution histogram (right panel). $O_2^{\bullet-}$ total number is calculated after 200 seconds of the stochastic simulation.

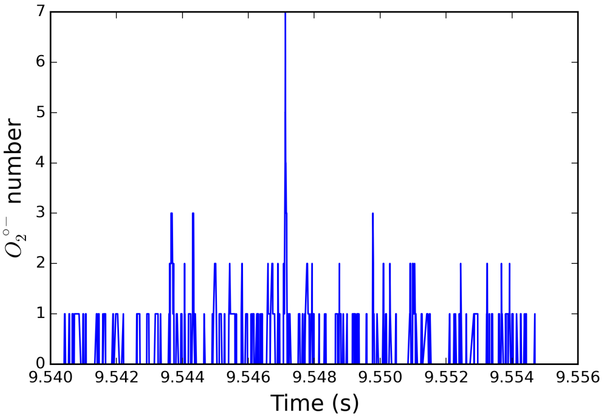

FIGURE 4.10: Superoxide number evolution in one cell during a narrow time interval. $O_2^{\bullet-}$ number is calculated using the stochastic simulation following the NSM method.

Ding and Demple [14] reported that SoxR [2Fe–2S] clusters were completely oxidized after only 2-min aerobic exposure of the cells to superoxide-generating agents using 100 μM paraquat. Then $soxS$ transcript reached a steady state within 10 min (and a half life near 5 min) of aerobic exposure to 100 μM of paraquat. This 5 min half life strongly depends on the paraquat concentration as reported by Lu *et al.* [39], therefore if 100 μM of paraquat corresponds to a steady state of 48 $O_2^{\bullet-}$ molecules with a 5 min half life, a steady state of 0.38 molecule of $O_2^{\bullet -}$ should give a half life long enough to neglect soxRS response.

Hydrogen peroxide distribution

H_2O_2 molecules follow different ranges and kinds of distribution comparing number, maximal number or total production of molecule. Indeed, figure 4.13 indicates that the maximum number of H_2O_2 molecules observed in a cell ranges between 68 and 84 molecules which is approximately twice the average value close to 38 (figure 4.12 and 4.14) or four times the minimum value observed in figure 4.11 after 200 s. Nevertheless, the standard deviation is only about 6 molecules. These results are consistent with the deterministic prediction. However, we can also notice (figure 4.15) that the total amount of H_2O_2 experiences per cell is distributed between 5.336 and 5.354 billions of H_2O_2 molecules which represent a very narrow range. Therefore, all cells suffer the same cumulative amount of H_2O_2 with some short time interval of insignificant oxidative fluctuation.

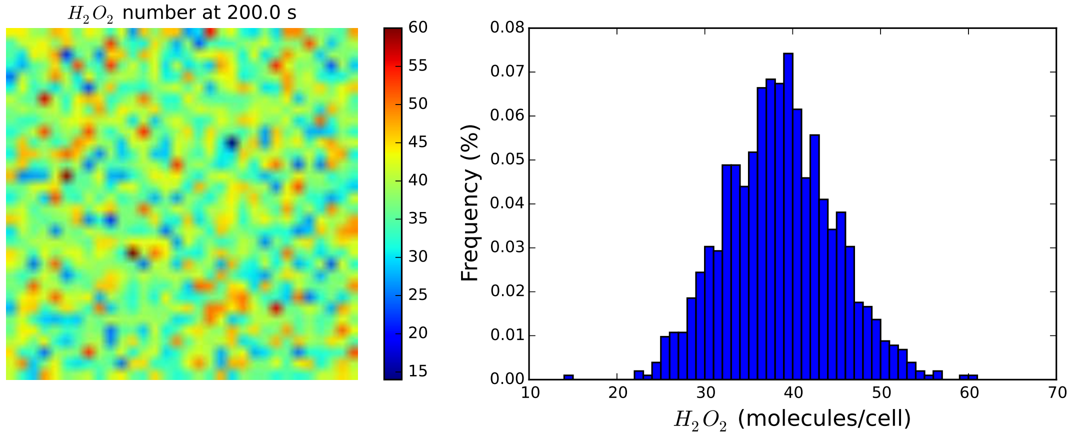

FIGURE 4.11: Hydrogen peroxide number in each cell represented in a square lattice of 32 by 32 cells (left panel) and Hydrogen peroxide distribution histogram (right panel). H_2O_2 number is given after 200 seconds of the stochastic simulation following the NSM method.

OxyR distribution

OxyR oxidized molecules follow a narrow range distribution centred around 27 ± 7 molecules with a standard deviation near 5 ± 3 molecules (figures 4.16 and 4.17). This

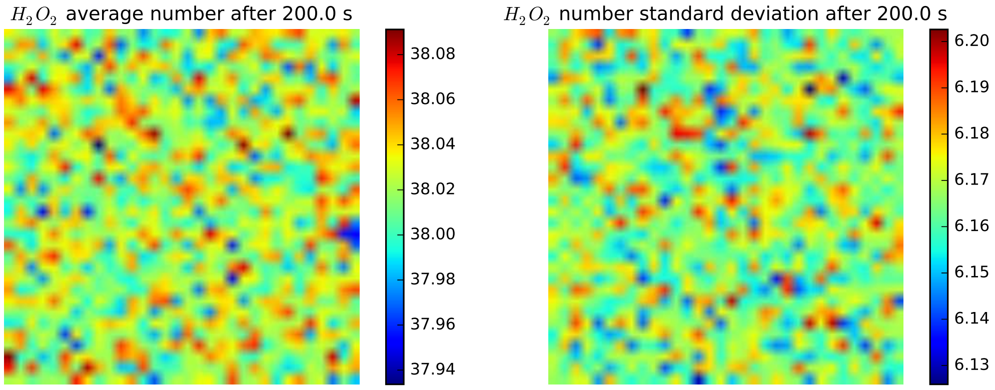

FIGURE 4.12: Hydrogen peroxide average number in each cell represented in a square lattice of 32 by 32 cells (left panel) and the corresponding standard deviation. H_2O_2 average value and standard deviation have been calculated after 200 seconds of the stochastic simulation following the NSM method.

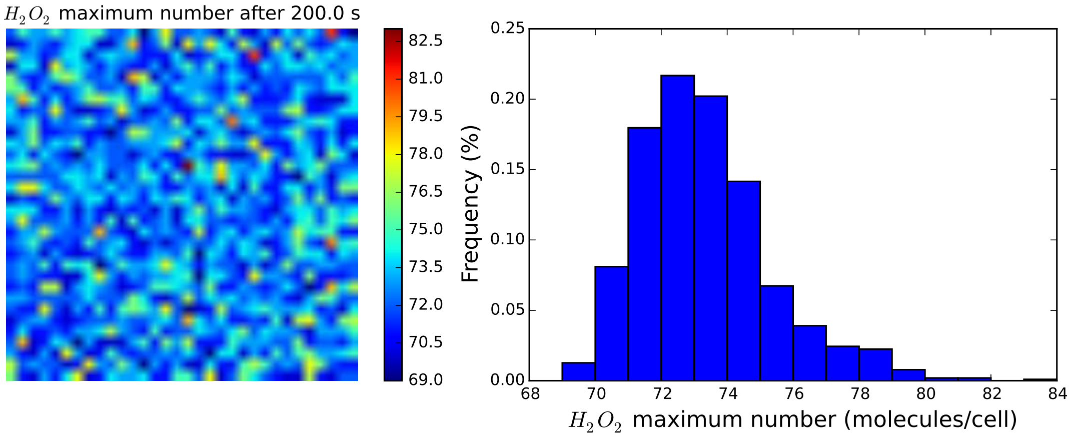

FIGURE 4.13: Hydrogen peroxide number in each cell represented in a square lattice of 32 by 32 cells (left panel) and Hydrogen peroxide distribution histogram (right panel). H_2O_2 number is given after 200 seconds of the stochastic simulation following the NSM method.

average value is approximately constant in time (figure 4.19) and even the maximum number of molecules does not deviate too far (figure 4.18) and does not exceed twice the initial value (maximum is 54 and average value of the maximal OxyR activated form is 38). Unlike $O_2^{\bullet-}$ and H_2O_2 which have a small number of copies, OxyR (oxidized) molecules present a large number of copies which reduces the effect of stochasticity.

Moreover the correlation coefficient between maximum oxidized OxyR molecules

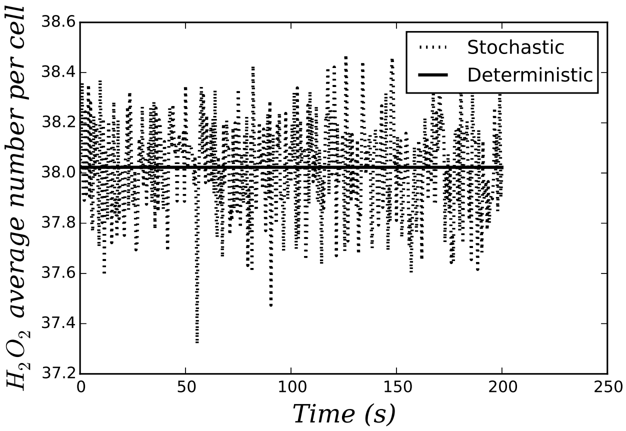

FIGURE 4.14: Hydrogen peroxide average number in cell versus time calculated for a system of 1032 cells. H_2O_2 average value has been calculated during 200 seconds of the stochastic simulation following the NSM method.

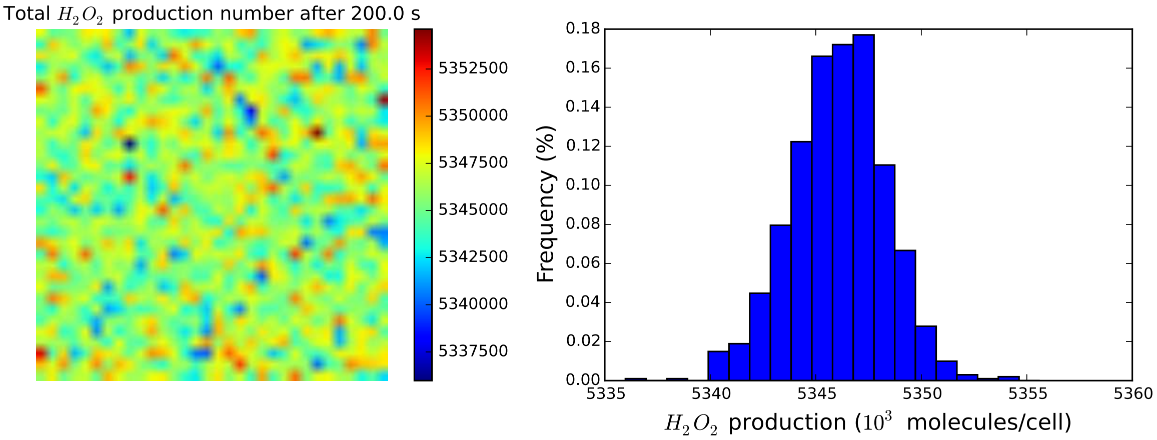

FIGURE 4.15: Hydrogen peroxide total number produced in each cell represented in a square lattice of 32 by 32 cells (left panel) and Hydrogen peroxide total number produced distribution histogram (right panel). H_2O_2 total number is calculated after 200 seconds of the stochastic simulation following the NSM method.

number and maximum H_2O_2 molecule number is (over all simulations) lower than 5 %. Figure 4.20 shows a scatter plot example where the correlation coefficient is only 0.7 %, this figure contains no ambiguity concerning the independence of the two variables.

We conclude that the data pairs are not correlated at physiological concentration. Cells with a maximum number of oxidized OxyR are not automatically those with the maximum number of H_2O_2. Of course this assertion should change at non-physiological H_2O_2 concentrations. Simulations show a maximum number of H_2O_2 molecules near

85, this value is below a concentration of 50 nM which is also below the 130 nM the minimal internal H_2O_2 concentration required for OxyR activation [40, 41].

Finally, after testing multiple statistical laws for $OxyR_{ox}$ distribution we find that the probability that $OxyR_{ox}$ exceed 150 copies (minimum required for activation) is almost rigorously null. We conclude that under physiological conditions (and with the hypothesis used in our model) no cell activates OxyR. Indeed the maximal oxidized OxyR proportion hardly reaches 5 % which is insufficient.

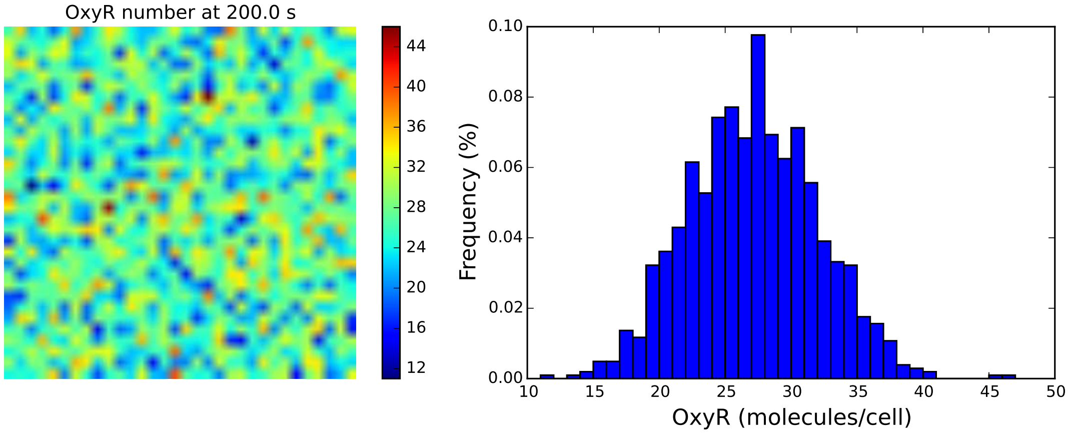

FIGURE 4.16: OxyR number in each cell represented in a square lattice of 32 by 32 cells (left panel) and OxyR distribution histogram (right panel). OxyR number is given after 200 seconds of the stochastic simulation following the NSM method.

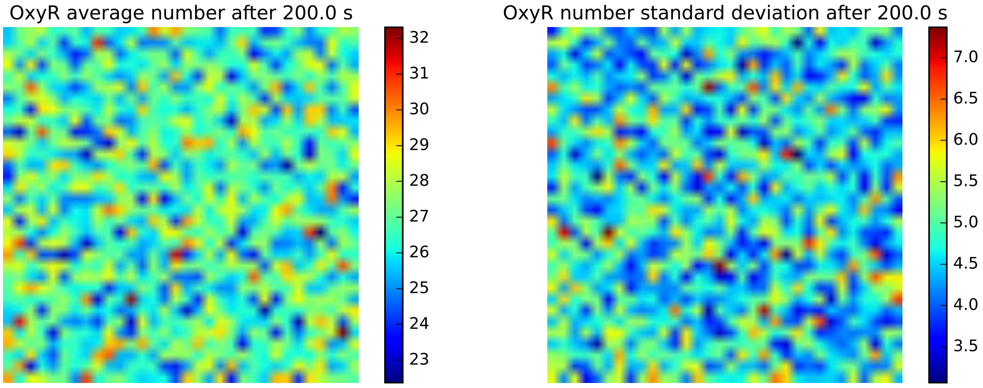

FIGURE 4.17: OxyR average number in each cell represented in a square lattice of 32 by 32 cells (left panel) and the corresponding standard deviation. OxyR average value and standard deviation have been calculated after 200 seconds of the stochastic simulation following the NSM method.

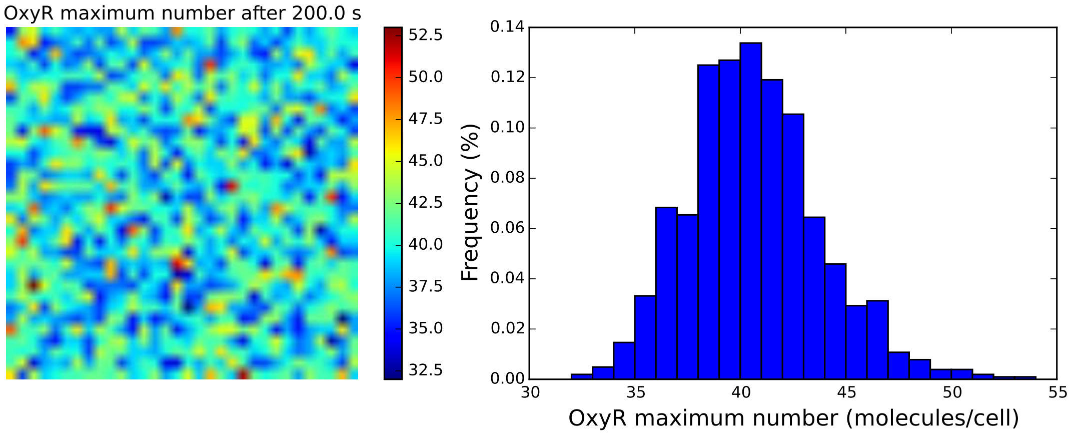

FIGURE 4.18: OxyR maximal number in each cell represented in a square lattice of 32 by 32 cells (left panel) and maximal OxyR distribution histogram (right panel). OxyR number is given after 200 seconds of the stochastic simulation following the NSM method.

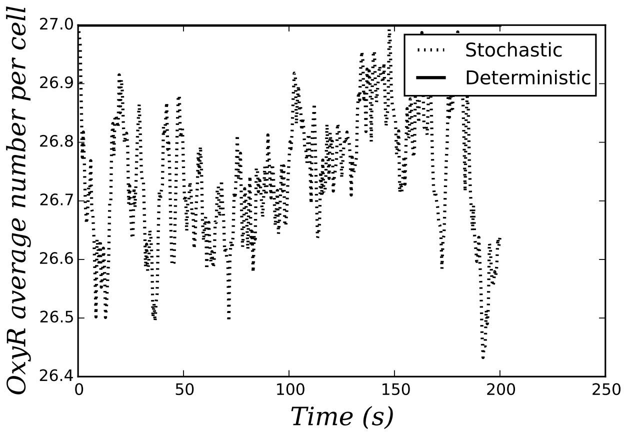

FIGURE 4.19: OxyR average number in cell versus time for a system of 1032 cells. OxyR average value was calculated during 200 seconds of the stochastic simulation following the NSM method.

DNA distribution

Numerical simulations do not consider DNA repair, therefore we only count DNA nicks by $HO^\bullet$ and observed their distributions over the 1032 cell set over the 32 by 32 square lattice. One example of simulation results is shown in figure 4.21. The DNA damage distribution follows a Poisson distribution with parameter $\lambda = 2,1$ (average number of DNA damage). We use the Kolmogorov-Smirnov statistic on 2 samples [42]. This is a two-sided test for the null hypothesis that 2 independent samples are drawn from the same continuous distribution. Over all simulations, the K-S statistic is about 1

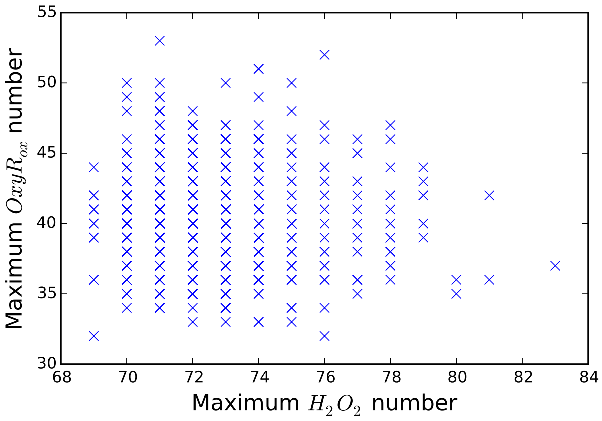

FIGURE 4.20: Scatter plot of $OxyR_{ox}$ maximal number in cell versus H_2O_2 maximal number for a system of 1032 cells. Values have been calculated during 200 seconds of the stochastic simulation following the NSM method.

% (small enough) and the p-value is about 99 % (high enough), so we cannot reject the hypothesis that the distributions of the two samples are the same. The Poisson distribution is often called the law of small numbers because it corresponds to the probability distribution of the number of occurrences of an event that happens rarely but has very many chances of happening. This distribution seems to fit DNA damage distribution perfectly.

Moreover the correlation coefficient between maximum H_2O_2 molecules number and DNA damage number is lower than 3 %. It indicates that the data pairs are not correlated at physiological concentration. Cells with maximum number of DNA lesions are not necessarily those with the maximum number of H_2O_2.

So, under physiological conditions, DNA damage distribution is only due to the inherent stochastic mechanism of chemical reactions. According to the simulation, we can notice that during 200 s, about 65 % of cells suffer less than 2 lesions whereas one unlucky cell has to fight 8 lesions (four times the average value). This unlucky cell has an average number of H_2O_2 of 38 with a maximum value of 75, once again there is no correlation between the H_2O_2 molecules number and DNA damage. Indeed, following the Poisson distribution, we can check that the probability for a cell to get $k = 8$ DNA lesions is $P(k = 8) = \frac{\lambda^k}{k!}e^{-\lambda} \approx \frac{1}{870}$. This means that taking 870 cells we will get one cell with 8 types of damage (on average). We can also notice that about 13 % of cells show no damage. So because damage rarely happen, it involves a large distribution which highly segregates cells. And this is only a consequence of chemical properties, here we do not take into account biological induction.

Here we implemented the simulation with 1032 cells, but with the same reasoning and according to Poisson distribution, we can say that taking 10^9 cells we will find one cell with 16 type of damage (on average). This value is 8 times the mean value whereas the H_2O_2 average number still remains on 38 molecules. This is an extraordinary high value, in order to reach this number of types of damage as an average value H_2O_2 intracellular should be at least 8 times. Indeed, average DNA lesions are proportional to average $[HO^\bullet]$ which is proportional to average $[H_2O_2]$. Under physiological conditions $[H_2O_2]$ is about 21 nM. So in order to observe an average value of 16 DNA lesions, intracellular $[H_2O_2]$ should rise to about 170 nM. Moreover because of the flux gradient between external medium and intracellular medium, 170 nM of intracellular $[H_2O_2]$ corresponds to approximately 1.5 μM of external H_2O_2 [10]. At those concentrations, defence mechanisms must be on the alert and OxyR must be activated. Nevertheless, the unlucky cell which has suffered the 16 DNA lesions under physiological conditions has not activated OxyR (because H_2O_2 concentration is too low) but it will probably trigger the regulation of DNA-repair (after an induction delay), and this cell will then be ready to respond to adverse environmental conditions. So what we thought to be misfortune can turn out to be an advantage over other conditions. Therefore chemical stochasticity can explain the robustness of some cells or the deployment of specialized cells. This is an example of rare event concerning a single molecule that involves important biological consequences.

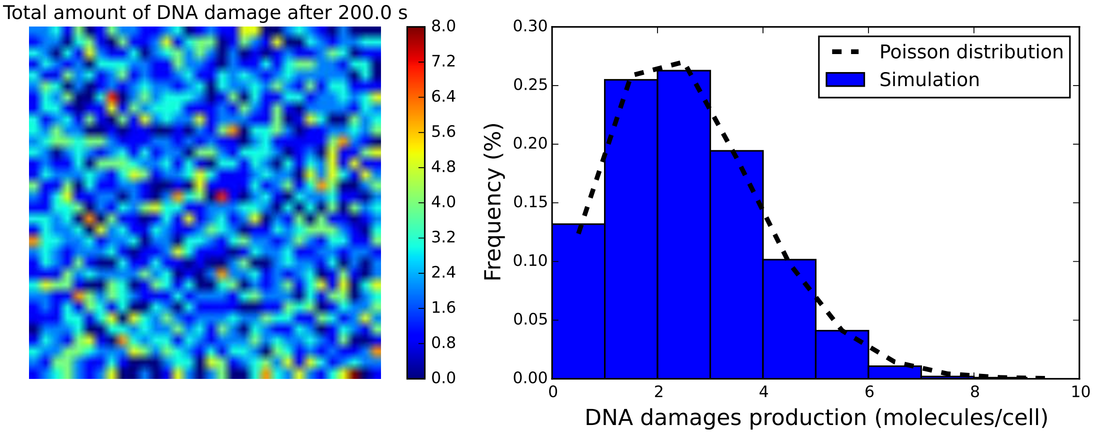

FIGURE 4.21: DNA types of damage number in each cell represented in a square lattice of 32 by 32 cells (left panel) and DNA damage distribution histogram with the theoretical Poisson distribution in dashed line style (right panel). DNA damage number is given after 200 seconds according to our stochastic simulation following the NSM method.

Bibliography

[1] S. Arrhenius, Uber die Dissociations arme und den Einfluss der Temperatur. Wilhelm Engelmann, 1889.

[2] H. Eyring, "The activated complex in chemical reactions", The Journal of Chemical Physics, vol. 3, no. 2, pp. 107–115, 1935.

[3] J. Imlay and I. Fridovich, "Assay of metabolic superoxide production in escherichia coli.", Journal of Biological Chemistry, vol. 266, no. 11, pp. 6957–6965, 1991.

[4] R. Losick and C. Desplan, "Stochasticity and cell fate", Science, vol. 320, no. 5872, pp. 65–68, 2008.

[5] G.-W. Li and X. S. Xie, "Central dogma at the single-molecule level in living cells", Nature, vol. 475, no. 7356, pp. 308–315, 2011.

[6] N. G. Van Kampen, Stochastic processes in physics and chemistry. Elsevier, 1992, vol. 1.

[7] E. Hidalgo and B. Demple, "Adaptive responses to oxidative stress: The soxrs and oxyr regulons", in Regulation of gene expression in Escherichia coli, Springer, 1996, pp. 435–452.

[8] G. Storz and J. A. Imlay, "Oxidative stress", Current opinion in microbiology, vol. 2, no. 2, pp. 188–194, 1999.

[9] L. Uhl, A. Gerstel, M. Chabalier, and S. Dukan, "Hydrogen peroxide induced cell death: One or two modes of action?", Heliyon, vol. 1, no. 4, e00049, 2015.

[10] L. Uhl and S. Dukan, "Hydrogen peroxide induced cell death: The major defences relative roles and consequences in e. coli", Plos One, vol. 11, no. 8, e0159706, 2016.

[11] L. C. Seaver and J. A. Imlay, "Hydrogen peroxide fluxes and compartmentalization inside growing escherichia coli", Journal of bacteriology, vol. 183, no. 24, pp. 7182–7189, 2001.

[12] ——, "Alkyl hydroperoxide reductase is the primary scavenger of endogenous hydrogen peroxide in escherichia coli", Journal of bacteriology, vol. 183, no. 24, pp. 7173–7181, 2001.

[13] I. R. Tsaneva and B. Weiss, "Soxr, a locus governing a superoxide response regulon in escherichia coli k-12.", Journal of bacteriology, vol. 172, no. 8, pp. 4197–205, Aug. 1990.

[14] H. Ding and B. Demple, "In vivo kinetics of a redox-regulated transcriptional switch.", Proceedings of the National Academy of Sciences of the U.S.A., vol. 94, no. 16, pp. 8445–9, Aug. 1997.

[15] J. W. Little and M. Gellert, "The sos regulatory system: Control of its state by the level of reca protease", Journal of molecular biology, vol. 167, no. 4, pp. 791–808, 1983.

[16] M. Sassanfar and J. W. Roberts, "Nature of the sos-inducing signal in escherichia coli. the involvement of dna replication.", Journal of molecular biology, vol. 212, no. 1, pp. 79–96, Mar. 1990.

[17] S. L. Lusetti and M. M. Cox, "The bacterial reca protein and the recombinational dna repair of stalled replication forks.", Annual review of biochemistry, vol. 71, pp. 71–100, 2002.

[18] M. M. Cox, "Regulation of bacterial reca protein function", Critical reviews in biochemistry and molecular biology, vol. 42, no. 1, pp. 41–63, 2007.

[19] O. Goerlich, P. Quillardet, and M. Hofnung, "Induction of the sos response by hydrogen peroxide in various escherichia coli mutants with altered protection against oxidative dna damage.", Journal of bacteriology, vol. 171, no. 11, pp. 6141–6147, 1989.

[20] N. Friedman, S. Vardi, M. Ronen, U. Alon, and J. Stavans, "Precise temporal modulation in the response of the sos dna repair network in individual bacteria", PLoS biol, vol. 3, no. 7, e238, 2005.

[21] D. T. Gillespie, "A general method for numerically simulating the stochastic time evolution of coupled chemical reactions", Journal of computational physics, vol. 22, no. 4, pp. 403–434, 1976.

[22] ——, "Exact stochastic simulation of coupled chemical reactions", The journal of physical chemistry, vol. 81, no. 25, pp. 2340–2361, 1977.

[23] J. Elf, A. Doncic, and M. Ehrenberg, "Mesoscopic reaction-diffusion in intracellular signaling", in SPIE's First International Symposium on fluctuations and noise, International Society for Optics and Photonics, 2003, pp. 114–124.

[24] J. Elf and M. Ehrenberg, "Spontaneous separation of bi-stable biochemical systems into spatial domains of opposite phases", IEE Proceedings-Systems Biology, vol. 1, no. 2, pp. 230–236, 2004.

[25] G. van Rossum, "Python tutorial", Report CS-R9526, Apr. 1995, pp. iii + 65.

[26] P. F. Hallin and D. W. Ussery, "Cbs genome atlas database: A dynamic storage for bioinformatic results and sequence data", Bioinformatics, vol. 20, no. 18, pp. 3682–3686, 2004.

[27] H. B. Michaels and J. Hunt, "Reactions of the hydroxyl radical with polynucleotides", Radiation Research, vol. 56, no. 1, pp. 57–70, 1973.

[28] B. D. Bennett, E. H. Kimball, M. Gao, R. Osterhout, S. J. Van Dien, and J. D. Rabinowitz, "Absolute metabolite concentrations and implied enzyme active site occupancy in escherichia coli", Nature chemical biology, vol. 5, no. 8, pp. 593–599, 2009.

[29] E.-M. Park, M. K. Shigenaga, P. Degan, T. S. Korn, J. W. Kitzler, C. M. Wehr, P. Kolachana, and B. N. Ames, "Assay of excised oxidative dna lesions: Isolation of

8-oxoguanine and its nucleoside derivatives from biological fluids with a monoclonal antibody column.", Proceedings of the National Academy of Sciences, vol. 89, no. 8, pp. 3375–3379, 1992.

[30] M. Zheng, F. Åslund, and G. Storz, "Activation of the oxyr transcription factor by reversible disulfide bond formation", Science, vol. 279, no. 5357, pp. 1718–1722, 1998.

[31] F. Åslund, M. Zheng, J. Beckwith, and G. Storz, "Regulation of the oxyr transcription factor by hydrogen peroxide and the cellular thiol—disulfide status", Proceedings of the National Academy of Sciences, vol. 96, no. 11, pp. 6161–6165, 1999.

[32] G.-W. Li, D. Burkhardt, C. Gross, and J. S. Weissman, "Quantifying absolute protein synthesis rates reveals principles underlying allocation of cellular resources", Cell, vol. 157, no. 3, pp. 624–635, 2014.

[33] B. González-Flecha and B. Demple, "Homeostatic regulation of intracellular hydrogen peroxide concentration in aerobically growing escherichia coli.", Journal of bacteriology, vol. 179, no. 2, pp. 382–8, Jan. 1997.

[34] J. A. Imlay, "The molecular mechanisms and physiological consequences of oxidative stress: Lessons from a model bacterium", Nature Reviews Microbiology, vol. 11, no. 7, pp. 443–454, 2013.

[35] C. Lee, S. M. Lee, P. Mukhopadhyay, S. J. Kim, S. C. Lee, W.-S. Ahn, M.-H. Yu, G. Storz, and S. E. Ryu, "Redox regulation of oxyr requires specific disulfide bond formation involving a rapid kinetic reaction path", Nature structural & molecular biology, vol. 11, no. 12, pp. 1179–1185, 2004.

[36] K. Tao, "In vivo oxidation-reduction kinetics of OxyR, the transcriptional activator for an oxidative stress-inducible regulon in Escherichia coli", FEBS Lett., vol. 457, no. 1, pp. 90–92, Aug. 1999.

[37] K. J. Davies, Oxidative damage & repair: Chemical, biological and medical aspects. Elsevier, 2013.

[38] H. M. Hassan and I. Fridovich, “Paraquat and escherichia coli. mechanism of production of extracellular superoxide radical.”, Journal of Biological Chemistry, vol. 254, no. 21, pp. 10 846–10 852, 1979.

[39] C. Lu, C. R. Albano, W. E. Bentley, and G. Rao, “Quantitative and kinetic study of oxidative stress regulons using green fluorescent protein.”, Biotechnology and bioengineering, vol. 89, no. 5, pp. 574–87, Mar. 2005.

[40] S. Park, X. You, and J. A. Imlay, “Substantial dna damage from submicromolar intracellular hydrogen peroxide detected in hpx-mutants of escherichia coli”, Proceedings of the National Academy of Sciences of the United States of America, vol. 102, no. 26, pp. 9317–9322, 2005.

[41] S. Jang and J. A. Imlay, “Micromolar intracellular hydrogen peroxide disrupts metabolism by damaging iron-sulfur enzymes”, Journal of Biological Chemistry, vol. 282, no. 2, pp. 929–937, 2007.

[42] F. J. Massey Jr, “The kolmogorov-smirnov test for goodness of fit”, Journal of the American statistical Association, vol. 46, no. 253, pp. 68–78, 1951.

Chapter 5

Conclusions and perspectives

This thesis presents multiple aspects of ROS dynamic with both analytical or theoretical demonstrations and deterministic or stochastic numerical simulations. We have shown that our models can be used to interpret or even predict some experimental results. Let us come back to the main results presented in this thesis.

Our work first deals with Imlay and Linn [1] two modes of *Escherichia coli* cell killing experiments. A simple model demonstrates (mathematically and numerically) that free available iron decrease is necessary to explain *in vitro* or *in vivo* mode one killing which cannot appear without it and that H_2O_2 quenching or consumption is not responsible for mode-one death. Moreover using our model, we were also able to demonstrate that cell density is strongly involved in $HO^\bullet$ dynamic and by consequence in DNA oxidation within *E. coli*. Indeed, without taking into account the evolution of free available iron or cell density, we were not able to reproduce mode one killing experimental results obtained in the literature.

In order to evaluate the major defences relative roles against H_2O_2, we investigated the relative contributions of the various reactions to the dynamic system and searched for approximate analytical solutions for the explicit expression of changes in H_2O_2 internal or external concentrations. Although the key actors in cell defence are enzymes and membrane, a detailed analysis shows that their involvement depends on the H_2O_2 concentration level. Actually, the impact of the membrane upon the H_2O_2 stress felt by the cell is greater when micromolar H_2O_2 is present (9-fold less H_2O_2 in the cell than out of the cell) than when millimolar H_2O_2 is present (about 2-fold less H_2O_2 in the cell than out of the cell). The ratio between maximal external H_2O_2 and internal H_2O_2 concentration also changes, reducing from 8 to 2 while external H_2O_2 concentration increases from micromolar to millimolar. This non-linear behaviour mainly occurs because of the switch in the predominant scavenger from Ahp (Alkyl Hydroperoxide Reductase) to Cat (catalase). The phenomenon changes the internal H_2O_2 maximal concentration, which surprisingly does not depend on cell density. The external H_2O_2 half-life and the cumulative internal H_2O_2 exposure do depend upon cell density. Based on these analyses and in order to introduce a concept of dose response relationship for H_2O_2-induced cell death, we developed the concepts of "maximal internal H_2O_2 concentration" and "cumulative internal H_2O_2 concentration" (e.g. the total amount of H_2O_2). We predict that cumulative internal H_2O_2 concentration is responsible for the H_2O_2-mediated death of bacterial cells. This study also allows us to better interpret Ma and Eaton's [2] experiments which consider different *E. coli* mutants and cell densities.

It has also recently been suggested that the carbonate radical ($CO_3^{\bullet-}$), generated by a reaction between $HO^{\bullet}$ and carbon dioxide CO_2, are formed in *E. coli* [3], increasing the known range of ROS.

$$HO^{\bullet} + CO_2 \rightarrow H^{+} + CO_3^{\bullet-}$$

However, no direct proof has yet been obtained for the existence of this new ROS *in vivo*. Indeed, the methods used to study short-lived species, such as the spin trapping of radicals, cannot easily differentiate between $HO^{\bullet}$ [4]. Ezraty [5] showed that increases in atmospheric CO_2 concentrations are associated with an increase in DNA damage estimated by 8-oxo-guanine levels. Our team (Audrey Gerstel unpublished data) also measured p-nitrosodimethylaniline (pNDA) oxidation via a Fenton system ($Fe(II)/H_2O_2 - 75\,\mu$M iron) experimentally, at two different concentrations of atmospheric CO_2 : 0 and 1000 ppm. We found that pNDA oxidation was dependent on CO_2 concentration. These two *in vitro* experiments show that, contrary to Ezraty *in* *vivo* results, increases in $CO_{2,aq}$ concentration lead to a decrease in Fenton oxidation efficiency. Therefore, we investigated whether the simulation of ROS/$CO_{2,aq}$ interactions *in vivo* could account for those experimental results. Our *in silico* experiments could partially explain some experimental results, but they are strongly dependent on the rate constants which are not well known. We have to deeper our model in order to avoid some contradictory results, then we hope to unify *in vitro, in vivo* and *in silico* observations.

Our team (Audrey Gerstel unpublished data) also reproduced mode one killing experiments with different *E. coli* mutants (for example OxyR null mutant), cell densities or CO_2 atmospheric various partial pressures (which involve various $CO_{2,aq}$ concentration according to Henry's Law). *In silico* experiments were able to reproduce experimental results but some missing data (for example *E. coli* $CO_{2(g)}$ production in LB) were invented to test our model. Experimental results show a high dependency upon CO_2, but to complete our mathematical model we first have to perform more *in vivo* experiments in order to obtain more rate constants or missing data.

The last chapter of the thesis looks closely at on the single cell, a micro-system where chemical reactions may proceed in a deterministic manner because only a few types of molecule exist in a cell, therefore stochastic effects can become predominant. We showed that elementary chemical stochasticity allows bacteria to segregate specialized cells in prevision of possible stress challenge. Actually, whereas ROS distribution does not activate defence regulation without exogenous stress, we demonstrated that this distribution may activate DNA repair mechanism because DNA damage shows a very large range distribution following a Poisson distribution which perfectly describes rare events. Moreover superoxide, hydrogen peroxide, OxyR and DNA damage distributions caused by hydroxyl radical are not statistically correlated. DNA damage distribution is only due to the fact that DNA nicks are the result of a succession of rare events which involve a small number of molecules. To complete this stochastic approach, we could improve the model by adding the SoxR transcription factors and eventually the SOS response, but this improvement will have to be tested over a longer period in order to be significant. Then simulations could be compared with SOD experimental distribution obtained by our team. Finally we could also imagine adding CO_2 interactions with ROS to examine its involvement in cell DNA bases damage.

Using biological, chemical, physical, mathematical or computational models, this interdisciplinary thesis can lead to a better understanding of the ROS dynamic but it also confirms to scientists the interest there is in blending together scientific fields.

Bibliography

[1] J. A. Imlay and S. Linn, "Bimodal pattern of killing of dna-repair-defective or anoxically grown escherichia coli by hydrogen peroxide.", Journal of bacteriology, vol. 166, no. 2, pp. 519–527, 1986.

[2] M. Ma and J. W. Eaton, "Multicellular oxidant defense in unicellular organisms", Proc. Natl. Acad. Sci. U.S.A., vol. 89, no. 17, pp. 7924–7928, Sep. 1992.

[3] O. Augusto, M. G. Bonini, A. M. Amanso, E. Linares, C. C. Santos, and S. L. De Menezes, "Nitrogen dioxide and carbonate radical anion: two emerging radicals in biology", Free Radic. Biol. Med., vol. 32, no. 9, pp. 841–859, May 2002.

[4] F. A. Villamena, E. J. Locigno, A. Rockenbauer, C. M. Hadad, and J. L. Zweier, "Theoretical and experimental studies of the spin trapping of inorganic radicals by 5,5-dimethyl-1-pyrroline N-oxide (DMPO).", J Phys Chem A, vol. 111, no. 2, pp. 384–391, Jan. 2007.

[5] B. Ezraty, M. Chabalier, A. Ducret, E. Maisonneuve, and S. Dukan, "CO2 exacerbates oxygen toxicity", EMBO Rep., vol. 12, no. 4, pp. 321–326, Apr. 2011.

Appendix A

Numerical methods for ODE

A.1 Runge-Kutta

A.1.1 ODE discretization

This part studies the following first order differential equation which is a Cauchy problem.

$$\begin{cases} \frac{\mathrm{d}v(t)}{\mathrm{d}t} = f\left(t, v(t)\right) \quad 0 \leq t \leq T \\ v(0) = v_0 \end{cases}$$

where $f : [0, T] \times \mathbb{R} \to \mathbb{R}$ is a continuous function and $v_0 \in \mathbb{R}$.

For the numerical approximation, h is the fixed step size of the uniform subdivision $(t_n)_{n \in [\![0,N]\!]}$ from the interval $[0, T]$: $t_n = nh$ and $\tilde{v}_n$ represents the numerical approximation of $v_n = v(t_n)$ for $0 \leq n \leq N$. The different methods exposed here are one-step methods because the determination of $\tilde{v}_{n+1}$ is made knowing the previous value $\tilde{v}_n$.

A.1.2 Runge-Kutta methods (*RK*)

Presentation

The general form of the Runge-Kutta methods is

$$\tilde{v}_{n+1} = \tilde{v}_n + h\Phi\left(t_n, \tilde{v}_n, h\right)$$

where Φ is called the *increment function*. It is defined by:

$$\Phi\left(t_n, \tilde{v}_n, h\right) = \sum_{i=1}^{s} b_i k_i \text{ with } \forall i \in [\![1, s]\!]\,,\ k_i = f\left(t_n + c_i h, \tilde{v}_n + h \sum_{j=1}^{s} a_{ij} k_j\right)$$

TABLE A.1: Butcher table for *RK* methods

$$
\begin{array}{c|cccc}
c_1 & a_{11} & a_{12} & \cdots & a_{1s} \\
c_2 & a_{21} & a_{22} & & a_{2s} \\
\vdots & \vdots & & \ddots & \vdots \\
c_s & a_{s1} & a_{s2} & \cdots & a_{ss} \\
\hline
 & b_1 & b_2 & \cdots & b_s
\end{array}
$$

s represents the method number of level.

The coefficients a_{ij}, b_i et c_i characterize completely one *RK* method. The following table outlines the choice of coefficients (Butcher table).

The Runge-Kutta methods are based on the increase in the number s of the function evaluation in order to ameliorate the accuracy of the numerical approximation. When the a_{ij} coefficients are null for $j \geq i$, $i = 1, 2, \ldots, s$ then each k_i can be found explicitly with the $i - 1$ previous coefficients. The *RK* method is then explicit, otherwise it is implicit. In other words, if the a_{ij} is a lower triangular matrix with a null diagonal, the *RK* method is explicit

Method Construction

Let us rewrite the differential equation with a view to integrating the expression

$$\tfrac{\mathrm{d}v(t)}{\mathrm{d}t} = f\left(t, v(t)\right) \quad \text{or} \quad \mathrm{d}v(t) = f\left(t, v(t)\right)\mathrm{d}t$$

After integration between t_n and t_{n+1}, it gives:

$$v\left(t_{n+1}\right) = v\left(t_n\right) + \int\limits_{t_n}^{t_{n+1}} f\left(\tau, u(\tau)\right)\mathrm{d}\tau$$

The *RK* numerical scheme proposes to integrate the function $f : t \mapsto f\left(t, v(t)\right)$ thanks to a classic quadrature method. The simplest way approximate f with its value $f(t_n)$, is the rectangle method:

$$\tilde{v}\left(t_{n+1}\right) = \tilde{v}\left(t_n\right) + \int\limits_{t_n}^{t_{n+1}} f\left(t_n, \tilde{v}(t_n)\right)\mathrm{d}\tau = \tilde{v}\left(t_n\right) + f\left(t_n, \tilde{v}(t_n)\right) \int\limits_{t_n}^{t_{n+1}} \mathrm{d}\tau$$

TABLE A.2: Butcher table for Euler method

$$
\begin{array}{c|c}
0 & \\
\hline
 & 1
\end{array}
$$

TABLE A.3: Butcher table for modified Euler method

$$
\begin{array}{c|cc}
0 & 0 & \\
1/2 & 1/2 & 0 \\
\hline
 & 0 & 1
\end{array}
$$

then

$$\tilde{v}_{n+1} = \tilde{v}_n + hf(t_n, \tilde{v}_n)$$

And we find again the Euler method presented in 1. Its Butcher table is: With the midpoint method, the numerical scheme becomes:

$$\tilde{v}_{n+1} = \tilde{v}_n + hf(t_n + 1/2h, \tilde{v}_{n+1/2})$$

by replacing $\tilde{v}_{n+1/2} = \tilde{v}\,(t_n + 1/2h) = \tilde{v}_n + 1/2hf(t_n, \tilde{v}_n)$ with the Euler method:

$$\tilde{v}_{n+1} = \tilde{v}_n + hf(t_n + 1/2h, \tilde{v}_n + 1/2hf(t_n, \tilde{v}_n))$$

We find the modified Euler method The trapezoidal rule gives the Heun method

$$\tilde{v}_{n+1} = \tilde{v}_n + \frac{h}{2}\left[f(t_n, \tilde{v}_n) + f\left(t_{n+1}, \tilde{v}_n + hf(t_n, \tilde{v}_n)\right)\right]$$

TABLE A.4: Butcher table for Heun method

$$
\begin{array}{c|cc}
0 & 0 & \\
1 & 1 & 0 \\
\hline
 & 1/2 & 1/2
\end{array}
$$

TABLE A.5: Butcher table for the *RK*4 method

$$\begin{array}{c|cccc}
0 & 0 & & & \\
1/2 & 1/2 & 0 & & \\
1/2 & 0 & 1/2 & 0 & \\
1 & 0 & 0 & 1 & 0 \\
\hline
 & 1/6 & 2/6 & 2/6 & 1/6
\end{array}$$

TABLE A.6: Butcher table for Newton method

$$\begin{array}{c|cccc}
0 & 0 & & & \\
1/3 & 1/3 & 0 & & \\
2/3 & -1/3 & 1 & 0 & \\
1 & 1 & -1 & 1 & 0 \\
\hline
 & 1/8 & 3/8 & 3/8 & 1/8
\end{array}$$

In order to get higher order method we need to develop the exact solution v_n but also the numeric one $\tilde{v}_n$ with a Taylor series expansion near $h = 0$. A comparison between h^i coefficients for $i = 1, ..., p$ gives conditions for the parameters a_{ij} et b_i. Avoiding calculi, we simply show some Butcher Tables found in literature ([1] and [2]).

The first one is based on Simpson's rule, it is the "famous" *RK*4 method. It needs 4 evaluations of the function f and it is an explicit method. We can also write

$$k_1 = f\left(t_n, \tilde{v}_n\right)$$

$$k_2 = f\left(t_n + \frac{h}{2}, \tilde{v}_n + \frac{h}{2}k_1\right)$$

$$k_3 = f\left(t_n + \frac{h}{2}, \tilde{v}_n + \frac{h}{2}k_2\right)$$

$$k_4 = f\left(t_{n+1}, \tilde{v}_n + hk_3\right)$$

$$\tilde{v}_{n+1} = \tilde{v}_n + \frac{h}{6}\left[k_1 + 2k_2 + 2k_3 + k_4\right]$$

The next method also uses 4 evaluations but it is found according to Newton's rule. This table gives the following numerical scheme:

TABLE A.7: Butcher table for Cash-Karp method

0	0					
1/5	1/5	0				
3/10	3/40	9/40	0			
6/10	3/10	−9/10	12/10	0		
1	−11/54	5/2	−70/27	35/27	0	
7/8	1631/55296	175/512	575/13824	44275/110592	253/4096	0
	37/378	0	250/621	125/594	0	512/1771
	2825/27648	0	18575/48384	13525/55296	277/14336	1/4

$$k_1 = f\left(t_n, \tilde{v}_n\right)$$

$$k_2 = f\left(t_n + \frac{h}{3}, \tilde{v}_n + \frac{h}{3}k_1\right)$$

$$k_3 = f\left(t_n + \frac{2h}{3}, \tilde{v}_n - \frac{h}{3}k_1 + hk_2\right)$$

$$k_4 = f\left(t_{n+1}, \tilde{v}_n + hk_1 - hk_2 + hk_3\right)$$

$$\tilde{v}_{n+1} = \tilde{v}_n + \frac{h}{8}\left[k_1 + 3k_2 + 3k_3 + k_4\right]$$

The Cash-Karp method uses 6 evaluations of the function but it offers a 4 or 5 order approximation depending on the choice of the b_i coefficients.

The first line of the b_i coefficient gives the 5 order method whereas the second one proposes a 4 order method.

Finally the Runge-Kutta-Fehlberg method also uses 6 evaluations of the function and it proposes a 4 or 5 order approximation depending on the choice of the b_i coefficients. The first line of the b_i coefficient gives the 4 order method whereas the second one proposes a 5 order method.

A.2 Adaptative RK methods

Chemical or biological systems are kinetically described with a high number of reactions. This generally leads to a system of non linear differential equations. Concentrations (notation C_i for the i' reactant among a total of N reactants) are the time functions

TABLE A.8: Butcher table for Runge-Kutta-Fehlberg method

0	0					
$1/4$	$1/4$	0				
$12/32$	$3/32$	$9/32$	0			
$12/13$	$1932/2197$	$-7200/2197$	$7296/2197$	0		
1	$439/216$	-8	$3680/513$	$-845/4104$	0	
$1/2$	$-8/27$	2	$-3544/2565$	$1859/4104$	$-11/40$	0
	$25/216$	0	$1408/2565$	$2197/4104$	$-1/5$	0
	$16/135$	0	$6656/12825$	$28561/56430$	$-9/50$	$2/55$

we have to calculate. The numerical resolution depends on the constants rate (k_i) and the orders (α_i) of each reaction. The dynamical system can be written with a matrix structure.

$$\begin{cases} \frac{\mathrm{d}C(t)}{\mathrm{d}t} = F\left(t, C\right) \quad \text{with}\, t \in [0, T] \\ C(0) = C_0 \end{cases}$$

where $F : [0, T] \times \mathbb{R}^N \to \mathbb{R}^N$ is a continuous function ; $C_0 \in \mathbb{R}^N$ and $F : C \mapsto F(C)$ depends on the constants rate k_i and the orders α_i. Overall, *RK* methods obey the following scheme:

$$\tilde{C}_{n+1} = \tilde{C}_n + h\Phi\left(t_n, \tilde{C}_n, h\right)$$

where Φ is the increment function.

$$\Phi\left(t_n, \tilde{C}_n, h\right) = \sum_{i=1}^{s} \beta_i K_i \text{ with } \forall i \in [\![1, s]\!]\,,\ K_i = f\left(t_n + \delta_i h, \tilde{C}_n + h\sum_{j=1}^{s} \alpha_{ij} K_j\right)$$

s is the method number of stages.

The timescale over which chemical reactions occur covers many orders of magnitude. Without detailing the whole concept of convergence, *RK* methods converge and therefore are accurate enough only if the step size h is lower than the smallest characteristic time in the dynamical system. For instance, in *E. coli*, $O_2^{\bullet-}$ dismutation by SOD presents a half life of τ_1=25 μs ([3]) whereas H_2O_2 dismutation by catalase shows a half life of τ_2 =10 ms ([4]). In order to solve H_2O_2 evolution the step size of the numerical method has to be smaller than τ_2, but with a view to solving $O_2^{\bullet-}$ evolution it has to be under τ_1. Of course to approximate both evolutions, the step size has to be below the smallest half life. Let us first take h =1 μs. After 100 μs (four times the half life of $O_2^{\bullet -}$) $O_2^{\bullet -}$ has practically reached its steady state. The algorithm has run 100 time points. In order to observe 1 second with the same step size, the algorithm has to undergo a total of 1 million points of time evaluation. That number can decrease if we increase step size, indeed H_2O_2 evolution is slower. The method has to adapt the step size, small for fast evolution and high for slow evolution.

In order to adapt the step size h, we have to evaluate the local error. In practice the local error is estimated $a\,posteriori$ because it is easier than $a\,priori$. The method strategy uses two *RK* methods with different orders (p and $p+1$) but with the same K_i coefficients. The difference between the two approximative numerical solutions gives an estimation of the method local error.

One famous adaptive method is the Runge-Kutta Fehlberg which considers one *RK*4 and one *RK*5 explicit method:

$$\tilde{C}_{n+1}^{RK4} = \tilde{C}_n + h\left(\frac{25}{216}K_1 + \frac{1408}{2565}K_3 + \frac{2197}{4104}K_4 - \frac{1}{5}K_5\right)$$

$$\tilde{C}_{n+1}^{RK5} = \tilde{C}_n + h\left(\frac{16}{135}K_1 + \frac{6656}{12825}K_3 + \frac{28561}{56430}K_4 - \frac{9}{50}K_5 + \frac{2}{55}K_6\right)$$

$$K_1 = F\left(t_n, \tilde{C}_n\right)$$

$$K_2 = F\left(t_n + \frac{h}{4}, \tilde{C}_n + \frac{h}{4}K_1\right)$$

$$K_3 = F\left(t_n + \frac{3h}{8}, \tilde{C}_n + \frac{3h}{32}K_1 + \frac{9h}{32}K_2\right)$$

$$K_4 = F\left(t_n + \frac{12h}{13}, \tilde{C}_n + \frac{1932h}{2197}K_1 - \frac{7200h}{2197}K_2 + \frac{7296h}{2197}K_3\right)$$

$$K_5 = F\left(t_n + h, \tilde{C}_n + \frac{439h}{216}K_1 - 8hK_2 + \frac{3680h}{513}K_3 - \frac{845h}{4104}K_4\right)$$

$$K_6 = F\left(t_n + \frac{h}{2}, \tilde{C}_n - \frac{8h}{27}K_1 + 2hK_2 - \frac{3544h}{2565}K_3 - \frac{1859h}{4104}K_4 - \frac{11h}{40}K_5\right)$$

$\tilde{C}_{n+1}^{RK4}$ (respectively $\tilde{C}_{n+1}^{RK5}$) represent the numerical approximation of $C_n = C(t_n)$ given by the *RK*4 (respectively *RK*5) method. The local error obtained after the n' iteration

E_n with a step size h_n is evaluated in the following way:

$$E_n = \tilde{C}_{n+1}^{RK4} - \tilde{C}_{n+1}^{RK5} = \left(\tilde{C}_{n+1}^{RK4} - C_{n+1}\right) - \left(\tilde{C}_{n+1}^{RK5} - C_{n+1}\right) = O(h_n^5) + O(h_n^6) \approx Ah_n^5$$

After the next iteration, the local error is $E_{n+1} \approx Ah_{n+1}^5$. As a result, $E_{n+1} = E_n\left(\frac{h_{n+1}}{h_n}\right)^5$. We wish the local error to remain lower than a given tolerance ε, therefore $E_{n+1} \leq \varepsilon$. Then $E_{n+1} = E_n\left(\frac{h_{n+1}}{h_n}\right)^5 < \varepsilon$ or $h_{n+1} < h_n\left(\frac{\varepsilon}{E_n}\right)^{1/5}$ The local error is calculated after each iteration until the end of the simulation.

If the error criteria are respected, the approximative solution estimated by the *RK*5 method is kept and the step size can increase with the rule : $h_{n+1} = \min\left(h_{\max},\, \frac{3}{2}h_n,\, h_n\left(\frac{\varepsilon}{E_n}\right)^{1/5}\right)$, otherwise $h_{n+1} = \max\left(h_{\min},\, \frac{1}{2}h_n,\, h_n\left(\frac{\varepsilon}{E_n}\right)^{1/5}\right)$. $h_{\min}$ et $h_{\max}$ represent the extreme values for the step size. This method is used by the $MATLAB$® ode45 function or the $Python$ odeint function.

A.3 Multistep methods

Let us consider the following ODE with its Cauchy problem:

$$\begin{cases} \frac{\mathrm{d}u(t)}{\mathrm{d}t} = f\,(t,u)\, t \in [0,T] \\ \qquad u(0) = u_0 \end{cases}$$

where $f : [0,T] \times \mathbb{R} \to \mathbb{R}$ is a continuous function and $u_0 \in \mathbb{R}$. With a view to constructing a numerical approximation, the discretization is made with the step size h which involves the uniform subdivision $(t_n)_{n\in[0,N]}$ for the interval $[0,T]$: $t_n = nh$, then $\tilde{u}_n$ is a numerical approximation of $u_n = u(t_n)$ for $0 \leq n \leq N$.

We introduce multistep methods (MS). A p-steps method calculates $\tilde{u}_{n+1}$ with the values $\tilde{u}_n$, $\tilde{u}_{n-1}$,…, $\tilde{u}_{n+1-p}$. MS methods need a specific procedure to start and calculate the $p-1$ first values $\tilde{u}_1$, $\tilde{u}_2$,…, $\tilde{u}_{p-1}$. An *RK* method is generally used.

A.3.1 Adams-Bashforth methods

Presentation

An integration of the problem gives:

$$u\left(t_{n+1}\right)=u\left(t_n\right)+\int\limits_{t_n}^{t_{n+1}} f\left(\tau, u(\tau)\right) \mathrm{d}\tau$$

The method approximates the function f with the interpolating polynomial of degree $p-1$ at node $\left(t_{n-i}, f_{n-i}\right)$ for $0 \leq i \leq p-1$ with the notation $f_k=f\left(t_k, u_k\right)$. Then

$$\tilde{u}_{n+1}=\tilde{u}_n+h \sum_{k=0}^{p-1} \beta_{p,k}^n f_{n-k} \quad \text{with } \beta_{p,k}^n=\frac{1}{h} \int\limits_{t_n}^{t_{n+1}} \ell_{p,k}^n(t)\, \mathrm{d}t$$

$\ell_{p,k}^n$ is the Lagrange interpolating polynomial of degree $p-1$; $\ell_{p,k}^n(t_{n-q})=\delta_{k,q}$. The Adams-Bashforth methods are explicit.

Examples

2-steps method

Les us introduce Π the interpolating polynomial of f at the two nodes $\left(t_{n-1}, f_{n-1}\right)$ and $\left(t_n, f_n\right)$.

$$\Pi(t)=\left(f_n-f_{n-1}\right) \frac{t-t_n}{t_n-t_{n-1}}+f_{n-1}=\frac{\left(f_n-f_{n-1}\right)}{h}\left(t-t_n\right)+f_{n-1}$$

This yields:

$$\tilde{u}_{n+1}=\tilde{u}_n+\int\limits_{t_n}^{t_{n+1}} \Pi(t) \mathrm{d}t=\tilde{u}_n+\frac{\left(f_n-f_{n-1}\right)}{h}\left[\frac{\left(t-t_n\right)^2}{2}\right]_{t_n}^{t_{n+1}}+f_{n-1}\left[t\right]_{t_n}^{t_{n+1}}$$

And finally

$$\tilde{u}_{n+1}=\tilde{u}_n+\frac{\left(f_n-f_{n-1}\right)}{h}\left[\frac{3h^2}{2}\right]+f_{n-1} h$$

or

$$\tilde{u}_{n+1}=\tilde{u}_n+h\left(\frac{3}{2} f_n-\frac{1}{2} f_{n-1}\right)$$

In a similar way, it gives:

3-steps method: $\tilde{u}_{n+1} = \tilde{u}_n + \frac{h}{12}\left(23 f_n - 16 f_{n-1} + 5 f_{n-2}\right)$

4-steps method: $\tilde{u}_{n+1} = \tilde{u}_n + \frac{h}{24}\left(55 f_n - 59 f_{n-1} + 37 f_{n-2} - 9 f_{n-3}\right)$

5-steps method: $\tilde{u}_{n+1} = \tilde{u}_n + \frac{h}{720}\left(1901 f_n - 2774 f_{n-1} + 2616 f_{n-2} - 1274 f_{n-3} + 251 f_{n-4}\right)$

A.3.2 Adams-Moulton methods

Presentation

By integrating:

$$u\left(t_{n+1}\right) = u\left(t_n\right) + \int\limits_{t_n}^{t_{n+1}} f\left(\tau, u(\tau)\right) \mathrm{d}\tau$$

Here we approximate the function f with an interpolating polynomial of degree p at nodes $\left(t_{n+1-i}, f_{n+1-i}\right)$ for $0 \leq i \leq p$ with the notation $f_k = f\left(t_k, u_k\right)$. The Adams-Moulton methods are implicit.

Examples

1-step method

Let us introduce Π the interpolating polynomial of f at nodes (t_{n+1}, f_{n+1}) (t_n, f_n).

$$\Pi(t) = \left(f_{n+1} - f_n\right) \frac{t - t_n}{t_{n+1} - t_n} + f_n = \frac{\left(f_{n+1} - f_n\right)}{h} \left(t - t_n\right) + f_n$$

It gives:

$$\tilde{u}_{n+1} = \tilde{u}_n + \int\limits_{t_n}^{t_{n+1}} \Pi(t) \mathrm{d}t = \tilde{u}_n + \frac{\left(f_{n+1} - f_n\right)}{h} \left[\frac{\left(t - t_n\right)^2}{2}\right]_{t_n}^{t_{n+1}} + f_n \left[t\right]_{t_n}^{t_{n+1}}$$

Finally $\tilde{u}_{n+1} = \tilde{u}_n + \frac{\left(f_{n+1} - f_n\right)}{h}\left[\frac{h^2}{2}\right] + f_n h$ or

$$\tilde{u}_{n+1} = \tilde{u}_n + \frac{h}{2}\left(f_{n+1} + f_n\right)$$

We found the trapezoid rule.

In a similar way:

2-steps method: $\tilde{u}_{n+1} = \tilde{u}_n + \frac{h}{12}\left(5f_{n+1} + 8f_n - f_{n-1}\right)$

3-steps method: $\tilde{u}_{n+1} = \tilde{u}_n + \frac{h}{24}\left(9f_{n+1} + 19f_n - 5f_{n-1} + f_{n-2}\right)$

4-steps method: $\tilde{u}_{n+1} = \tilde{u}_n + \frac{h}{720}\left(251f_{n+1} + 646f_n - 264f_{n-1} + 106f_{n-2} - 19f_{n-3}\right)$

A.3.3 Nyström methods

Presentation

ODE integration gives:

$$u\left(t_{n+1}\right) = u\left(t_{n-1}\right) + \int\limits_{t_{n-1}}^{t_{n+1}} f\left(\tau, u(\tau)\right) \mathrm{d}\tau$$

The function f is approximated with an interpolating polynomial of degree $p-1$ at nodes $\left(t_{n-i}, f_{n-i}\right)$ for $0 \leq i \leq p-1$ with $f_k = f\left(t_k, u_k\right)$. The Nyström methods are explicit.

Examples

2-steps method

Π is the interpolating polynomial of f at nodes $\left(t_{n-1}, f_{n-1}\right)$ and $\left(t_n, f_n\right)$.

$$\Pi(t) = \left(f_n - f_{n-1}\right)\frac{t - t_n}{t_n - t_{n-1}} + f_{n-1} = \frac{\left(f_n - f_{n-1}\right)}{h}\left(t - t_n\right) + f_{n-1}$$

It gives:

$$\tilde{u}_{n+1} = \tilde{u}_{n-1} + \int\limits_{t_{n-1}}^{t_{n+1}} \Pi(t)\mathrm{d}t = \tilde{u}_n + \frac{\left(f_n - f_{n-1}\right)}{h}\left[\frac{\left(t - t_n\right)^2}{2}\right]_{t_{n-1}}^{t_{n+1}} + f_{n-1}\left[t\right]_{t_{n-1}}^{t_{n+1}}$$

Finally $\tilde{u}_{n+1} = \tilde{u}_{n-1} + \frac{\left(f_n - f_{n-1}\right)}{h}\left[\frac{4h^2}{2}\right] + 2f_{n-1}h$ and

$$\tilde{u}_{n+1} = \tilde{u}_{n-1} + 2hf_n$$

It is also called the Leapfrog method.

In a similar way:

3-steps method: $\tilde{u}_{n+1} = \tilde{u}_{n-1} + \frac{h}{3}\left(7f_n - 2f_{n-1} + f_{n-2}\right)$

4-steps method: $\tilde{u}_{n+1} = \tilde{u}_{n-1} + \frac{h}{3}\left(8f_n - 5f_{n-1} + 4f_{n-2} - f_{n-3}\right)$

A.3.4 Milne-Simpson methods

Presentation

These methods use the following integration:

$$u\left(t_{n+1}\right) = u\left(t_{n-1}\right) + \int\limits_{t_{n-1}}^{t_{n+1}} f\left(\tau, u(\tau)\right) \mathrm{d}\tau$$

The function f is now approximated by the interpolating polynomial of degree p at nodes $\left(t_{n+1-i}, f_{n+1-i}\right)$ for $0 \leq i \leq p$ with $f_k = f\left(t_k, u_k\right)$. The Milne-Simpson methods are implicit.

Examples

2-steps method

Π is the interpolating polynomial of f of degree 2 at nodes $\left(t_{n+1}, f_{n+1}\right)$, $\left(t_n, f_n\right)$ and $\left(t_{n-1}, f_{n-1}\right)$.

$$\Pi(t) = f_{n+1}\frac{\left(t - t_n\right)}{\left(t_{n+1} - t_n\right)}\frac{\left(t - t_{n-1}\right)}{\left(t_{n+1} - t_{n-1}\right)} + f_n\frac{\left(t - t_{n+1}\right)}{\left(t_n - t_{n+1}\right)}\frac{\left(t - t_{n-1}\right)}{\left(t_n - t_{n-1}\right)} + f_{n-1}\frac{\left(t - t_{n+1}\right)}{\left(t_{n-1} - t_{n+1}\right)}\frac{\left(t - t_n\right)}{\left(t_{n-1} - t_n\right)}$$

Then

$$\Pi(t) = \frac{f_{n+1}}{2h^2}\left(t - t_n\right)\left(t - t_{n-1}\right) - \frac{f_n}{h^2}\left(t - t_{n+1}\right)\left(t - t_{n-1}\right) + \frac{f_{n-1}}{2h^2}\left(t - t_{n+1}\right)\left(t - t_n\right)$$

Since $\tilde{u}_{n+1} = \tilde{u}_{n-1} + \int\limits_{t_{n-1}}^{t_{n+1}} \Pi(t)\,\mathrm{d}t$:

$$\tilde{u}_{n+1} = \tilde{u}_{n-1} + \frac{h}{3}\left(f_{n+1} + 4f_n + f_{n-1}\right)$$

A.3.5 Backward Differentiation Formulas

BDF methods are MS implicit methods. BDF directly approximate the value of the first derivative of u at node t_{n+1} through the first derivative of the polynomial interpolating u at the $q+2$ nodes $t_{n+1},\ t_n, \ldots, t_{n-q}$, where $p = q+1$ represents the step of the method.

2-steps method

Π is the integrating polynomial of degree 2 of u at nodes (t_{n+1}, u_{n+1}), (t_n, u_n) and (t_{n-1}, u_{n-1}). In a similar way:

$$\Pi(t) = \frac{u_{n+1}}{2h^2}\left(t - t_n\right)\left(t - t_{n-1}\right) - \frac{u_n}{h^2}\left(t - t_{n+1}\right)\left(t - t_{n-1}\right) + \frac{u_{n-1}}{2h^2}\left(t - t_{n+1}\right)\left(t - t_n\right)$$

The derivative of Π at t_{n+1} is:

$$\frac{\mathrm{d}\Pi}{\mathrm{d}t}(t_{n+1}) = \frac{u_{n+1}}{2h^2}\left(2t_{n+1} - (t_{n-1} + t_n)\right) - \frac{u_n}{h^2}\big(2t_{n+1} - (t_{n+1} + t_{n-1})\big) + \frac{u_{n-1}}{2h^2}\big(2t_{n+1} - (t_{n+1} + t_n)\big)$$

and finally $\frac{\mathrm{d}\Pi}{\mathrm{d}t}(t_{n+1}) = \frac{3u_{n+1}}{2h} - \frac{4u_n}{2h} + \frac{u_{n-1}}{2h}$

Considering the EDO

$$\begin{cases} \frac{\mathrm{d}u(t)}{\mathrm{d}t} = f\left(t, u\right) \quad t \in [0, T] \\ u(0) = u_0 \end{cases}$$

At t_{n+1}, $\frac{\mathrm{d}u}{\mathrm{d}t}(t_{n+1}) = f\left(t_{n+1}, u_{n+1}\right) = f_{n+1}$, therefore numerical approximation gives

$$\frac{\mathrm{d}\Pi}{\mathrm{d}t}(t_{n+1}) = \frac{3\tilde{u}_{n+1}}{2h} - \frac{4\tilde{u}_n}{2h} + \frac{\tilde{u}_{n-1}}{2h} = f\left(t_{n+1}, \tilde{u}_{n+1}\right) = f_{n+1}$$

$$\tilde{u}_{n+1} = \frac{4}{3}\tilde{u}_n - \frac{1}{3}\tilde{u}_{n-1} + \frac{2}{3}hf_{n+1}$$

We can also calculate:

3-steps method: $\tilde{u}_{n+1} = \frac{18}{11}\tilde{u}_n - \frac{9}{11}\tilde{u}_{n-1} + \frac{2}{11}\tilde{u}_{n-2} + \frac{6}{11}hf_{n+1}$

4-steps method: $\tilde{u}_{n+1} = \frac{48}{25}\tilde{u}_n - \frac{36}{25}\tilde{u}_{n-1} + \frac{16}{25}\tilde{u}_{n-2} - \frac{3}{25}\tilde{u}_{n-3} + \frac{12}{25}hf_{n+1}$

5-steps method: $\tilde{u}_{n+1} = \frac{300}{137}\tilde{u}_n - \frac{300}{137}\tilde{u}_{n-1} + \frac{200}{137}\tilde{u}_{n-2} - \frac{75}{137}\tilde{u}_{n-3} + \frac{12}{137}\tilde{u}_{n-4} + \frac{60}{137}hf_{n+1}$

6-steps method:

$$\tilde{u}_{n+1} = \frac{360}{147}\tilde{u}_n - \frac{450}{147}\tilde{u}_{n-1} + \frac{400}{147}\tilde{u}_{n-2} - \frac{225}{147}\tilde{u}_{n-3} + \frac{72}{147}\tilde{u}_{n-4} - \frac{10}{147}\tilde{u}_{n-5} + \frac{60}{147}hf_{n+1}$$

Bibliography

[1] F. S. A. Quarteroni R. Sacco, Numerical Mathematics. Berlin: Springer, 2007.

[2] L. Uhl, 1001 codes Python pour la Modélisation. Paris: Ellipse, 2014.

[3] J. A. Imlay and I. Fridovich, "Assay of metabolic superoxide production in Escherichia coli", J. Biol. Chem., vol. 266, no. 11, pp. 6957–6965, Apr. 1991.

[4] L. C. Seaver and J. A. Imlay, "Hydrogen peroxide fluxes and compartmentalization inside growing Escherichia coli", J. Bacteriol., vol. 183, no. 24, pp. 7182–7189, Dec. 2001.

Appendix B

A passive physical model for DnaK chaperoning and disaggregation

B.1 Introduction

Protein chaperones are present in all domains of life and serve multiple functions in protein homeostasis. DnaK chaperone network controls proteostasis in bacteria. It plays an essential role in the prevention and the amelioration of stress-induced protein damage. In over 1200 sequenced bacterial genomes, only two members of the order Aquificales lack HSP70 genes [1]. Actually, one major challenge for cells is to ensure that proteins are properly folded and targeted to the different cellular compartments. External stress may eventually lead to proteostasis breakdown and in particular to protein misfolding. Therefore, to cope with noxious off pathways in protein fate, cells have evolved universally with a view to conserving molecular chaperones which act to guide the precise partitioning, localization and folding of proteins [2, 3]. DnaK chaperones are essential during the protein denaturation that occurs during heat shock or other external stress [4–7].

During stress, the DnaK can bind and prevent the aggregation of misfolded proteins and thereafter act to solubilize protein aggregates. Therefore chaperone functions are closely linked to protein folding and aggregate processes [8–10].

In unstressed cells, DnaK localizes to multiple and dynamic foci, but re-localizes to focal protein aggregates during stationary phase. The number of foci varied among cells [11] and within the same cell at different time points, however the number of foci had a slightly negative correlation with the length of the cell. Fay and Glickman indicated that DnaK has two modes of chaperone function, a first one in native protein folding in which it is localized in peripheral foci, and a second one in aggregate stress processing in which DnaK re-localizes to central immobile foci of protein aggregates.

Our experimental data (figure B.1) also show this original behaviour. First located on foci, DnaK proteins quickly diffuse during alcoholic stress in order to interact with abnormal protein. DnaK is then located on the abnormal protein aggregate and finally goes back to foci. The aim of this work is to reproduce such behaviour using kinetic constants (rate constants or diffusion coefficients) found in literature. Actually, using computational modelling, we wonder whether the known properties of the DnaK system are sufficient to reproduce the observed dynamics using only classical physical and chemical laws.This issue was already raised 70 years ago by Erwin Schrödinger when he wrote "What is life". He was already interested in whether new physical or new chemical laws were necessary to describe biological systems. Like the DnaK issue, he wondered how "a single group of atoms existing in one copy produces orderly events".

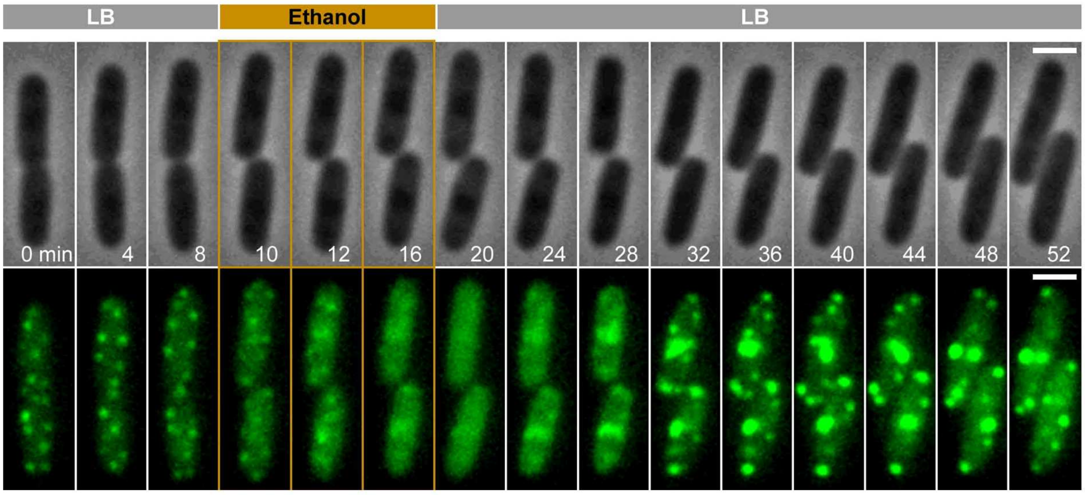

FIGURE B.1: Green fluorescent DnaK protein microscopy. Time-lapse microscopy of DnaK aggregates during *E. coli* outgrowth in LB with an alcoholic stress. Exposure time was 6 minutes. Time in white indicates minutes after start of outgrowth. The white bar (at 52 minutes) indicates 1 μm.

B.2 Materials and methods

The standard assumption for biochemical models is that the spatial distribution of reactants is homogeneous. Actually with this hypothesis, the system can be described with ordinary differential equations (ODE) or partial differential equations (PDE) easy to compute. Nevertheless, this assumption suffers some exceptions [12, 13]. The homogeneity of the chemical component concentration depends on the diffusion rate in the cell. Instead of using ODE or PDE with finite differences, one way to handle the vast state space is to use a Monte Carlo method introduced by Gillespie in 1976 [14, 15]. This section studies a mesoscopic reaction-diffusion with protein compartmentalization solved with the Next Sub-volume Method, a Gillespie like mesoscopic and stochastic algorithm proposed by Elf et al. [16, 17]. At each time interval, the reaction that occurs is chosen randomly according to the probabilities for the reaction to take place. The probabilities depend on both the number of molecules and the rate constants.

B.2.1 Presentation of the model

The DnaK chaperone system has been characterized in *E. coli* and seems to have important functions in stress resistance. The minimal model of the DnaK mechanism in *E. coli* cells should include description of many chemical reactions. In many cases detailed mechanisms and kinetics of molecular processes are not perfectly known. Chaperone proteins interact with their substrate which can aggregate. Non-linearities arising from this complex topology of such networks make it difficult to intuit quantitative or even qualitative behaviour of the system.

In this study, we propose a simple model based on reaction-diffusion. Diffusion follows macromolecular diffusion law in crowded solution (Han and Herzfeld 1993) and enzymatic reactions obey the Michaelis-Menten mechanism. In our model we only use known physical or chemical properties of molecule. The model considers a few hypotheses which are quickly described here.

In the DnaK action model, considering 4 types of molecules (DnaK, abnormal proteins, DnaK-protein complex and normal proteins), different events occur with different probabilities.

In our model, the Michaelis-Menten mechanism is :

$$\begin{array}{ccccc} E & + & P^* & \underset{k_{-1}}{\overset{k_1}{\rightleftharpoons}} & EP^* \xrightarrow{k_2} E + P \\ \uparrow k_0 & & \uparrow k'_0 & & \\ production & & P & & \end{array}$$

Where E is the DnaK enzyme, P^* the abnormal protein, EP^* the DnaK-protein complex and P the normal protein.

To mimic the aggregation phenomenon, we consider that when two molecules of P^* meet, they create a physical or chemical binding, the produced dimmer $(P^*)_2$ has a higher molecular weight involving a smaller diffusion coefficient. The dimmer can also be associated with other P^* and step by step there will appear an aggregate of n abnormal proteins $(P^*)_n$. In order to describe the aggregation we use the random polymerization model proposed by Kodaka [18]. The more size aggregate grows, the more its diffusion coefficient decreases thanks to crowding effect [19] and size effect [20–22].

To mimic the initial DnaK foci, we only suppose that there are areas in the cell which are characterised with a 50 times smaller diffusion coefficient. We simply consider that those areas present more interactions like Van der Waals forces or hydrogen bonding that act as if the media present a higher viscosity and by consequence a smaller diffusion coefficient. Therefore the probability for DnaK to stay on foci is fifty time greater than outside the foci.

B.2.2 The aggregation phenomenon

To describe the aggregation phenomenon, we use the random polymerization model proposed by Kodaka [18].

$$r = 1 - \frac{1}{1 + k_P[P^*]_0 t}$$

In this case, $[P^*]_0$ is the initial concentration of abnormal protein monomer. r is the fraction of the total binding sites already engaged in bonding. k_P is the rate constant of the bimolecular association.

The increasing of aggregate size also involves modification in its diffusion coefficient. Two effects have been taken into account: the first one is the crowding effect developed by Han and Herzfeld [19] and the second one is the size effect well described by other teams [20–22] and principally based on the Stockes-Einstein equation.

The crowding and confinement effects show that the apparent diffusion coefficient decreases roughly exponentially with the protein volume fraction ν_p according to the function β.

Moreover, the size effect essentially shows that the diffusion coefficients also depend on the protein size according to the inverse of the cube root function α.

Therefore, we adopt the following equation to mimic the evolution of the diffusion coefficient with the degree of polymerisation:

$$D_n = D_1 \cdot \overbrace{\alpha(n)}^{\substack{size\\effect}} \cdot \underbrace{\beta(n)}_{\substack{crowding\\effect}}$$

$$\alpha(n) = (n)^{-\frac{1}{3}}$$

$$\beta(n) = \exp\left(-\frac{2}{3}\left(3\frac{v_p}{1-v_p} + \frac{9}{2}\frac{{v_p}^2}{(1-v_p)^2} + \frac{9}{4}\frac{{v_p}^3}{(1-v_p)^3}\right)\right)$$

D_1 represents the diffusion coefficient of the monomer. v_p is the volume fraction defined as the volume of an aggregate divided by the volume of the mixture prior to mixing. This value is directly linked to the degree of polymerization of the aggregate.

B.2.3 Algorithm

The algorithm is published as supplementary material to Elf and Ehrenberg [17, 23]. It is a Gillespie-like [14, 15] method approaching the spatial effects of diffusive phenomena and chemical reaction.

The event data consists of two types : reactions and diffusions. Reactions describe the chemical interaction between particles within one sub-volume. As a consequence, the number of particles change within the sub-volume according to the chemical reaction stoichiometry.

Diffusions describe the movement of a molecule from one sub-volume to a neighbouring sub-volume. The reaction and diffusion rates in a single sub-volume depend on the numbers of molecules and their rate constants or diffusion coefficient.

The propensity p_r that a first order kinetic reaction $A \rightarrow product$ occurs in a sub-volume with volume V during the next time $\mathrm{d}t$ is modelled as $r \cdot \mathrm{d}t \cdot V$ where it is indicated that the rate r depends on the concentrations c of the reactant A in sub-volume and the rate constant k. The kinetic law is therefore $r = k \cdot c$ and the propensity of the reaction is : $p_r = k \cdot c \cdot V \cdot \mathcal{N_A} \cdot \mathrm{d}t$, or $p_r = k \cdot n_A \cdot \mathrm{d}t$ assuming $c = \frac{n_A}{V\mathcal{N_A}}$ and n_A is the number of A molecules ($\mathcal{N_A}$ is the Avogadro constant). If this reaction occurs, the number of A molecules in the sub-volume is reduced by one and the number of product molecules is increased by one. A chemical reaction only affects one sub-volume state.

For a second order kinetic reaction $A+B \rightarrow product$, the kinetic law is : $r = k \cdot c_A \cdot c_B$ and the propensity of the reaction is : $p_r = \frac{k}{V\mathcal{N_A}} \cdot n_A \cdot n_B \cdot \mathrm{d}t$.

The diffusion of an A molecule to a neighbouring sub-volume is treated as a first order reaction with a rate constant of $k_d = \frac{D}{\ell^2}$, where D is the diffusion coefficient of A and ℓ is the side length of the sub-volume. Therefore, the propensity that an A molecule diffuses from one sub-volume i to one of its neighbours j during $\mathrm{d}t$ is $p_d = k_d \cdot n_A \cdot \mathrm{d}t = \frac{D}{\ell^2} \cdot n_A \cdot \mathrm{d}t$. If a diffusion event occurs the number of A molecules in sub-volume i decreased by one and the number is increased by one in its neighbour j.

Let us enumerate the different molecules considered in the model and their possible events:

For the enzyme E :

- E can diffuse with propensity $\frac{D_E}{\ell^2} \cdot n_E \cdot \mathrm{d}t$ in the cell and with probability $\varepsilon \frac{D_E}{\ell^2} \cdot$

$n_E \cdot \mathrm{d}t$ in the foci. $\varepsilon < 1$ indicates that the enzyme has a better affinity for the sub-volume that represents the foci.

- E can react with $(P^*)_n$ with propensity $\frac{k_1}{V} \cdot n_E \cdot n_{P^*} \cdot \mathrm{d}t$,
- E can appear as a product of the complex dissociation with propensity $k_{-1} \cdot n_{EP^*} \cdot \mathrm{d}t$,
- E can be produced with probability $k_0 \cdot \mathrm{d}t$ which does not depend on any concentration, but this propensity falls to zero after the ethanol flux is stopped.

For the abnormal protein or aggregate $(P^*)_n$:

- $(P^*)_n$ can diffuse with propensity $\frac{D_n}{\ell^2} \cdot n_{P^*} \cdot \mathrm{d}t$,
- $(P^*)_n$ can react with E with propensity $\frac{k_1}{V} \cdot n_E \cdot n_{P^*} \cdot \mathrm{d}t$,
- $(P^*)_n$ can appear as a product of the complex dissociation with propensity $k_{-1} \cdot n_{EP^*} \cdot \mathrm{d}t$.
- $(P^*)_n$ can be produced with propensity $k_0' \cdot \mathrm{d}t$ which does not depend on any concentration, but this propensity falls to zero after the ethanol flux is stopped.

For the complex:

- EP^* can diffuse with the same propensity as $(P^*)_n$ (i.e. $\frac{D_n}{\ell^2} \cdot n_{P^*} \cdot \mathrm{d}t$) because it is bound to the aggregate,
- EP^* can dissociate to E and P^* with propensity $k_{-1} \cdot n_{EP^*} \cdot \mathrm{d}t$,
- EP^* can dissociate to E and P with propensity $k_2 \cdot n_{EP^*} \cdot \mathrm{d}t$,
- EP^* can appear as a product of the reaction between E and P^* with propensity $\frac{k_1}{V} \cdot n_E \cdot n_{P^*} \cdot \mathrm{d}t$.

B.2.4 Constants used for simulation and validity

According to the Next Sub-volume Method, the side length ℓ of the square sub-volumes has to satisfy the two inequalities

$$R \ll \ell \text{ and } \frac{\ell^2}{6D} \ll \tau_{\min} \text{ (*)}$$

where R is the larger protein radius and D the smallest diffusion constant

The first inequality indicates that dissociation events can be properly defined within sub-volumes. The second criterion specifies that the time for any molecule to leave a sub-volume is much smaller than the shortest reaction time τ_{min} among the molecular species, so that all molecules are homogeneously distributed within the sub-volumes.

The 3D simulations were performed with $\ell = 0.1\,\mu$m and the depth $h = \ell$ of the sub-volumes, which is many times larger than the average protein radius.

Then we checked that the characteristic time of each reaction is much larger than the characteristic time of diffusion of the molecule.

The Michaelis-Menten [24] mechanism used in our simulation is :

$$\begin{array}{ccl} E & + & P^* \overset{k_1}{\underset{k_{-1}}{\rightleftharpoons}} EP^* \xrightarrow{k_2} E + P \\ \uparrow k_0 & & \uparrow k'{}_0 \\ \mathit{production} & & P \end{array}$$

Where k_0 and k'_0 are respectively the rate constant of production of DnaK and abnormal protein during the ethanol stress step occurring during the first 6 minutes.

Let us examine the incidence of each reaction and its constant rate.

- Reaction $E + P^* \xrightarrow{k_1} EP^*$

  $k_1 = 4.5 \cdot 10^5$ mol^{-1}.L.s^{-1} (Schmid *et al.* 1994) is a second order rate constant involving a half life time $\tau_1 = \frac{1}{k_1 c}$ where c is the concentration of reacting molecules which is given by $c = \frac{N}{\mathcal{N}_A V}$ (the Avogadro constant $\mathcal{N}_A \approx 6 \cdot 10^{23}$ mol^{-1}). Considering $N \approx 10$ molecules of moving P^* or E in the sub-volume $V = \ell^3 = 10^{-18}$ L, the concentration is then $c \approx 20\,\mu$mol.L^{-1} and $\tau_1 = 0.1$ s. This value has to be compared to $\ell^2/6D$ where D is the diffusion coefficient of the reacting molecule.

Literature reports a large range of value [25–29] from 10^{-15} to 10^{-11} $\mathrm{m}^2.\mathrm{s}^{-1}$, but the (*) relation imposes that $D \gg \frac{\ell^2}{6\tau_1} \approx 10^{-14}$ $\mathrm{m}^2.\mathrm{s}^{-1}$. We tested many values and we noticed that under 10^{-13} $\mathrm{m}^2.\mathrm{s}^{-1}$ simulations do not give the same results and do not follow the experimental data.

- Reaction $EP^* \xrightarrow{k_{-1}} E + P^*$

  $k_{-1} = 1.8$ s^{-1} is a first order rate constant [30] involving a half life time $\tau_{-1} = \frac{\ln 2}{k_{-1}} = 0.4$ s. This value gives the same conclusion as the previous one.

- Reaction $EP^* \xrightarrow{k_2} E + P$

  $k_2 = 0.011$ s^{-1} Schlecht *et al.* [31] give a half life time $\tau_2 = \frac{\ln 2}{k_2} = 63$ s which is higher than the later one, therefore the conclusions do not change.

- Reaction $P \rightarrow P^*$

  $k'_0 = 0.045$ molecule.s^{-1} is the rate of abnormal protein production during stress, with a half life time $\tau'_0 = \frac{1}{k''_0} \approx 22$ s $\gg \frac{\ell^2}{6D}$. This value was calculated so that aggregated proteins increase from 0 to 35000 during the 6 min of the alcoholic stress of our simulation. Actually, Winkler *et al.* [32] estimate that maximal aggregated proteins is about 33000.

- Reaction $\phi \rightarrow E$

  $k_0 = 7 \cdot 10^{-4}$ molecule.s^{-1} is the rate of enzyme production with a half life time $\tau_0 = \frac{1}{k_0} \approx 1400$ s. ($\tau_0 \gg \frac{\ell^2}{6D}$). The initial pool of DnaK was set to about 9300 molecules and this induction rate allows them to increase to 10000 molecules. This value can be compared with the 9900 proposed by Mogk *et al.* [16].

In the case of the highest diffusion constant for a protein ($D_1 = 5 \cdot 10^{-11}$ $\mathrm{m}^2\mathrm{s}^{-1}$), $\ell^2/6D_1$ is about 33 μs, which is much shorter than the chemical life times of all molecules.

B.3 Results and discussion

Due to the stochastic nature of this algorithm, a single execution is not sufficient to draw one satisfactory conclusion. Therefore, a number of replications of the same model but with different seeds for the random number generator were run. Simulations always show similar patterns.

To simulate the interactions between molecules in a spatial and temporal context, the Next Sub-volume Method imposes a grid on the inner cell volume. In each sub-volume, we set a homogeneous distribution of particles of which interactions are described by events. These events take place with specific rates that depend on the state of the sub-volume which is characterized by the current number of particles and the different rate of reaction or diffusion. The time between one event and another is an exponentially distributed random number with mean equal to the reciprocal of the sum of reaction and diffusion rates. Therefore a high kinetic rate, high diffusion constants or a large number of particles inside the sub-volume involves a drastic reduction of the inter-event times which can fall under the millisecond. Consequently the system can undergo enormous modifications within one second. Such a phenomenon occurs during the aggregate formation.

DnaK are initially placed on 4 foci. Aggregation of abnormal protein (Figure B.3) and DnaK diffusion (Figure B.2) outside foci take place in less than 1 min like in the experiment. Simulation shows the aggregation of proteins on random areas and the superposition of the DnaK chaperone on the same areas.

One of the amazing observations (Figure B.2) is that DnaK come back to their initial foci after the destruction of the aggregate and this phenomenon occurs without any active processes, indeed our model is only based on passive processes such as diffusion.

In order to check the influence of compartmentalization during the action of DnaK we made different simulations with or without aggregation and with or without the foci.

We first observed the system without aggregation and without the foci; this system is perfectly homogeneous. It can therefore also be solved thanks to a set of ordinary

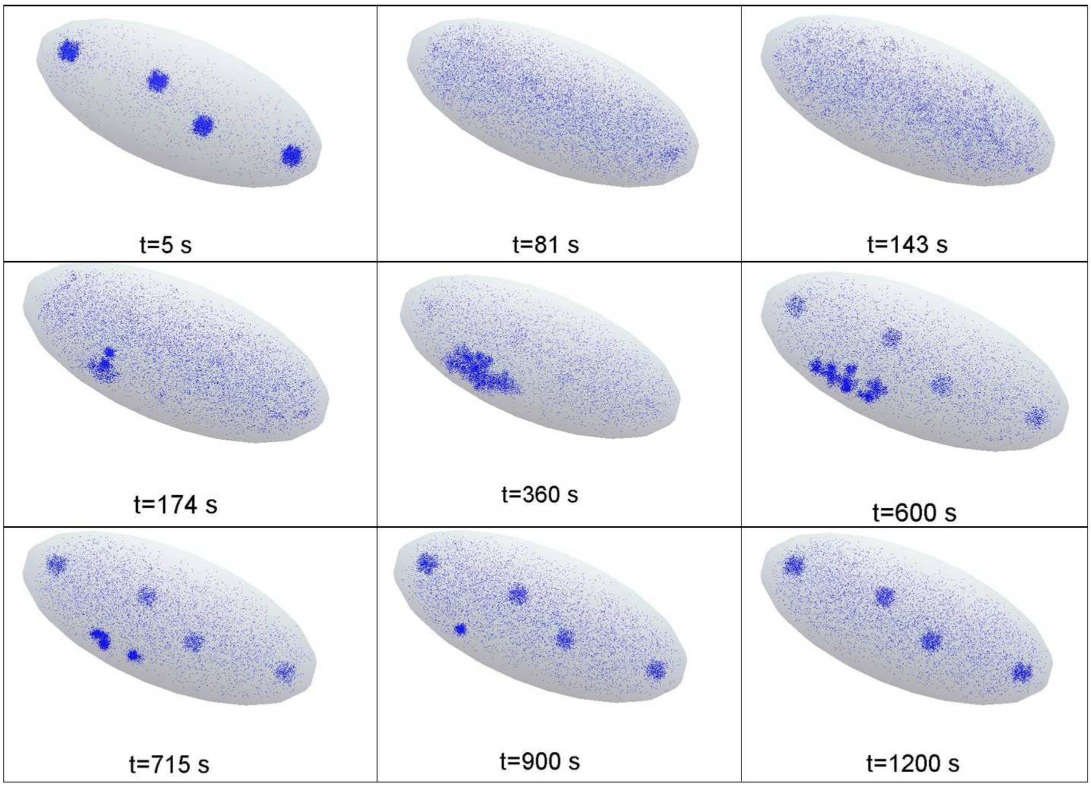

FIGURE B.2: DnaK evolution in *E. coli* with NSM simulation, after an alcoholic stress produced during the first 6 minutes.

differential equations.

$$\left\{\begin{array}{l} \frac{d[E]}{\mathrm{d}t} = \underbrace{k_0}_{if\ t<360\,s} -k_1\,[E]\,[P^*] + (k_{-1}+k_2)\,[EP^*] \\ \frac{d[P^*]}{\mathrm{d}t} = \underbrace{k'_0}_{if\ t<360\,s} -k_1\,[E]\,[P^*] + k_{-1}\,[EP^*] \\ \frac{d[EP^*]}{\mathrm{d}t} = k_1\,[E]\,[P^*] - (k_{-1}+k_2)\,[EP^*] \end{array}\right]$$

$$\underset{\substack{\uparrow k_0 \\ production}}{E} \quad + \underset{\substack{\uparrow k'_0 \\ P}}{P^*} \underset{k_{-1}}{\overset{k_1}{\rightleftharpoons}} EP^* \xrightarrow{k_2} E + P$$

The solution of this dynamical problem is deterministic whereas the one obtained previously is stochastic. This first study helped us to confirm the convergence of the stochastic system to the deterministic one and indeed both evolutions are perfectly similar (Figure B.4).

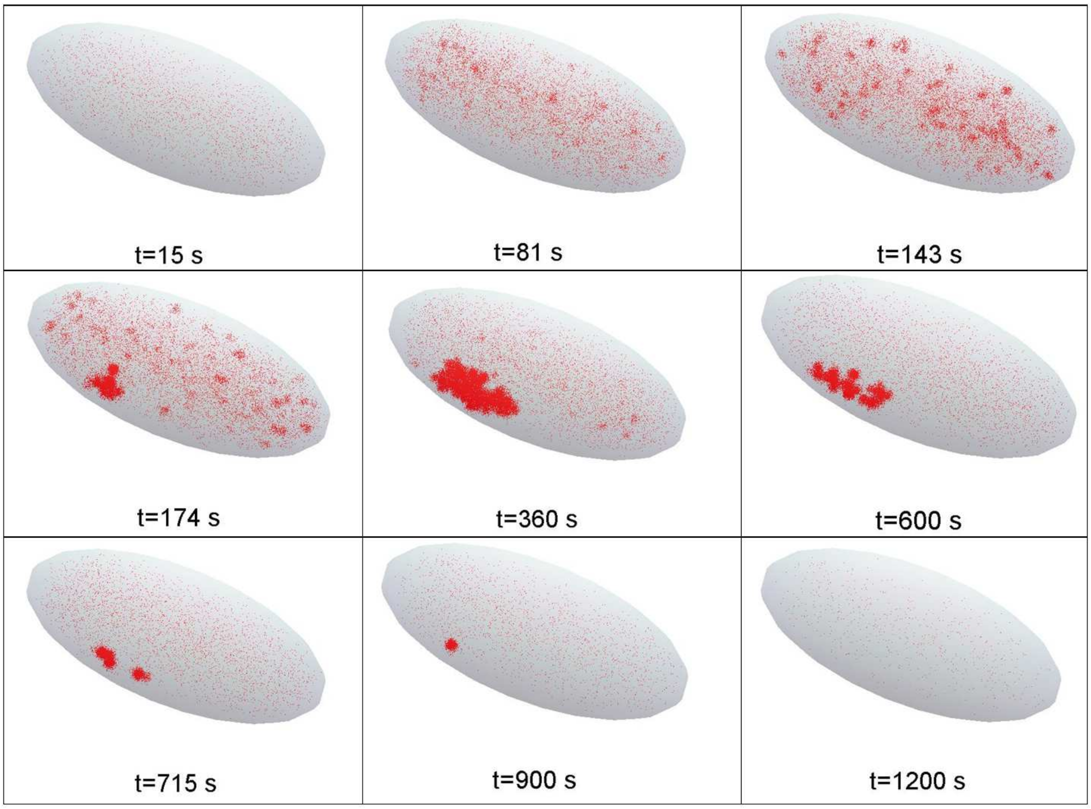

FIGURE B.3: Abnormal proteins evolution in *E. coli* with NSM simulation, after an alcoholic stress produced during the first 6 minutes.

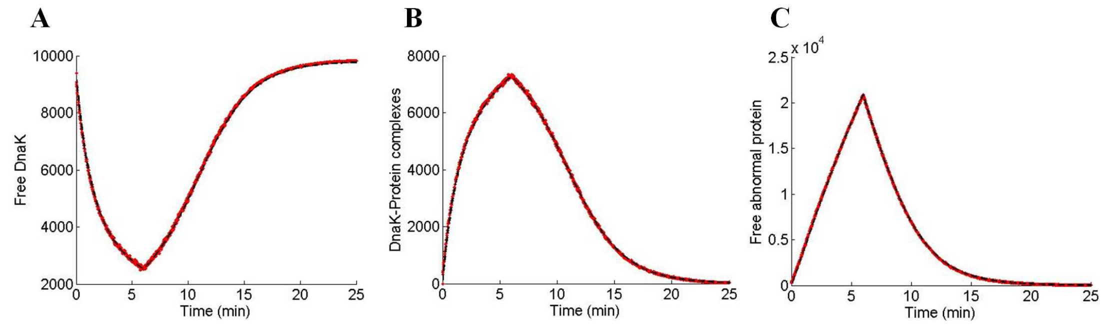

FIGURE B.4: Free DnaK, DnaK-protein complexes and free abnormal proteins evolution after an alcoholic stress in a homogeneous system. Comparison of the stochastic simulation (red points) and the ODE deterministic model.

Consequently we could validate our stochastic model and we then modified it to consider foci and/or protein aggregate.

The unhooking of the black curve (Figure B.6) (corresponding to the real model, with foci and with aggregation) with the other one in free DnaK evolution, appears near 3 minutes. This phenomenon appears simultaneously with the formation of the

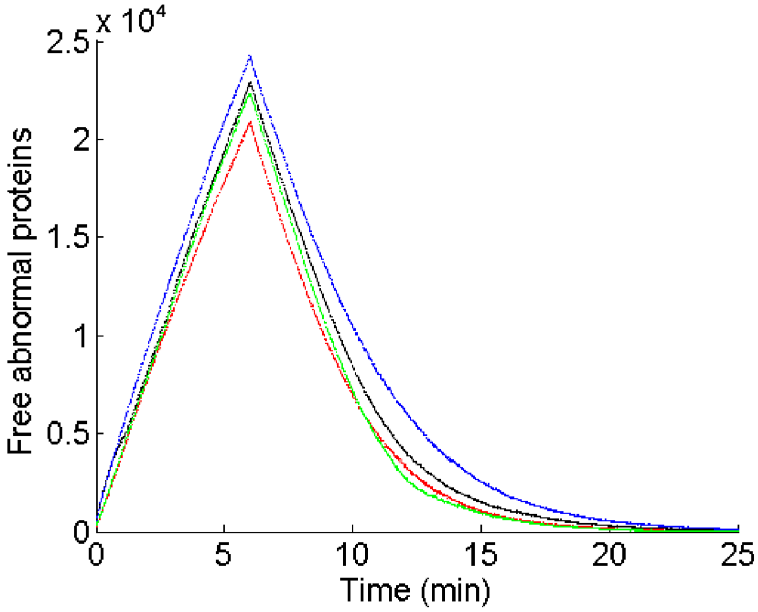

FIGURE B.5: Evolution of the number of abnormal protein obtained by the simulation with the next sub-volume method. Red : without foci and without protein aggregate ; Black : with foci and with protein aggregate ; Green : without foci and with protein aggregate ; Blue : with foci and without protein aggregate.

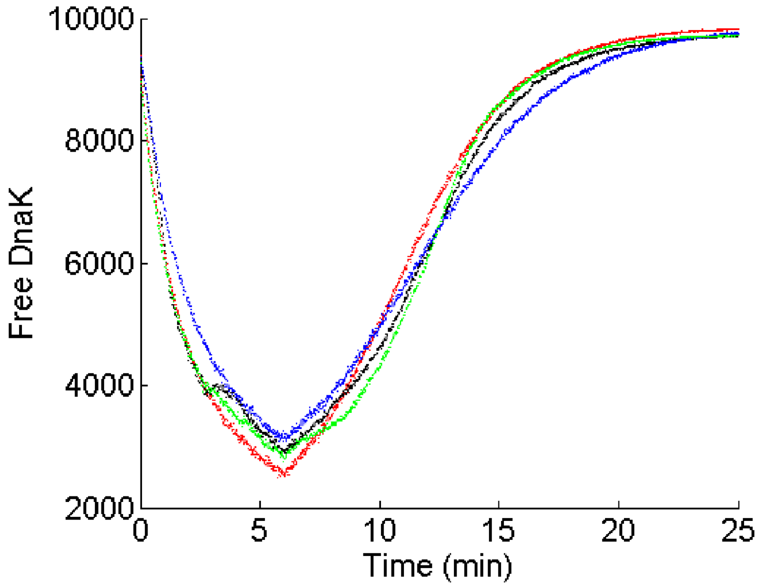

FIGURE B.6: Evolution of the number of free DnaK obtained by the simulation with the next sub-volume method. Red : without foci and without protein aggregate ; Black : with foci and with protein aggregate ; Green : without foci and with protein aggregate ; Blue : with foci and without protein aggregate.

big aggregate which is observed between 174 and 360 seconds in figure B.2. The aggregate may operate as a cage that reduces the efficiency of DnaK to complex abnormal proteins, but surprisingly abnormal proteins decrease more efficiently with the aggregate when DnaK owns foci (black curve) than without aggregate (blue curve) (Figure B.5). Therefore assuming DnaK foci we can consider that abnormal protein aggregation is a positive biological evolution process, because according to our simulations protein aggregates offer a better way for DnaK to act.

Moreover this model (for this study) answers Erwin Schrödinger's question. Here, it is unnecessary to invoke new physical or new chemical laws to describe even complex biological systems.

Bibliography

[1] T. Warnecke, "Loss of the DnaK-DnaJ-GrpE chaperone system among the Aquificales", Mol. Biol. Evol., vol. 29, no. 11, pp. 3485–3495, Nov. 2012.

[2] G. Kramer, D. Boehringer, N. Ban, and B. Bukau, "The ribosome as a platform for co-translational processing, folding and targeting of newly synthesized proteins", Nat. Struct. Mol. Biol., vol. 16, no. 6, pp. 589–597, Jun. 2009.

[3] Y. E. Kim, M. S. Hipp, A. Bracher, M. Hayer-Hartl, and F. U. Hartl, "Molecular chaperone functions in protein folding and proteostasis", Annu. Rev. Biochem., vol. 82, pp. 323–355, 2013.

[4] B. Bukau and G. C. Walker, "Cellular defects caused by deletion of the Escherichia coli dnaK gene indicate roles for heat shock protein in normal metabolism", J. Bacteriol., vol. 171, no. 5, pp. 2337–2346, May 1989.

[5] G. Calloni, T. Chen, S. M. Schermann, H. C. Chang, P. Genevaux, F. Agostini, G. G. Tartaglia, M. Hayer-Hartl, and F. U. Hartl, "DnaK functions as a central hub in the E. coli chaperone network", Cell Rep, vol. 1, no. 3, pp. 251–264, Mar. 2012.

[6] H. Itikawa, H. Fujita, and M. Wada, "High temperature induction of a stringent response in the dnaK(Ts) and dnaJ(Ts) mutants of Escherichia coli", J. Biochem., vol. 99, no. 6, pp. 1719–1724, Jun. 1986.

[7] K. H. Paek and G. C. Walker, "Escherichia coli dnaK null mutants are inviable at high temperature", J. Bacteriol., vol. 169, no. 1, pp. 283–290, Jan. 1987.

[8] E. Deuerling, H. Patzelt, S. Vorderwulbecke, T. Rauch, G. Kramer, E. Schaffitzel, A. Mogk, A. Schulze-Specking, H. Langen, and B. Bukau, "Trigger Factor and DnaK possess overlapping substrate pools and binding specificities", Mol. Microbiol., vol. 47, no. 5, pp. 1317–1328, Mar. 2003.

[9] A. Mogk, E. Deuerling, S. Vorderwulbecke, E. Vierling, and B. Bukau, "Small heat shock proteins, ClpB and the DnaK system form a functional triade in reversing protein aggregation", Mol. Microbiol., vol. 50, no. 2, pp. 585–595, Oct. 2003.

[10] M. J. Kerner, D. J. Naylor, Y. Ishihama, T. Maier, H. C. Chang, A. P. Stines, C. Georgopoulos, D. Frishman, M. Hayer-Hartl, M. Mann, and F. U. Hartl, "Proteome-wide analysis of chaperonin-dependent protein folding in Escherichia coli", Cell, vol. 122, no. 2, pp. 209–220, Jul. 2005.

[11] A. Fay and M. S. Glickman, "An essential nonredundant role for mycobacterial DnaK in native protein folding", PLoS Genet., vol. 10, no. 7, e1004516, Jul. 2014.

[12] M. Howard and A. D. Rutenberg, "Pattern formation inside bacteria: fluctuations due to the low copy number of proteins", Phys. Rev. Lett., vol. 90, no. 12, p. 128 102, Mar. 2003.

[13] M. B. Elowitz, M. G. Surette, P. E. Wolf, J. B. Stock, and S. Leibler, "Protein mobility in the cytoplasm of Escherichia coli", J. Bacteriol., vol. 181, no. 1, pp. 197–203, Jan. 1999.

[14] D. T. Gillespie, "A general method for numerically simulating the stochastic time evolution of coupled chemical reactions", J. Comp. Phys., vol. 22, no. 4, pp. 403–434, Dec. 1976.

[15] ——, "Exact stochastic simulation of coupled chemical reactions", J. Phys. Chem., vol. 81, no. 25, pp. 2340–2361, Dec. 1977.

[16] A. Mogk, T. Tomoyasu, P. Goloubinoff, S. Rudiger, D. Roder, H. Langen, and B. Bukau, "Identification of thermolabile Escherichia coli proteins: prevention and reversion of aggregation by DnaK and ClpB", EMBO J., vol. 18, no. 24, pp. 6934–6949, Dec. 1999.

[17] J. Elf and M. Ehrenberg, "Spontaneous separation of bi-stable biochemical systems into spatial domains of opposite phases", Syst Biol (Stevenage), vol. 1, no. 2, pp. 230–236, Dec. 2004.

[18] M. Kodaka, "Interpretation of concentration-dependence in aggregation kinetics", Biophys. Chem., vol. 109, no. 2, pp. 325–332, May 2004.

[19] J. Han and J. Herzfeld, "Macromolecular diffusion in crowded solutions", Biophys. J., vol. 65, no. 3, pp. 1155–1161, Sep. 1993.

[20] M. E. Young, R. L. Bell, and P. A. Carroad, "Estimation of diffusion coefficients of proteins", Biotechnol. Bioeng., vol. 22, no. 5, pp. 947–955, May 1980.

[21] M. T. Tyn and T. W. Gusek, "Prediction of diffusion coefficients of proteins", Biotechnol. Bioeng., vol. 35, no. 4, pp. 327–338, Feb. 1990.

[22] L. He and B. Niemeyer, "A novel correlation for protein diffusion coefficients based on molecular weight and radius of gyration", Biotechnol. Prog., vol. 19, no. 2, pp. 544–548, 2003.

[23] J. Elf, A. Doncic, and M. Ehrenberg, "Mesoscopic reaction-diffusion in intracellular signaling", in Proceedings of SPIE – Volume 5110, 2003, pp. 114–124.

[24] L. Michaelis and M. M. Menten, "The kinetics of invertin action. 1913", FEBS Lett., vol. 587, no. 17, pp. 2712–2720, Sep. 2013.

[25] K. Luby-Phelps, F. Lanni, and D. L. Taylor, "Behavior of a fluorescent analogue of calmodulin in living 3T3 cells", J. Cell Biol., vol. 101, no. 4, pp. 1245–1256, Oct. 1985.

[26] K. Luby-Phelps, S. Mujumdar, R. B. Mujumdar, L. A. Ernst, W. Galbraith, and A. S. Waggoner, "A novel fluorescence ratiometric method confirms the low solvent viscosity of the cytoplasm", Biophys. J., vol. 65, no. 1, pp. 236–242, Jul. 1993.

[27] K. Luby-Phelps, "Cytoarchitecture and physical properties of cytoplasm: volume, viscosity, diffusion, intracellular surface area", Int. Rev. Cytol., vol. 192, pp. 189–221, 2000.

[28] K. Jacobson and J. Wojcieszyn, "The translational mobility of substances within the cytoplasmic matrix", Proc. Natl. Acad. Sci. U.S.A., vol. 81, no. 21, pp. 6747–6751, Nov. 1984.

[29] R. Swaminathan, S. Bicknese, N. Periasamy, and A. S. Verkman, "Cytoplasmic viscosity near the cell plasma membrane: translational diffusion of a small fluorescent solute measured by total internal reflection-fluorescence photobleaching recovery", Biophys. J., vol. 71, no. 2, pp. 1140–1151, Aug. 1996.

[30] D. Schmid, A. Baici, H. Gehring, and P. Christen, "Kinetics of molecular chaperone action", Science, vol. 263, no. 5149, pp. 971–973, Feb. 1994.

[31] R. Schlecht, A. H. Erbse, B. Bukau, and M. P. Mayer, "Mechanics of Hsp70 chaperones enables differential interaction with client proteins", Nat. Struct. Mol. Biol., vol. 18, no. 3, pp. 345–351, Mar. 2011.

[32] J. Winkler, A. Seybert, L. Konig, S. Pruggnaller, U. Haselmann, V. Sourjik, M. Weiss, A. S. Frangakis, A. Mogk, and B. Bukau, "Quantitative and spatio-temporal features of protein aggregation in Escherichia coli and consequences on protein quality control and cellular ageing", EMBO J., vol. 29, no. 5, pp. 910–923, Mar. 2010.

Résumé

Les Formes Réactives de l'Oxygène (FRO) regroupent des molécules comme les radicaux superoxide ($O_2^{\bullet -}$) et hydroxyle ($HO^{\bullet}$) ou le peroxyde d'hydrogène (H_2O_2) qui sont produites en permanence au sein des cellules en aérobiose. Malgré des systèmes de défense, des FRO peuvent réagir fortuitement avec des protéines, des lipides ou l'ADN provoquant des dommages cellulaires dont les mécanismes ne sont pas encore entièrement élucidés. Afin d'appréhender ce "stress oxydant", cette thèse présente des simulations numériques de la dynamique de FRO en utilisant la bactérie *E. coli* comme organisme modèle. Dans un premier temps, les simulations numériques sont réalisées de façon déterministe sur un ensemble de cellules. L'étude de la mortalité de *E. coli* exposé à H_2O_2 montre que le fer intracellulaire libre et la densité cellulaire, deux facteurs potentiellement impliqués dans la dynamique des FRO, jouent un rôle primordial dans l'interprétation expérimentale comme par exemple le comportement bi-modal de *E. coli* opposé à H_2O_2. Nous avons également évalué les rôles relatifs des principales défenses mises en place contre H_2O_2 à savoir la membrane cellulaire et les enzymes. Une étude détaillée indique que leur implication dépend non linéairement de la concentration en H_2O_2. Dans une seconde approche et grâce à l'étude déterministe nous réduisons l'échelle d'étude pour nous ramener à la cellule unique dans les conditions physiologiques. La taille du système impose alors des méthodes numériques stochastiques. Il apparaît ainsi que la stochasticité intrinsèque des réactions chimiques associées aux FRO permet à certaines bactéries de se différencier en vue d'un futur stress. En effet, bien que la distribution statistique des FRO ne déclenche pas le système de régulation de défense dans les conditions physiologiques, nous montrons qu'elle peut en revanche enclencher les mécanismes de réparation de l'ADN dont les lésions sont le résultat d'une succession d'événements rares impliquant un très faible nombre de molécules.

Abstract

The Reactive Oxygen Species (ROS) are molecules (superoxide $O_2^{\bullet -}$, hydrogen peroxide H_2O_2 and hydroxyl radical $HO^{\bullet}$) that are continuously generated in living cells as a consequence of aerobic life. They are partially eliminated by scavenging systems. Nevertheless, ROS can unfortunately react with cellular proteins, lipids or DNA leading to cell damage. The mechanisms of such lesions is still being studied : we are talking about "oxidative stress". Using *Escherichia coli* as a model organism this thesis is concerned with the numerical simulation of ROS dynamics. In the first part of this work, simulations were performed in a deterministic way to predict the behaviour of a set of cells. By studying killing of *E. coli* by exposure to H_2O_2, we show that intracellular available iron and cell density, two factors potentially involved in ROS dynamics, play a major role in the prediction of experimental results in particular in bimodal cell killing. We then evaluate the relative roles of major defences against H_2O_2. Although the key actors in cell defence are enzymes and membrane, a detailed analysis shows that their involvement depends on the H_2O_2 concentration level. In the second part and thanks to the first deterministic approach, we study more closely the fate of the single cell with a stochastic point of view in physiological conditions. We show that elementary chemical stochasticity allows bacteria to segregate specialized cells in prevision of possible stress challenge. Actually, whereas ROS distribution does not activate defence regulation without exogenous stress, we demonstrate that this distribution may activate DNA repair mechanisms because DNA nicks are the result of a succession of rare events which involve a small number of molecules.